SAPIENZA
UNIVERSITÀ DI ROMA

Beam loading assisted matching working point for PWFA beam driven experiment at SPARC_LAB

Istituto Nazionale di Fisica Nucleare

Dottorato di Ricerca in Fisica degli acceleratori – XXIX Ciclo

Candidate

Stefano Romeo
ID number 1603031

Thesis Advisor

Dr. Massimo Ferrario

A thesis submitted in partial fulfillment of the requirements
for the degree of Doctor of Philosophy in Accelerator Physics

June 2017

Thesis defended on 20 September 2017
in front of a Board of Examiners composed by:

Dr. Antonio Capone (chairman)

Dr. Renato Fedele

Dr. Danilo Giulietti

Beam loading assisted matching working point for PWFA beam driven experiment at SPARC_LAB

Ph.D. thesis. Sapienza – University of Rome

This thesis has been typeset by LaTeX and the Sapthesis class.

Author's email: stefano.romeo@lnf.infn.it

Contents

Abstract

This thesis concerns the investigation of the methods to improve the quality of beams accelerated via beam-driven plasma wakefield acceleration (PWFA) schemes in therms of emittance and energy spread.
In the I chapter the motivation that led to the use of plasma wakefields in order to accelerate beams instead of conventional RF-based accelerating structures is reviewed, reporting also the state of the art of beam driven PWFA experiments. Investigating the differences between linear and non linear plasma wake, a proposal for a new scheme is elaborated. This scheme is based on the combination of a low quality high charge driver that generates an accelerating wakefield in linear regime and an high quality low charge witness that is injected in a region close to the crest of the accelerating wakefield. Since most of the focusing field is guaranteed by the beam loading effect, this scheme was called Beam Loading ASsisted maTching (BLAST) scheme. The theoretical tools to develope the study of this kind of working point are also discussed.
The II chapter introduces the models used to describe the fields inside plasma. The very well-estabilished plasma linear theory will be developed in electrostatic approximation in order to derive a complete solution of the fields in the entire space. This solution will be used to obtain scaling laws that describe the main features of plasma acceleration i.e. maximum attainable energy, expected energy spread growth and optimal injection phase of witness for beam loading compensation of energy spread. The solution for the transverse field will be used in order to find the matching conditions via the envelope equation. Finally a procedure for the design of BLAST working points will be presented.
The III chapter will introduce the SPARC_LAB facility, pointing out the features of the injector and the experimental setup for the plasma acceleration experiments.
In chapter IV the scaling laws derived in chapter II will be verified through the simulation of a working point for an experiment of high quality plasma acceleration to be performed at SPARC_LAB. The robustness of this working point will be also investigated through a tolerance analysis.

Outline

In this work we will introduce and define a new kind of accelerating scheme for the plasma wakefield acceleration that takes advantage of an enhanched beam loading effect to guarantee a matched propagation of the trailing bunch and helps to preserve the beam quality. We will also implement the scheme to design a working point for an experiment to be performed at the SPARC_LAB test facility.
The first chapter introduces the state of the art of RF based and plasma based accelerators, pointing out the limits of both technologies and the reasons that makes the plasma acceleration so interesting. The linear regime and the blow-out regime of plasma acceleration will be also summarized, pointing out differences, advantages and disadvantages. In the end, the beam loading assisted matching working point will be introduced.
The second chapter is dedicated to plasma beam dynamics. We will apply the cold fluid model for plasma waves in order to extrapolate the main features of the new scheme.
The third chapter is dedicated to the experimental setup of SPARC_LAB facility, pointing out the characteristics of the outcoming beams, final focus device and the plasma interaction chamber features.
The fourth chapter is dedicated to the SPARC_LAB working point design and tolerance analysis.

Chapter 1

From conventional to plasma accelerators

The first example of the usefulness that particle accelerators have for fundamental physics is the Rutherford scattering experiment of α particles in 1911. Since then, particle accelerators imposed their presence in almost any scientific or technical field. The importance of accelerators like the Large Hadron Collider (LHC) for the fundamental physics is very well known, less known are for example the applications for semi-conductors doping, the activation of the materials used for X-ray diagnostics, the more recent hadron therapy for the cure of cancer, the application of the synchrotron radiation and Free Electron Laser radiation for biology, chemistry, paleontology and archeology.
Particle accelerators are today an integral part of everyday life and the improvement of their technology is of primary importance for the development of science. The challenge of plasma accelerators is the goal of really compact particle accelerators that can make avalaible to a larger number of users the results obtained so far and the potential new applications of these fascinating tools.
The main purpose driving the development of particle accelerators technology has always been the fundamental phyisics. Today technology allows to accelerate and collide two charged particle beams up to the energy of 14 TeV in the center of mass reference frame [1], giving the possibility to recreate the conditions that existed few istants after the big bang. The study of the processes acting during these collisions helps to understand the fundamental forces that govern the universe leading to the unified field theory. The last great success obtained by the use of an accelerator is the discovery of an Higgs boson-like particle performed by LHC in 2012, the missing dowel of the Standard Model, that is mainly recognized as the most successful theory of the particle physics.
The necessity of going beyond these results requires, unfortunately, even greater collision energies, that require more powerful and more expensive accelerators in order to be achieved, as shown in Fig. 1.1.

Plasma accelerators can be seen as a promising improvement of electron linac technology, represented in the chart by the green line. The technological limit right now for the accelerating RF structures is $\approx 100\text{MV/m}$ [3] of accelerating gradient (in X-band) while a plasma based accelerator can reach accelerating gradient $\gg 1\text{GV/m}$,

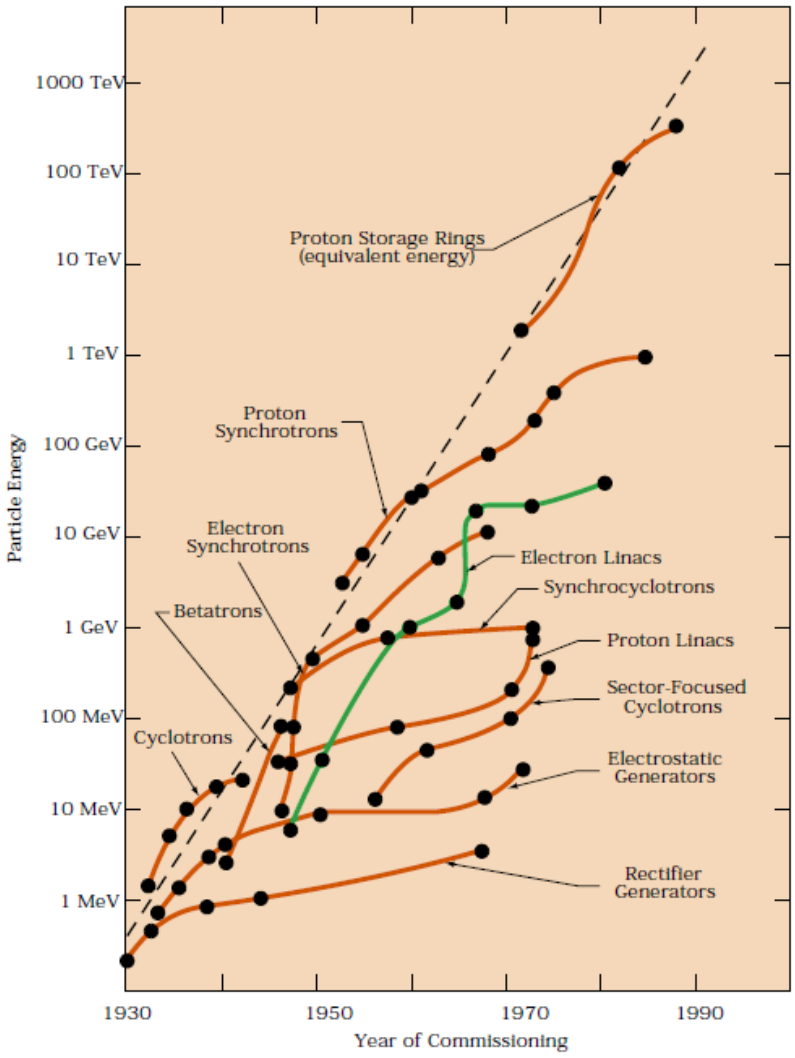

Figure 1.1. Progress in collision energy over time from reference [2]

marking an improvement greater than a factor ten in the state of the art of linear accelerators and becoming very helpful for the design of future linear colliders. Going beyond the energy of LHC or the future International Linear Collider (ILC [4]) would require very expensive accelerators with length $>$ 30km. Further, as we can see from Fig. 1.2, LHC differs from the linear growth of the energy of hadron accelerators, a signal that we are reaching the limit of what can be designed with current technology and a technological leap is required to overcome the current limits.

One of the most promising way to obtain compact accelerating devices is the plasma wakefield acceleration. The fields that can be generated inside plasma are orders of magnitude higher than the state of the art accelerating cavities possibilities (GV-TV/m). Very high accelerating gradients have been obtained by several experiments

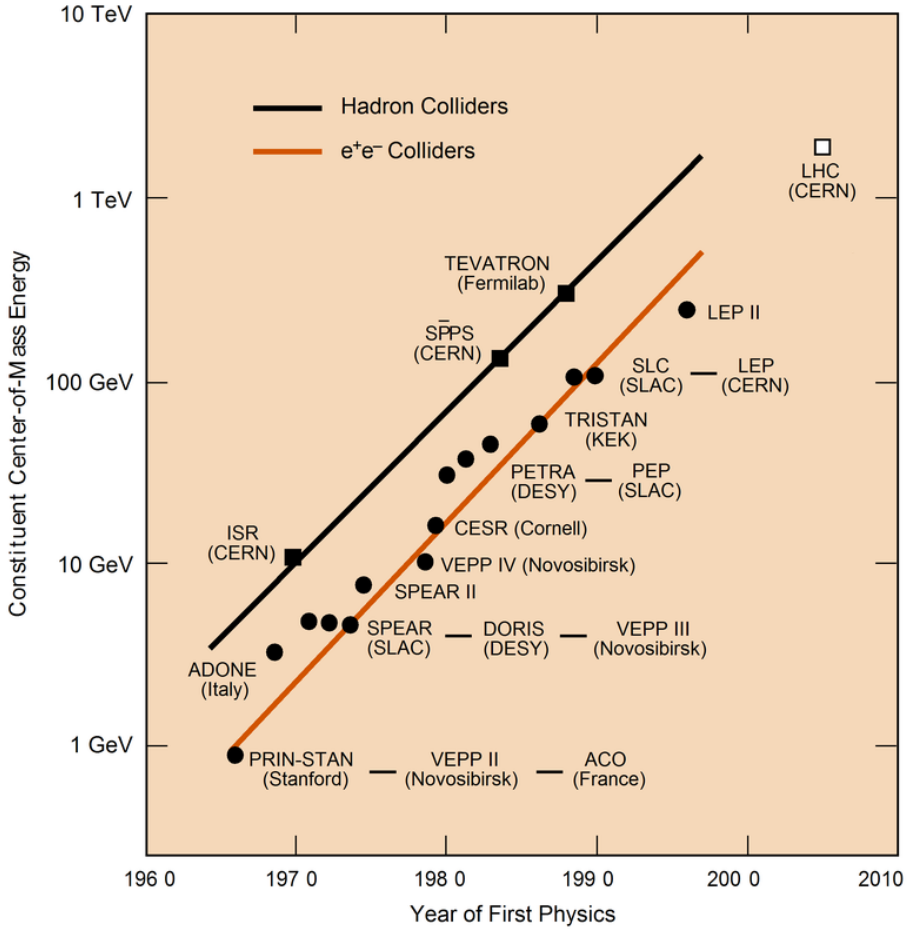

Figure 1.2. Progress in collision energy over time for different facilities from reference [2]

[5] with high gradient acceleration, both laser (LWFA) and plasma wakefield beam driven (PWFA). Nevertheless, there is still a great issue concerning the quality of outcoming beams. Conventional accelerators are able to produce beams with very low emittance and energy spread ($<$ 1mm mrad, $\ll 1\%$). As we will see in detail in next sections, beams accelerated by PWFA still suffer, at present, of higher emittance and energy spread compared to RF accelerators.
Higher accelerating gradients allow to create more compact accelerators with the same energy. The maximum electric field that can be generated by RF cavities is primarly limited by discharge breakdown.
The main work to be referred for discharge breakdown is the Kilpatrick's Criterion [6]. In his work Kilpatrick used some experimental results in order to empirically define the breakdown threshold as a function of working frequency and accelerating field. The original Kilpatrick's formula was

$$Ee^{-4.25/E} = 24.4 \cdot (f[GHz])^{\frac{1}{2}}[MV/m]; \tag{1.1}$$

that was then reformulated by T.J. Boyd [7] as

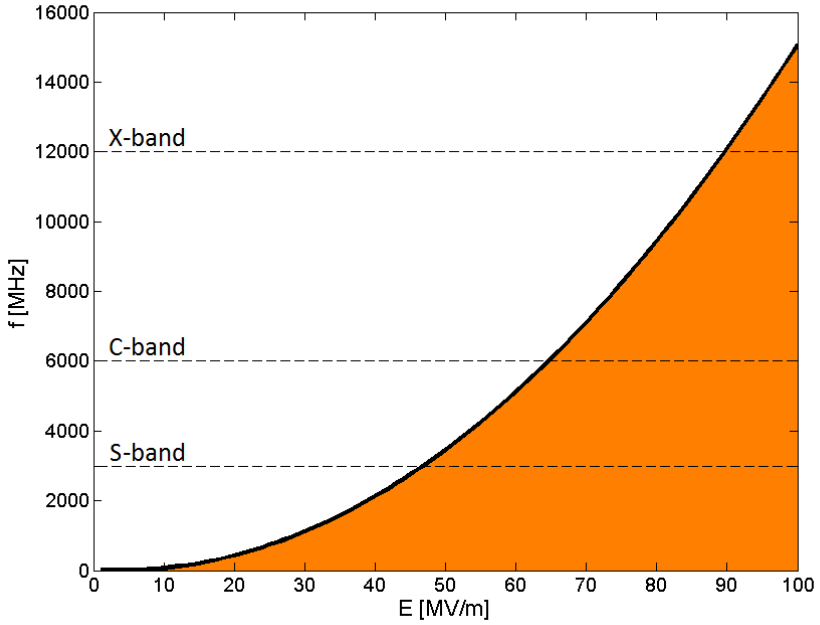

Figure 1.3. Kilpatrick's limit [6]

$$f[MHz] = 1.64 \cdot E[MV/m]^2 \cdot e^{-8.5/(E[MV/m])}. \tag{1.2}$$

In order to increase accelerating gradient and avoid sparks it is necessary to build cavity designed to work at higher frequency.
The Kilpatrick limit is reported in Fig. 1.3. The white region is expected to work without sparks. A work of 1986 by T.J. Wang et al. [8] showed that it is possible to overcome the Kilpatrick's limit for higher RF frequency. In Fig. 1.4 we can see the corrected limits.
Despite it has been demonstrated that it's possible to overcome the Kilpatrick limit of beyond a factor ~ 10, the limit of 500MV/m is a very hard challenge for RF accelerating structures and a stable gradient of 1GV/m is far away from the state of the art, making a technological upgrade desiderable.
In this work we developed a new beam driven PWFA scheme named Beam Loading ASsisted maTching (BLAST) aiming to increasing the outcoming beam quality. The scheme is based on a low brightness driver that generates an accelerating wakefield in linear regime and a very high brightness witness injected behind the driver on the crest region of the accelerating field. In the injection region the focusing field generated by the driver is negligible and the transverse matching of witness is based on a beam loading effect. The motivations for this kind of structure and the reasons of the stability of BLAST scheme will be also discussed.
The BLAST scheme is also a possible candidate for positron acceleration that is a very challenging topic for the PWFA schemes [9].

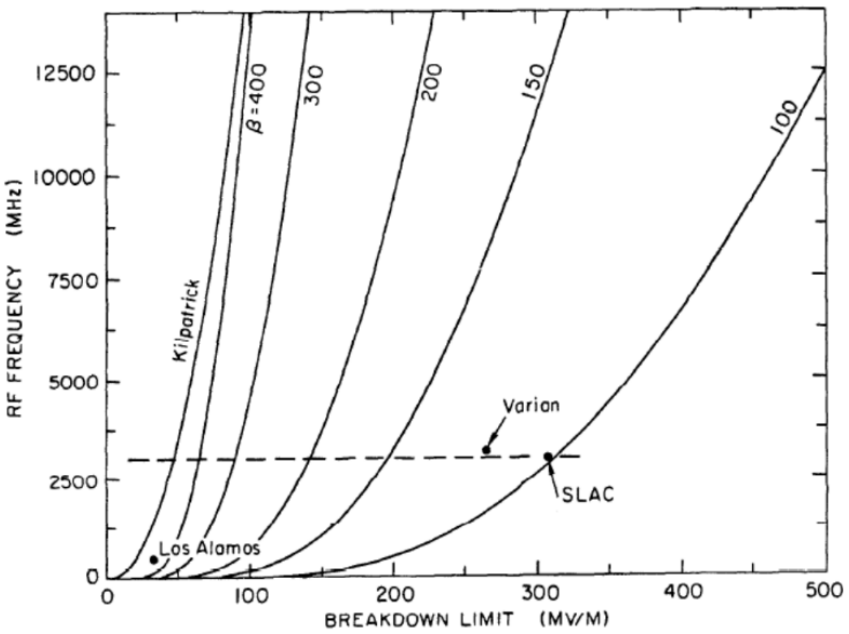

Figure 1.4. Breakdown limit from Wang's report [8]

1.1 Beam quality: luminosity, brightness and chromaticity

The most important parameters that define the quality of a collider are center of mass energy and luminosity.
The luminosity is defined as

$$\mathcal{L} = \frac{1}{\sigma}\frac{dN}{dt}; \tag{1.3}$$

where σ is the cross section, and N the number of events. It is possible to demonstrate [10] that two equal round gaussian beams colliding head on have a luminosity

$$\mathcal{L} = \frac{N_1 N_2 N_b}{4\pi\sigma_r^2} f; \tag{1.4}$$

where N_b is the number of bunch inside a single beam, N_1 and N_2 are the number of particles contained in every beam, f is the collision rate and σ_r is the rms radius of the beams. As demonstrated in Appendix C, it is possible to write $\sigma_r = \sqrt{\beta_r \epsilon_r}$, where β is the β-function in the collision point and ϵ_r the rms emittance. The minimum value of β that can be reached by a magnetic transport line is affected by the gradient of the focusing element and on the length of final focus devices, leading to the conclusion that lower emittances help to increase the luminosity.
One important applications of particle accelerators consists in the generation of advanced radiation sources. The intensity of these sources depend on the brightness of the beams that generate them. The brightness is defined as [11]

$$B_n = \frac{2I}{\pi^2 \epsilon_n^2}; \tag{1.5}$$

where I is the peak current of the beam and ϵ_n is the normalized emittance. Beams with higher brightness guarantee higher brilliance of radiation sources.
High energy spread of the beam can lead to difficulties in beam focusing and to emittance growth during transport [12].
High quality beams are characterized by low emittance and low energy spread.

1.2 Plasma wakefield acceleration overview

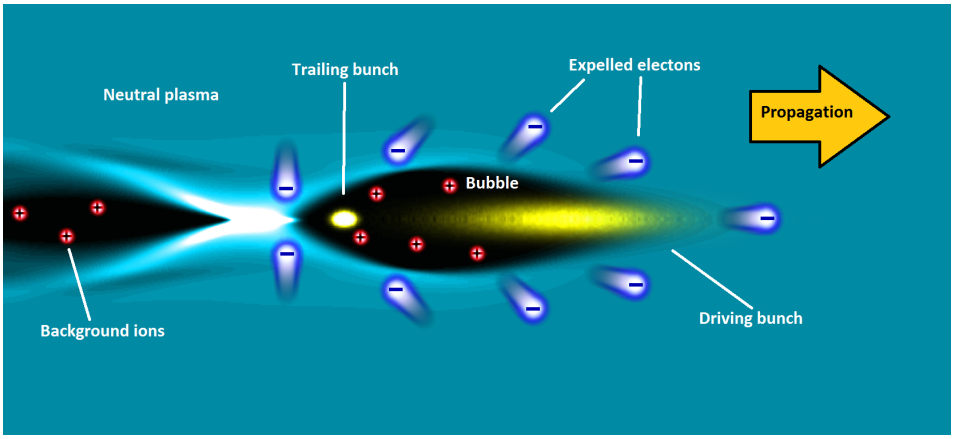

Figure 1.5. PWFA beam driven scheme for highly non linear driving bunch

Plasma physics was originally developed in order to analyze processes that occur at very high temperature, where the electric bounds of the electrons with the nuclei breaks and the coulomb interactions between the elements of the matter become non negligible and sometimes dominant. The idea of using plasma wakefield in order to accelerate particles is due to Tajima and Dawson in 1979 [13]. In their work they evidenced how the wakefield generated inside plasma by the ponderomotive force of a laser had an oscillating behaviour and that a bunch of electrons could be trapped inside the wake and accelerated with very high gradients. The plasma wakefield acceleration is a very attractive technological development due to the fact that the electric and magnetic fields generated inside plasma are orders of magnitude higher with respect to conventional structures (hundreds of GV/m) [14].
LWFA experiments have shown that it is possible to achieve gradients of the order of TV/m, but the quality of the generated beams was low, with an energy spread of the order of 100% and very high emittances [15, 16, 17, 18, 19, 20]. An higher degree of control of laser and plasma parameters allowed to perform some experiments with a significant accelerated charge ($\geq$ 100pC), high mean energy ($\approx 100MeV$) and relatively high beam quality (few percents of energy spread and divergence of few milliradians) [21, 22, 23]. After that in 2006 Leemans, Nagler, et al. [24] were able to produce an electron beam with 1GeV energy of using LWFA, and in 2013 Kim et al [25] were able to produce a $3GeV$ beam with the multi-staging LWFA.
An alternative to LWFA is the beam driven plasma wakefield acceleration scheme proposed by Chen et al. in 1985 [26]. The response of the plasma to an electron bunch coulombian field is mostly equivalent to the effect of the ponderomotive force generated by laser.
Many experiments has been performed in order to prove the validity of the beam driven scheme [27, 28], but, as we will evidence in this chapter, there is still a great problem concerning the beam quality at the exit of plasma. This work will focus on the possibility of increasing the accelerated beam quality preserving an high accelerating gradient inside plasma.

1.3 Beam driven plasma wakefield acceleration experiments

The most promising results have been obtained in beam driven PWFA schemes are highlighted in the following paragraphs. The experiments were performed in highly non linear regime, which means a driver bunch with high density if compared to the background plasma density. Details will be given in the next sections and in Appendices.

1.3.1 Energy doubling of 42 GeV electrons in a metre-scale plasma wakefield accelerator

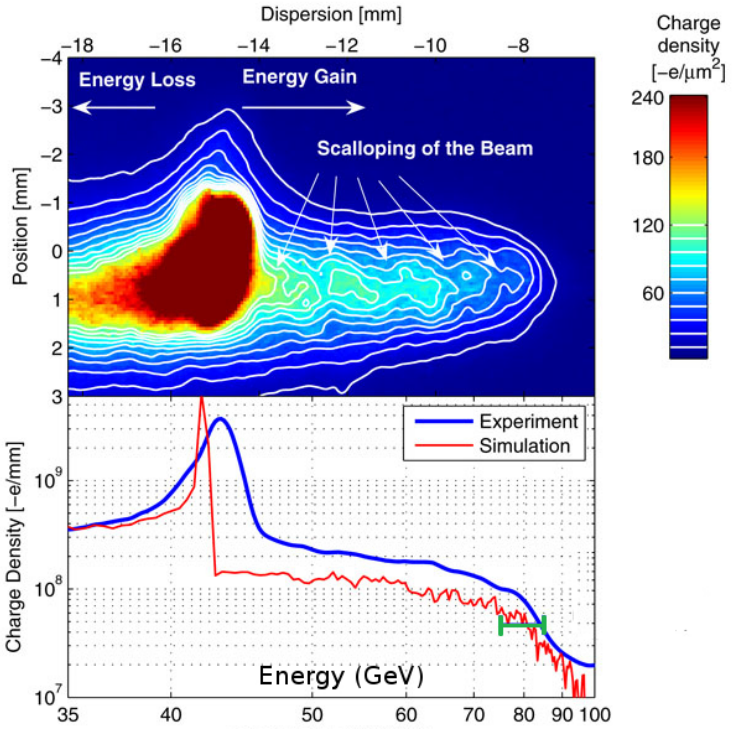

Figure 1.6. Energy spectrum of the outcoming beam in Blumenfeld experiment. On the x axis are represented both the dispersion [mm] and the energy spectrum [GeV] while in the y axis are represented the position [mm] of the electrons on the diagnostic screen (figure above) and the electron linear density [mm^{-1}] (figure below). As we can see the experiment showed an effective energy doubling of part of the incoming beam (green line) but at cost of an absolute energy spread of the order of 1.5GeV.

The experiment performed by Blumenfeld et al. [27] in 2007 showed high energy gain and accelerating gradient of beam driven PWFA. The experiment consisted in a single bunch with energy $E = 42$ GeV, length $\sigma_z = 15\ \mu$m and charge $Q \approx 3$ nC injected in an 85 cm long ion column of lithium vapour with an electron density of $n_e = 2.7 \cdot 10^{17}\ \text{cm}^{-3}$. Since the beam length was approximatively of the same size of the plasma bubble, the head of the beam lost energy and the tail of the beam gained energy at the expense of a dramatic increase of energy spread.

The result of the experiment was an outcoming beam with an energy spectrum as showed in Fig. 1.6. As we can see the experiment showed an effective energy doubling of part of the incoming beam (green line) but at cost of an absolute energy spread of the order of 1.5 GeV.

1.3.2 High-efficiency acceleration of an electron beam in a plasma wakefield accelerator

The experiment performed by Litos et al. [28] in 2014 consisted in 2 bunches, a driver with a charge $Q = 1.02$ nC, a length $\sigma_z = 25\ \mu$m and a witness with a charge $Q = 780$ pC, a length $\sigma_z = 47\ \mu$m are injected both with an incoming energy $E = 20.35$ GeV inside a ionized column of lithium with an effective electron density of $n_e = 5 \cdot 10^{16}$ cm^{-3}. Since the two bunches are both contained inside the bubble, the first bunch generates the bubble and the second is accelerated, preserving the energy spread of the trailing bunch. The spatial beams distributions of density and current and the accelerating field outcoming from simulations are shown in Fig. 1.7a both for the single injection of the driver and for the scheme of driver and witness. The result of the experiment was an outcoming witness with an energy spectrum as showed in Fig. 1.7b. As pointed out in reference, the effective energy gain during the acceleration was of 1.6 GeV for the core particles (charge $Q_c = 74$ pC) with an effective accelerating gradient of 4.4 GV/m. The outcoming energy spread for the core was of 0.7% in the single shot with a total energy spread of 2% integrated on all the measurement set of 92 shots. The reduced energy spread was a result of the optimized shaping of the trailing bunch profile. No measurement of outcoming beam emittance were performed during that experiment.

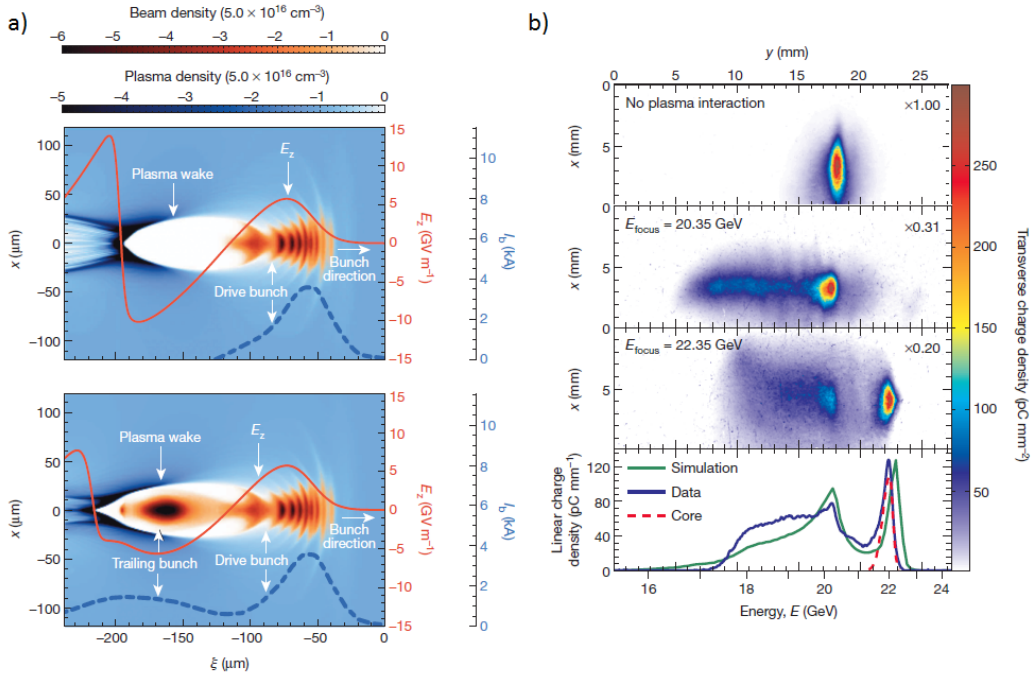

Figure 1.7. (a) Simulation results for the Litos experiment. The figure above refers to a case with the driving bunch only, while the figure below refers to a case with both driving and trailing bunch. Beam electron density is shown in red scale while the plasma electron density is shown in blue scale. As we can see the introduction of trailing bunch with a proper longitudinal distribution (dashed blue line) causes a flattening of the accelerating gradient profile (red continuous line) that effectively reduces the outcoming beam energy spread.
(b) Energy spectrum of the outcoming beams in Litos experiment (2014). On the x axis are represented both the dispersion y[mm] and the energy spectrum E[GeV] while in the y axis are represented the position x[mm] of the electrons on the diagnostic screen (figure above) and the electron linear density $[mm^{-1}]$ (figure below). The first figure refers to the case of an incoming couple of beams without plasma interaction. The second figure refers to the outcoming beams with plasma interaction and a spectrometer set to image the incoming energy (20.35GeV). The third figure refers to the outcoming beams with plasma interaction and a spectrometer set to image the witness core average energy (22.35GeV). The last figure shows the integrated spectrum of the outcoming beams. The blue continuous line represent the experimental data, the continuous line represent the simulation data and the red dashed line represents the witness core.

1.4 Linear vs. Blow-out regime

Plasma wakefield perturbations can be treated in a simple analytical way in two cases:

- Small perturbations: the non linear terms of the equations describing plasma can be neglected and it is possible to find an analytical solution. This case is known as linear regime [29, 30, 31].
- Strong perturbations: in this case inside the plasma there are regions completely emptied of electrons and the local electron density is 0. This case is known as blow-out regime [32, 33, 34].

The kind of perturbation is determined by the normalized bunch density α that is defined as

$$\alpha = \frac{n_b}{n_0}; \tag{1.6}$$

where n_b is the density of the bunch and n_0 the background plasma density. Bunches with low densities generate small perturbations on plasma, so the action of the bunch over plasma can be described by the equations of the linear regime if $\alpha \ll 1$. On the contrary, bunch with high density, $\alpha \gg 1$, can be described properly by the blow-out model. The linear theory is presented in Appendix A, while the blow-out model is presented in Appendix B. Below we list the main differences in the two different regimes.

1.4.1 Focusing field

The main difference between the linear regime and the blow-out regime [35] concerns the focusing field generated by driver. The focusing field generated by a low density driver propagating in plasma at the speed of light c in cylindrical symmetry can be written as

$$E_r(r,\xi) = \sqrt{\frac{\pi}{2}}\frac{c^2 m_e}{e}(\alpha)(k_p\sigma_z)e^{-k_p^2\sigma_z^2/2}\,\mathrm{Re}\left[e^{ik_p\xi}\,\mathrm{erfc}\left(\frac{\xi}{\sqrt{2}\sigma_z}+i\frac{k_p\sigma_z}{\sqrt{2}}\right)\right]R'(r); \tag{1.7}$$

where $\xi = z - ct$ and $R'(r)$ is a function of the transverse component. It can be demonstrated that $R'(r)$ is not linear in r (see Appendix A, Eq. A.43). The focusing field also depends on the longitudinal coordinate ξ and on the normalized bunch density α. A driver that is evolving through the plasma channel generally has a density that is not constant. So the focusing field generated by low density drivers is also a function of time.
An high density driver, instead, generates inside the blow-out region a focusing field that is linear and uncorrelated in the longitudinal dimension. In the limit that $\alpha \gg 1$, the field is also constant during the propagation in the plasma channel and does not depend on ξ. This kind of focusing field is highly preferable to the previous one for beam dynamics reasons, which will be fully explained in the next section.

1.4.2 Accelerating field

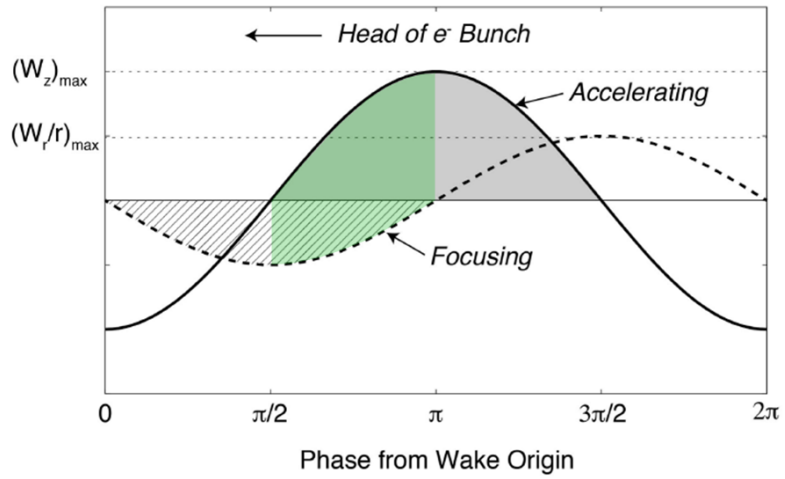

Figure 1.8. Longitudinal dependency of wakefields in linear regime. The green region guarantees both accelerating and focusing field.

The accelerating wakefield generated by a low density bunch behind the driver can be written as

$$E_z(r,\xi) = \sqrt{2\pi}\frac{c^2 m_e}{e}(\alpha)(k_p^2\sigma_z)e^{-k_p^2\sigma_z^2/2}\cos k_p\xi\, R(r). \tag{1.8}$$

showing a sinusoidal behaviour, so the crest region guarantees the lowest energy spread and the maximum accelerating gradient. Unfortunately, the crest region is not useful for accelerating bunches because we can write the focusing field

$$E_r(r,\xi) = \sqrt{2\pi}\frac{c^2 m_e}{e}(\alpha)(k_p\sigma_z)e^{-k_p^2\sigma_z^2/2}\sin k_p\xi\, R'(r). \tag{1.9}$$

In fact the crest region corresponds to $\cos(k_p\xi) = 1$ and $\sin(k_p\xi) = 0$, so the crest region guarantees no focusing field for the witness. In Fig. 1.8 we show the useful region for acceleration in linear regime.
According to Eq.(1.8) also the accelerating field depends on α, that doesn't remain constant during acceleration. The accelerating field has also a dependency on the transverse position that introduced further energy spread that has to be evaluated. The longitudinal field profile presents a spike in the zone of bubble closure that corresponds to the maximum accelerating gradient but also to the maximum energy spread. The accelerating field is not dependant on the transverse position so the energy spread can be completely evaluated only taking into account the longitudinal contribution.

1.5 Beam Loading ASsisted maTching scheme

The Beam Loading ASsisted maTching (BLAST) scheme presented in this thesis aims to use the advantages of linear and non linear scheme, combining the high accelerating gradient and a focusing field that does not depend on the driver with the possibility of use an high amount of the accelerating gradient with a compensation of energy spread that is also function of the bunch separation.
It consists in a beam driven scheme where:

- The driver generates a linear or quasi-linear field ($\alpha_D < 1$);
- The witness generates an highly non linear field ($\alpha_w \gg 1$);
- Witness injection is performed close to accelerating field crest.

This scheme is illustrated in Fig. 1.9.

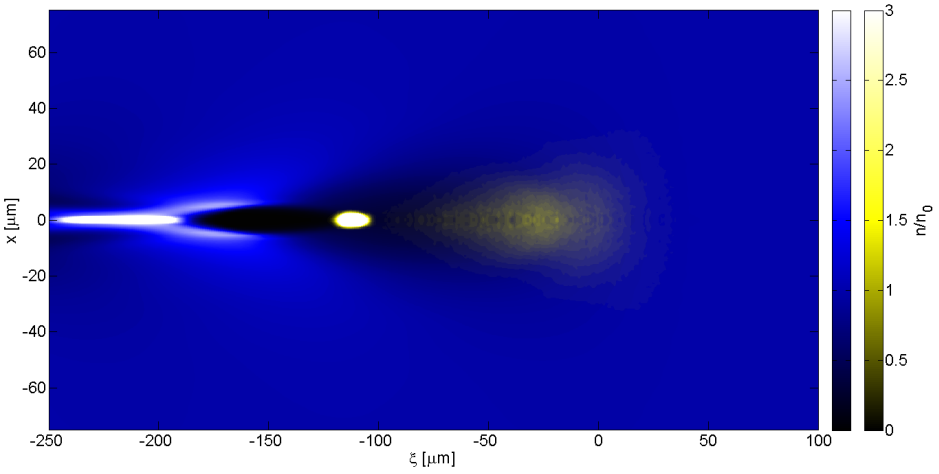

Figure 1.9. Beam loading assisted matching (BLAST) scheme. Background plasma electron density is represented in blue scale while the bunches are presented in yellow scale. The low density driver (on the right) generates a linear field, the witness high density witness (on the left) is injected on the crest of linear field (where assuming negligible beam loading the local plasma density results to be unperturbed) and generates a bubble.

The idea behind the BLAST scheme is to use the crest of the linear field that is the most suitable for acceleration, despite that region presents a negligible focusing effect.
We investigated the possibility of injecting the witness in the crest field region using an external focusing device (i.e. active plasma lensing [36]) during acceleration. Optimal acceleration of a witness in the wake of a low density driver requires that the transverse dimension of the witness is much smaller than the driver's one. The β-function required during all the acceleration is of the order of $\approx$ 1mm, requiring very high focusing field. As a consequence, the technical realization of external focusing devices resulted to be too challenging.
On the contrary, the self focusing effect that has been modelized throughout this

thesis work, showed optimal features and a relatively simple realization. The most important are:

- the plasma wakefields in the region of the driver and the witness follow a linear behaviour, so it is possible to modelize them analitically;
- the energy spread depends on the separation of bunches; this feature allows to identify for a large range of witness parameters an optimal injection distance that keeps low energy spread; furthermore, there is a low dependency from the driver parameters, that makes the conditions of the driver at the injection more relaxed;
- the optimal injection distance is located near the crest region, allowing to use an high amount of the accelerating field;
- the matched spot size for emittance preservation does not depend on the driver parameters.

There are also some disadvantages connected mostly to the driver's dynamics. Due to the fact that a driver injected inside the neutral plasma creates a self focusing field [37], if the driver emittance is too low, the driver bunch density will increase after the injection, creating a blow-out region. Further, the expansion of the driver inside the plasma channel reduces the normalized bunch density and the accelerating field. These problems will be analyzed in detail and partially solved in the next chapters.

Chapter 2

Beam dynamics inside plasma

The particularity of the BLAST scheme requires peculiar applications of the equations that are conventionally used for plasma beam dynamics.
As we already pointed out in previous chapter and in appendices, the fields generated by a low density driver are quite different than the fields generated by an high density driver. Most of the interesting aspects for the design of a working point (accelerating gradient, maximum attainable energy, forseen energy spread) will be rigorously modelized. The discussion will point out the main advantage of the BLAST scheme: for any bunch parameters, it is possible to find an optimal injection distance for the energy spread compensation. This is quite different from the acceleration using an high density driver that doesn't depend from the bunch separation [38].
The driver transverse dynamics will be also discussed in this chapter. The lack of a complete blow-out of the electrons in the case of low brightness drivers means that the ion column model [39] (developed fully in appendix B) can not be used for the description of the transverse dynamics of driver.
After the definition of the requirements for driving bunch, we will discuss the witness dynamics for the preservation of high brightness. Emittance growth for non linearity of the fields and betatron dephasing will be introduced, pointing out the requirements of the witness for an optimal acceleration. The matching conditions for an high density witness injected on the crest of a linear wakefield will be analyzed in order to evidence how an high density witness can be focused in the crest of a linear field and why the matching conditions in that region depend weakly from the driver parameters.
All the equations derived will be used to define a procedure for the design of the working point. This procedure will be used tooptimize the working point that will be simulated in chapter 4.

2.1 Superposition principle for BLAST scheme

During the analysis of the fields in BLAST scheme we will often assume that the superposition principle can be applied in this context. We will now justify this assumption.
The superposition principle can be applied if the effect generated by the driver and witness together is the sum of the effects of the single bunches. The plasma cold fluid model is developed in Appendix A. In this model the background ions are considered motionless. The electromagnetic fields are derived from the Maxwell equations

$$\begin{aligned} &\nabla\times \vec{E} = -\frac{\partial B}{\partial t}; \\ &\nabla\times \vec{B} = \mu_0 \vec{J} + \frac{1}{c^2}\frac{\partial \vec{E}}{\partial t}; \\ &\nabla\cdot \vec{E} = -\frac{\rho}{\epsilon_0}; \\ &\nabla\cdot \vec{B} = 0; \end{aligned} \tag{2.1}$$

and generated by the motion of the free electrons that are treated as a fluid. The motion of the particles is described by the equation of motion of the electrons under the action of the Lorentz force

$$m_e\left[\frac{\partial \vec{v}}{\partial t} + \vec{v}(\nabla\cdot\vec{v})\right] = -e\vec{E} - e\vec{v}\times\vec{B}; \tag{2.2}$$

and the continuity equation

$$\frac{\partial n}{\partial t} + \nabla\cdot(n\,\vec{v}) = 0. \tag{2.3}$$

The superposition principle is always verified for electromagnetic phenomena, since the Maxwell equations are linear. For the fluid equations it is convenient to separate the contribution of the single bunches. Said n_1 and $\vec{v_1}$ the perturbation generated by the driver only and n_2 and $\vec{v_2}$ the perturbation generated by the second bunch only, we have to prove that the combined action of the bunches lead to a perturbation $n = n_0 + n_1 + n_2$ and $\vec{v} = \vec{v_1} + \vec{v_2}$ (the plasma is originally at rest so $\vec{v_0} = 0$).
We assume that the driver generates a linear field, so the second order perturbations are negligible. The equation of motion for the combined effect is

$$m_e\left[\frac{\partial \vec{v_1}}{\partial t} + \frac{\partial \vec{v_2}}{\partial t} + (\vec{v_1}+\vec{v_2})(\nabla\cdot(\vec{v_1}+\vec{v_2}))\right] = -e(\vec{E_1}+\vec{E_2}) - e(\vec{v_1}+\vec{v_2})\times(\vec{B_1}+\vec{B_2}); \tag{2.4}$$

while the continuity equation for the combined effect is

$$\frac{\partial n_1}{\partial t} + \frac{\partial n_2}{\partial t} + \nabla\cdot[(n_0+n_1+n_2)(\vec{v_1}+\vec{v_2})] = 0. \tag{2.5}$$

If the perturbation generated by the witness is smaller than the perturbation generated by the driver, the wakefield for the witness can be described by linear

equations and the superposition principle is verified. If the perturbation of the witness is much higher than the perturbation generated by driver (as occurs in the witness region), Eq.(2.4) can be written as

$$m_e \left[\frac{\partial \vec{v_1}}{\partial t} + \frac{\partial \vec{v_2}}{\partial t} + \vec{v_2}(\nabla \cdot \vec{v_2}) \right] = -e(\vec{E_1} + \vec{E_2}) - e\vec{v_2} \times \vec{B_2}; \tag{2.6}$$

while Eq.(2.5) can be written as

$$\frac{\partial n_1}{\partial t} + \frac{\partial n_2}{\partial t} + \nabla \cdot [n_0(\vec{v_1} + \vec{v_2})] + \nabla \cdot [n_2 \, \vec{v_2})] = 0. \tag{2.7}$$

The effects of the single bunches are described by the equations

$$\begin{aligned} m_e \left(\frac{\partial \vec{v_1}}{\partial t} \right) &= -e\vec{E_1}; \\ m_e \left[\frac{\partial \vec{v_2}}{\partial t} + \vec{v_2}(\nabla \cdot \vec{v_2}) \right] &= -e\vec{E_2} - e\vec{v_2} \times \vec{B_2}; \\ \frac{\partial n_1}{\partial t} + \nabla \cdot (n_0 \, \vec{v_1}) &= 0; \\ \frac{\partial n_2}{\partial t} + \nabla \cdot [(n_0 + n_2)\vec{v_2})] &= 0; \end{aligned} \tag{2.8}$$

that verify Eq.(2.6) and Eq.(2.7). So the superposition principle can be applied for the witness region.

2.2 Accelerating gradient and Transformer Ratio

High accelerating gradients that can be reached using a plasma accelerator are the main reason that makes this scheme so attractive for the future accelerating devices. The theoretical limit for the plasma wakefields intensity is the plasma breakdown limit [32]. Constraints on the beam dynamics both at the injection or inside plasma itself introduce further limitations on the effective accelerating gradient. The accelerating gradient on axis (where the accelerating field is maximum) from Eq.(1.8) far behind the driver can be written as [31]

$$E_z(0,\xi) = R(0)\sqrt{2\pi}\frac{c^2 m_e}{e}(\alpha)(k_p^2\sigma_z)e^{-k_p^2\sigma_z^2/2}\cos k_p\xi. \tag{2.9}$$

So, the plasma accelerating field in BLAST scheme is fully sinusoidal and can be written as

$$E(\xi) = E_0 \cos k_p\xi. \tag{2.10}$$

where the maximum accelerating gradient E_0 can be evaluated from Eq.(2.9). Since it depends on driver bunch shape, maximum plasma accelerating field is not preserved during the acceleration as in RF case, but generally is a function of the position of the driver inside the plasma channel s. Its analytical evolution is not trivial because it requires a self-consistent model of the driver evolution inside plasma. For this reason it is preferred to refer on simulations in order to have a reliable estimation. From Eq.(2.9) it is possible to extract some interesting features about the ideal driving bunch in order to maximize the accelerating field.
Notice that in order to keep the validity of Eq.(2.9) we must keep $\alpha \leq 1$.
Assuming a bunch with a constant shape ($\sigma_{r,z}$ =const.), we have that the accelerating field increases linearly with the normalized bunch density. Since we imposed the constraint $\alpha \leq 1$, the maximum field in linear regime corresponds to $\alpha = 1$.
Fixing α, we obtain that the accelerating field maximizes for $k_p\sigma_z = 1$ and $E_z \propto k_p\sigma_r$, leading to the consequence that $E_z \propto Q$.
Fixing α and keeping constant $k_p\sigma_r$ and $k_p\sigma_z$ the accelerating field $E_z \propto k_p$. So, in order to maximize the accelerating gradient, the plasma and driver parameters should be arranged so that:

- $k_p\sigma_z = 1$;
- $\alpha \approx 1$;
- High k_p;
- High Q.

The third and fourth conditions are limited by the possibilities of the injector. In fact, assuming the first condition we have that the bunch peak current required at the injection is $I = ck_pQ$, so the maximum accelerating gradient is limited by the peak current that can be obtained with the photo-injector. Limitations on the bunch charge are related to the plasma transverse beam dynamics that is discussed deeply in next sections.

The most significant information we derived from the optimization of the accelerating field is the formula for the injection length $k_p\sigma_z = 1$. Apparently, this is inconsistent with the evaluation of an optimal injection length for the plasma acceleration $k_p\sigma_z = \sqrt{2}$ [40]. This inconsistency is only apparent because the condition $k_p\sigma_z = \sqrt{2}$ is a consequence of the maximization of the energy extraction from the driver. The figure of merit that indicates the amount of energy extraction from a driver is the transformer ratio (RT) [35] [41]. In order to derive the RT for the BLAST scheme, we will assume a beam driven scheme composed by an electron driver followed by an electron witness with the same energy. The driver will excite the plasma and experience a decelerating field that will deplete its energy, while the witness is accelerated.
After a propagation inside plasma that can be roughly evaluated by

$$\Delta s = \frac{\gamma m_e c^2}{e|E^-_{z,max}|}; \tag{2.11}$$

where $E^-_{z,max}$ is the maximum decelerating field acting on the driver, some particles of the driver itself will become weakly relativistic, the approximation of considering $\beta \approx 1$ will be no more valid and the longitudinal distribution of the beam will change. This phenomenon is known as beam depletion (slightly different from the phenomenon of head erosion that is related to the transverse dynamics).
The beam depletion makes the beam unusable for plasma acceleration so Δs can be considered a limit on the length of the accelerator itself. During the propagation the witness will gain an energy that is function of the injection distance, as that can be easily evaluated by simple considerations over the field described in previous sections. The maximum acceleration that could be theoretically achieved can be calculated as

$$\Delta\gamma = \frac{e\Delta s|E^+_{z,max}|}{m_e c^2}; \tag{2.12}$$

where $E^+_{z,max}$ is the maximum accelerating field. The final energy of the witness can be evaluated inserting Eq.(2.11) in Eq.(2.12)

$$\gamma_f = \gamma_i(1 + R_T); \tag{2.13}$$

where we defined the transformer ratio R_T [42] as

$$R_T = \frac{|E^+_{z,max}|}{|E^-_{z,max}|}. \tag{2.14}$$

With the hypotesis of having a symmetric bunch that generates the maximum field behind the driver, it is possible to demonstrate that $R_T \leq 2$ [41].
The decelerating field in the center of the bunch is less equal than the maximum decelerating field

$$E_z(0) \leq |E^-_{z,max}|. \tag{2.15}$$

The wakefield generated behind a symmetric bunch with a separable density distribution (where $\xi \ll -\sigma_z$) can be expressed as

$$E_z(\xi) = R(0)\frac{e}{\epsilon_0}\int_{-\infty}^{+\infty} n_{b_\parallel}(\xi')\cos(k_p(\xi-\xi'))\,d\xi' =$$
$$= R(0)\frac{e}{\epsilon_0}\cos(k_p\xi)\int_{-\infty}^{+\infty} n_{b_\parallel}(\xi')\cos(k_p\xi')\,d\xi' + \tag{2.16}$$
$$+R(0)\frac{e}{\epsilon_0}\sin(k_p\xi)\int_{-\infty}^{+\infty} n_{b_\parallel}(\xi')\sin(k_p\xi')\,d\xi'.$$

For symmetric bunches, the second term of the right side of Eq.(2.16) disappears. The maximum accelerating field occurs for $\cos k_p\xi = -1$. The first term is the integral in the space of an even function. So we can write

$$|E^+_{z,max}| = 2R(0)\frac{e}{\epsilon_0}\int_{-\infty}^{+\infty} n_{b_\parallel}(\xi')\cos(k_p\xi')\,d\xi'. \tag{2.17}$$

We can also write the field in the center of the bunch as

$$E_z(0) = R(0)\frac{e}{\epsilon_0}\int_{-\infty}^{+\infty} n_{b_\parallel}(\xi')\cos(k_p\xi')\,d\xi'. \tag{2.18}$$

Inserting Eq.(2.18) in Eq.(2.17) we obtain

$$|E^+_{z,max}| = 2E_z(0) \leq 2|E^-_{z,max}|; \tag{2.19}$$

that considering the inequality Eq.(2.15) becomes

$$R_T = \frac{|E^+_{z,max}|}{|E^-_{z,max}|} \leq 2. \tag{2.20}$$

Inequality Eq.(2.20) doesn't consider the effect of a partial superposition between bunches, namely if the condition $\xi \ll -\sigma_z$ is no more valid. In these cases it is possible to have transformer ratio values that exceed 2. A direct evaluation of the RT using the fields derivated in appendix A and Eq.(2.14) give the result $R_T \approx 1.8$ assuming $k_p\sigma_z = 1$, a value that differ slightly from the maximum theoretical value. Due to all the considerations performed in this section we choosed for the BLAST scheme an injection length $\sigma_z = 1/k_p$.

2.3 Energy spread scaling

In the evaluation of the energy spread growth inside plasma the most important feature of the BLAST scheme is that the accelerating field depends both on longitudinal and transverse dimension. The coordinate system is chosen so that $\xi = 0$ corresponds to the center of witness, $\xi' = 0$ corresponds to the peak of the sinusoidal accelerating field and $\phi_0 = k_p(\xi' - \xi)$ is the injection phase of the witness bunch respect to the accelerating field. In this notation the head of the bunch is located at $\xi > 0$ and the tail is located at $\xi < 0$. We assume to have a driving bunch with a bi-gaussian distribution of the form $n(r, \xi'') = n_\perp(r) n_\parallel(\xi'')$ where

$$\begin{aligned} n_{b\parallel} &= n_b e^{-\xi''^2/2\sigma_z^2}; \\ n_{b\perp} &= e^{-r^2/2\sigma_r^2}; \end{aligned} \tag{2.21}$$

In the linear regime the accelerating field can be expressed as

$$E_z(r, \xi') = E_0 f(r) \cos(k_p \xi'); \tag{2.22}$$

where $f(r) = R(r)/R(0)$. $R(r)$ and $R(0)$ can be written as

$$R(r) = R(0) - \frac{k_p^2}{4} r^2 + \frac{k_p^2}{32\sigma_r^2} r^4 + \mathcal{O}(r^6); \tag{2.23}$$

and

$$R(0) = \left(\frac{k_p^2 \sigma_r^2}{2}\right) \left(e^{k_p^2 \sigma_r^2/2}\right) \Gamma\left(0, \frac{k_p^2 \sigma_r^2}{2}\right). \tag{2.24}$$

We define the relative energy difference of a particle of the bunch as

$$\delta = \frac{\gamma - \gamma_0}{\gamma_0} \tag{2.25}$$

where γ is the energy of the particle and γ_0 is the energy of the reference particle in the center of the witness bunch $(r, \xi) = (0, 0)$. The relative energy difference of the i^{th} particle after the acceleration can be evaluated as [43]

$$\delta_f = \delta_i + \left(1 - \frac{\gamma_0}{\gamma}\right) \left[f(r) \frac{\cos(\phi_0 + k_p \xi_i)}{\cos \phi_0} - 1 \right]; \tag{2.26}$$

where δ_i is the relative energy difference before the acceleration. Assuming negligible energy spread at the injection, we can evaluate

$$\delta_f = \left(1 - \frac{\gamma_0}{\gamma}\right) \left[f(r_i) \frac{\cos(\phi_0 + k_p \xi_i)}{\cos \phi_0} - 1 \right]. \tag{2.27}$$

From Eq.(2.26) results that the longitudinal and transverse contributions to energy spread can be separated. From now on we will refer to the expression $f(r)\frac{\cos(\phi_0 + k_p \xi)}{\cos \phi_0}$ as the field curvature. Its effect on the energy spread can be decomposed in its longitudinal and transverse components as follows. The field curvature can be approximated by the corresponding Taylor series to the second order

$$
\begin{aligned}
f(r)\frac{\cos(\phi_0+k_p\xi)}{\cos\phi_0} \approx & \frac{\cos(\phi_0+k_p\xi)}{\cos\phi_0}f(r)\Big|_{(0,0)} - \frac{\sin(\phi_0+k_p\xi)}{\cos\phi_0}f(r)\Big|_{(0,0)}k_p\xi + \\
+\frac{\cos(\phi_0+k_p\xi)}{\cos\phi_0}f'(r)\Big|_{(0,0)}r - & \frac{1}{2}\frac{\cos(\phi_0+k_p\xi)}{\cos\phi_0}f(r)\Big|_{(0,0)}k_p^2\xi^2 + \\
+\frac{1}{2}\frac{\cos(\phi_0+k_p\xi)}{\cos\phi_0}f''(r)\Big|_{(0,0)}r^2 - & \frac{\sin(\phi_0+k_p\xi)}{\cos\phi_0}f'(r)\Big|_{(0,0)}rk_p\xi = \\
=1-\tan\phi_0 k_p\xi + f'(0)r - & \frac{1}{2}k_p^2\xi^2 + \frac{1}{2}f''(0)r^2 - \tan\phi_0 f'(0)rk_p\xi.
\end{aligned}
\tag{2.28}
$$

From the definition of $R(r)$ in Eq.(2.23) we can evaluate that $f'(0) = 0$ and $f''(0) = -k_p^2/(2R(0))$. The energy difference can be written as

$$
\delta_f \approx \left(1-\frac{\gamma_0}{\gamma}\right)\left[-\tan\phi_0 k_p\xi - \frac{1}{2}k_p^2\xi^2 - \frac{k_p^2}{4R(0)}r^2\right]. \tag{2.29}
$$

The expected energy spread can be evaluated as

$$
\sigma_E = \sqrt{\langle\delta_f^2\rangle}; \tag{2.30}
$$

giving

$$
\sigma_E = \left(1-\frac{\gamma_0}{\gamma}\right)\sqrt{\tan^2\phi_0 k_p^2\sigma_{z,w}^2 + \frac{3k_p^4\sigma_{z,w}^4}{4} + \frac{3k_p^4\sigma_{r,w}^4}{16R(0)^2} + \frac{k_p^4\sigma_{r,w}^2\sigma_{z,w}^2}{4R(0)}}; \tag{2.31}
$$

where $\sigma_{r,w}$ and $\sigma_{z,w}$ are the transverse and longitudinal size of the witness. The energy spread contribution from the transverse dependency of the field scales with $k_p\sigma_{r,w}^2/R(0)$, that is plotted in Fig. 2.1 as a function of $k_p\sigma_{r,w}$ and $\sigma_{r,D}$ (driver's transverse size)

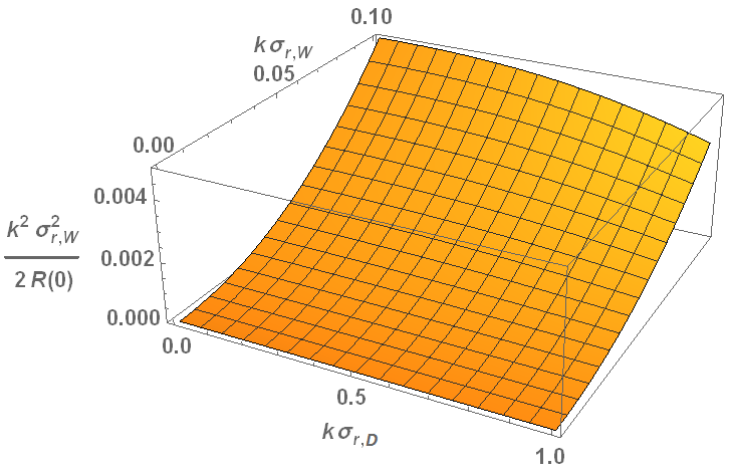

Figure 2.1. $k_p^2\sigma_{r,w}^2/R(0)$ as a function of $k_p\sigma_{r,w}$ and $k_p\sigma_{r,D}$.

Typical values for $k_p^2\sigma_z^2$ are $\approx 5 \cdot 10^{-3}$, so the transverse contribution is usually negligible for $k_p\sigma_{r,w} < 0.05$ for any value of $\sigma_{r,D}$. However, the condition $\sigma_{r,w} \ll \sigma_{r,D}$ is reccomended for the energy spread preservation. The expected energy spread to the second order of the field curvature under this assumption results to be

$$\sigma_E = \left(1 - \frac{\gamma_0}{\gamma}\right)\sqrt{\tan^2\phi_0 k_p^2\sigma_{z,w}^2 + \frac{3k_p^4\sigma_{z,w}^4}{4}}. \tag{2.32}$$

Assuming an uncorrelated energy spread at the injection we can write the outcoming energy spread as

$$\sigma_{E,f} = \sqrt{\sigma_{E,i}^2 + \left(1 - \frac{\gamma_0}{\gamma}\right)^2\left[\tan^2\phi_0 k_p^2\sigma_{z,w}^2 + \frac{3k_p^4\sigma_{z,w}^4}{4}\right]}. \tag{2.33}$$

With a negligible beam loading effect, the minimum energy spread is obtained with an injection on crest ($\tan\phi$=0). A plasma booster for energy doubling can achieve $\sigma_E < 10^{-3}$ assuming a witness length such that $k_p\sigma_z < 0.05$. Unfortunately, the conditions $k_p\sigma_{r,z} < 0.05$ and a charge of few pC produces a very high density and the beam loading contribution cannot be negligible.
The concept of BLAST scheme takes profit of the beam loading effect:

- in PWFA in linear regime the highest accelerating field region is sinusoidal;
- in order to have negligible energy spread, we must have an accelerated beam with longitudinal and transverse size higly smaller than the plasma wavelength;
- the beam loading effect generated by this kind of witness is very high for amount of witness charge $> 1pC$.

As an example we consider the case of a plasma with density $n_0 = 2 \cdot 10^{16}$. Negligible energy spreads accumulated by a beam accelerated inside plasma requires $\sigma_{z,r} \approx 2\mu$m. Even for a charge $Q \approx 300$fC, $\alpha \approx 1$ and the beam loading effect is not negligible. For non negligible beam loading effect, the treatment of energy spread changes and the conditions over the witness length become more relaxed. An analysis for the beam loading and the strategy for the energy spread compensation will be shown in next section.

2.4 Beam loading

Beam loading [30, 44] is the usual way to refer to the wakefields generated by a witness and is very useful in order to preserve the beam quality. As we already pointed out, it has been experimentally demonstrated [28] that a properly shaped witness charge distribution can help to reduce the energy spread gained by the witness itself, due to the beam loading effect.
In the first part of the section we will investigate what is the optimized injection distance in order to have the minimum energy spread considering beam loading effect in BLAST scheme.
In the second part we will evaluate what is the effect of the beam loading in terms of reduction of transformer ratio.

2.4.1 Energy spread compensation

The behaviour of beam loading in plasma linear theory 1-D has been deeply investigated in the work of Katsouleas et al. [30]. The work of Katsouleas emphasizes the influence of different kind of shapes of the witness for the energy spread. The work shows that the total compensation of energy spread can be obtained for a triangular or trapezoidal shape of the beam. For a gaussian shape of the beam, a proper injection can help to reduce the energy spread (see Fig. 2.3), but the total compensantion is not possible.
For the BLAST scheme we will assume the approximation that the fields in correspondence of the witness follow a total linear-like behaviour (basing on the results of Barov et al. [37]) and the superposition principle demonstrated in section 2.1. Assuming the presence of a beam loading effect, the energy deviation Eq.(2.25) becomes

$$\delta_f = \left(1 - \frac{\gamma_0}{\gamma}\right)\left[f(r_i)\frac{\cos(\phi_0 + k_p\xi_i) + R(r_i)Z'(\xi)/E_0}{\cos\phi_0 + R(0)Z'(0)/E_0} - 1\right]; \tag{2.34}$$

where E_0 is the maximum field generated by driver and the components of the beam loading field $R(r_i)$ and $Z(\xi_i)$ are evaluated using witness parameters. So, in order to perform an optimization of beam loading, we must know the shape of the witness bunch. We will now analyze the case of a trapezoidal witness (the longitudinal shape $n_{b\|}(\xi) = a\xi + b$ for $0 < \xi < L$ and 0 otherwise) and a bi-gaussian witness of the form Eq.(2.21).
Assuming trapezoidal witness shape, the field produced can be written as

$$\begin{aligned} R(r)Z'(\xi) &= R(r)\left[\frac{a}{k_p^2} - \frac{a}{k_p^2}\cos k_p\xi + \frac{b}{k_p}\sin k_p\xi\right] = \\ &= f(r)R(0)\left(\frac{a}{k_p^2} - \frac{a}{k_p^2}\cos k_p\xi + \frac{b}{k_p}\sin k_p\xi\right); \end{aligned} \tag{2.35}$$

where $f(r) = R(r)/R(0)$. We can write Eq.(2.35) as

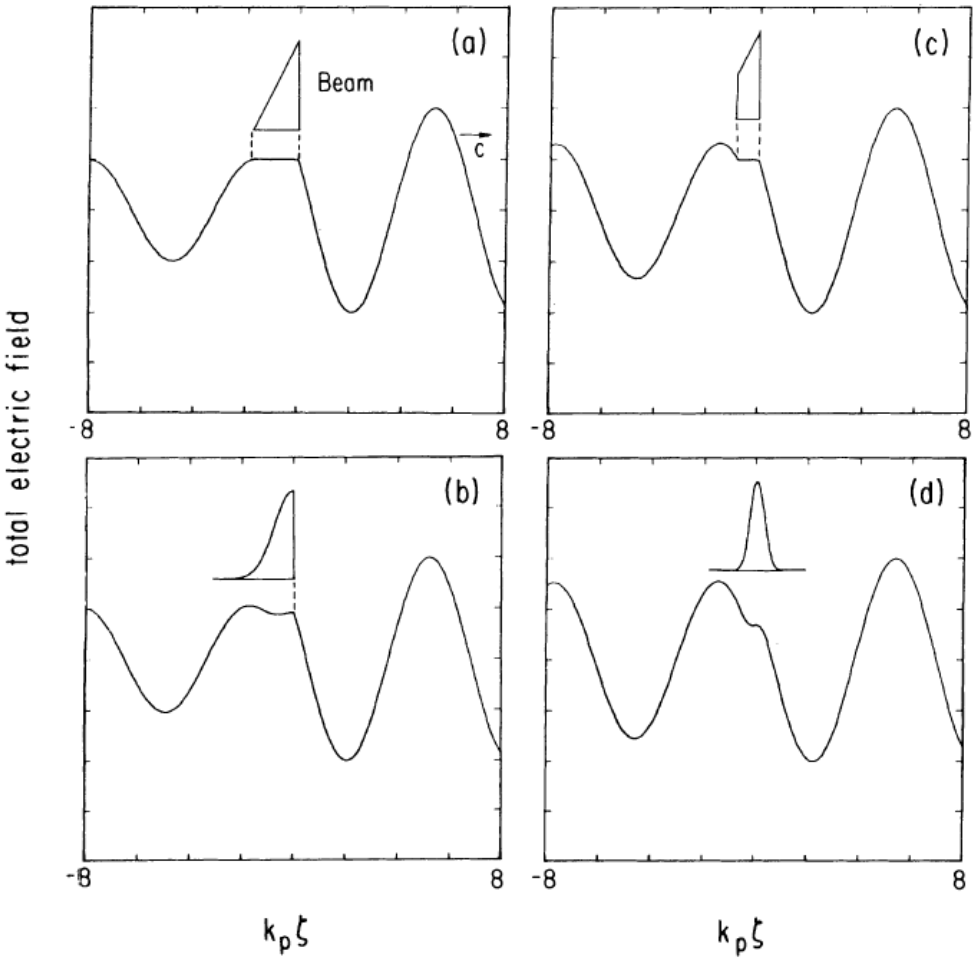

Figure 2.2. Beam loading compensation of energy spread for a triangular (a), half-gaussian (b), trapezoidal (c) and bi-gaussian (d) shaped beam. As we can see the total compensation is obtained just for triangular and trapezoidal beams from reference [30].

$$\delta_f = \left(1 - \frac{\gamma_0}{\gamma}\right)\left[f(r_i)\frac{\cos\phi_0\cos k_p\xi_i - \sin\phi_0\sin k_p\xi_i - \cos\phi_0}{\cos\phi_0} + \right.$$
$$\left. + \frac{f_w(r_i)R(0)/E_0\left(\frac{a}{k_p^2} - \frac{a}{k_p^2}\cos k_p\xi_i + \frac{b}{k_p}\sin k_p\xi_i\right)}{\cos\phi_0}\right]. \tag{2.36}$$

We used the different notations $f(r)$ and $f_w(r)$ to distinguish the functions evaluated using driver or witness parameters. In order to have the total compensation of energy spread the conditions

$$
\begin{aligned}
f(r)\cos\phi_0 &= f_w(r)\frac{R(0)}{E_0}\frac{a}{k_p^2};\\
f(r)\sin\phi_0 &= f_w(r)\frac{R(0)}{E_0}\frac{b}{k_p};
\end{aligned}
\tag{2.37}
$$

that can be verified only if the transverse shape of the beam is equal and $\sigma_{r,D} = \sigma_{r,w}$. Despite this solution guarantees the total energy spread compensation, it is very difficult to obtain such a configuration in a real accelerator [45]. The solution adopted is to have a very small transverse witness spot size. As we already have seen, this solution guarantees a negligible effect on energy spread of the fields generated by driver. From Eq.(2.23) we can see that the deviation from $R(0)$ is proportional to $k_p r$, so the effect is small for $k_p\sigma_r \ll 1$. Assuming a negligible transverse contribution, the condition Eq.(2.37) becomes

$$
\begin{aligned}
\cos\phi_0 &= \frac{R(0)}{E_0}\frac{a}{k_p^2};\\
\sin\phi_0 &= \frac{R(0)}{E_0}\frac{b}{k_p}.
\end{aligned}
\tag{2.38}
$$

Namely assuming the condition

$$
\frac{R(0)^2}{E_0^2 k_p^2}\left(\frac{a^2}{k_p^2}+b^2\right) = 1;
\tag{2.39}
$$

it is always possible to find a proper injection distance for the total energy spread compensation. Nevertheless, this condition requires a fine trapezoidal shaping of the witness and a great stability of the driver that is very difficult to obtain in a real accelerator. For the scheme we prefer to adopt a different approach. The relative energy difference assuming negligible transverse contribution ($f(r) = 1$) is

$$
\begin{aligned}
\frac{\cos(\phi_0+k_p\xi)+R(0)Z'(\xi)/E_0}{\cos\phi_0+R(0)Z'(0)/E_0}-1 \approx{}& \frac{-\sin(\phi_0+k_p\xi)-k_pR(0)Z(\xi)/E_0}{\cos\phi_0+R(0)Z'(0)/E_0}\bigg|_{\xi=0} k_p\xi+\\
&+\frac{1}{2}\frac{\cos(\phi_0+k_p\xi)+R(0)Z'(\xi)/E_0}{\cos\phi_0+R(0)Z'(0)/E_0}\bigg|_{\xi=0} k_p^2\xi^2.
\end{aligned}
\tag{2.40}
$$

In their work Chiou and Katsouleas [46] identified the condition for beam loading compensation in 1-D that the field generated by beam loading in the region of the witness has an opposite slope respect to the field generated in that region by driver. In our treatment, that condition corresponds to impose that

$$
\frac{\partial E_z}{\partial\xi} = 0;
\tag{2.41}
$$

namely that the first term of the right side of Eq.(2.40) is null. This corresponds to the following condition on the injection phase

$$\sin\phi_0 = -k_p \frac{Z(0)R(0)}{E_0}. \tag{2.42}$$

We notice that for any driver and witness parameter exists an optimal injection condition for the minimization of energy spread if

$$k_p Z(0)R(0) < -E_0; \tag{2.43}$$

that corresponds to a large range of parameters both for driver and for witness if $Q_D \gg Q_w$. Applying the condition Eq.(2.42) we obtain that the energy deviation is

$$\delta_f \approx \delta_i + \left(1 - \frac{\gamma_0}{\gamma}\right) \frac{k_p^2 \xi_i^2}{2}; \tag{2.44}$$

that corresponds to an energy spread

$$\sigma_{E,f} = \sqrt{\sigma_{E,i}^2 + \left(1 - \frac{\gamma_0}{\gamma}\right)^2 \frac{3}{4} k_p^4 \sigma_z^4}. \tag{2.45}$$

In the limit of negligible transverse contribution described in previous section, Eq.(2.45) should represent a good evaluation of the minimum of energy spread that we can get using the BLAST scheme.

2.4.2 Effective energy gain

The presence of the beam loading and its use to lower the energy spread has also the consequence of reducing the effective transformer ratio. The accelerating field experienced by a witness that follows the injection restrictions described in previous section is

$$E_{z,BL}^{+} = E_{z,max}^{+} \cos\phi_0 + Z'(0)R(0). \tag{2.46}$$

Since the beam loading field is decelerating for witness and the injection is performed near crest, we are allowed to write

$$|E_{z,BL}^{+}| = |E_{z,max}^{+}| \cos\phi_0 - |Z'(0)|R(0). \tag{2.47}$$

Dividing Eq.(2.47) for the maximum decelerating gradient of driver and we obtain

$$\frac{|E_{z,BL}^{+}|}{|E_{z,max}^{-}|} = R_T \cos\phi_0 - \frac{|Z'(0)|R(0)}{|E_{z,max}^{-}|}; \tag{2.48}$$

namely

$$R_T' = R_T \left(\sqrt{1 - k_p^2 \frac{Z(0)^2 R(0)^2}{E_0^2}} - \frac{1}{2} \frac{Z'(0)R(0)}{E_0} \right). \tag{2.49}$$

In the limit of matched driver and witness propagation (constant spot size) Eq.(2.49) can be considered a valid approximation for effective energy transfer. The conditions for stable propagation will be discussed in next sections.

2.5 Driver matching

The matching conditions for driver are necessary to prevent overfocusing at the injection (that could lead to strong increase of driver density and transition to blow-out regime) and to prevent strong emittance growth that could lead to head erosion. The head erosion effect is generated by the dependance of the focusing field from the longitudinal coordinate ξ. Different focusing fields acting on different sections of the bunch lead to different envelope evolution and to the expansion of the head where the focusing field is lower. Since the model developed is valid only for separable bunch distributions, the head erosion effect cannot be described. A self-consistent model of the driver evolution would require a reformulation of the fields for bunch distribution that are not separable. The problem will be overcome assuming the approximation that all the driver's charge is contained in the region $\xi \approx 0$. We start from the evaluation of $\langle xF_x \rangle_{ext}$ for a low density driver. Assuming a gaussian transverse distribution of the driver, we can expand it in Taylor series as

$$e^{-r^2/2\sigma_r^2} = \sum_{k=0}^{+\infty} \frac{(-1)^k r^{2k}}{2^k k! \sigma_r^{2k}}. \tag{2.50}$$

In electrostatic approximation we can apply the following equation

$$R'(r) = \frac{k_p^2}{r} \int_0^r n_{b,\perp}(r') r' dr'. \tag{2.51}$$

(demonstrated in Appendix A) in order to obtain for the transverse wake

$$E_r - cB_\theta = \frac{k_p^2}{r} Z(\xi) \sum_{k=0}^{+\infty} \int_0^r \frac{(-1)^k r'^{2k+1}}{2^k k! \sigma_r^{2k}} dr' = k_p^2 Z(\xi) \sum_{k=0}^{+\infty} \frac{(-1)^k r^{2k+1}}{2^{k+1}(k+1)! \sigma_r^{2k}}. \tag{2.52}$$

The focusing term can be evaluated as

$$e\langle x(E_r - cB_\theta)\cos\theta \rangle = \frac{1}{2\pi\sigma_r^2} \int_0^{2\pi} d\theta \cos^2\theta \int_0^{+\infty} dr e^{-r^2/2\sigma_r^2} r^2 (E_r - cB_\theta); \tag{2.53}$$

and since

$$\int_0^{+\infty} e^{-r^2/2\sigma_r^2} r^{3+2k} dr = 2^{k+1} \sigma_r^{2k+4} (k+1)!; \tag{2.54}$$

we evaluate

$$e\langle x(E_x - cB_y) \rangle = \frac{k_p^2 \sigma_r^2}{2} Z(\xi) \sum_{k=0}^{+\infty} (-1)^k. \tag{2.55}$$

The series is not convergent and it's a Grandi's series. The Cesáro summation of the Grandi's series gives the result $\frac{1}{2}$ leading to the evaluation of

$$\langle xF_x \rangle_{ext} = \frac{e k_p^2}{4} Z(\xi) \sigma_x^2. \tag{2.56}$$

Inserting Eq.(2.56) in the envelope equation

$$\sigma_x'' + \frac{p_z'}{p_z}\sigma_x' - \frac{1}{\sigma_x}\frac{\langle xF_x\rangle}{c\beta_z p_z} = \frac{\epsilon_{n,x}^2}{\gamma^2\sigma_x^3}; \tag{2.57}$$

and assuming negligible space charge we obtain

$$\sigma_x'' + \frac{p'}{p}\sigma_x' + \frac{\alpha\mathcal{Z}(\xi)}{4\gamma}k_p^2\sigma_x = \frac{\epsilon_{n,rms}^2}{\gamma^2\sigma_x^3}; \tag{2.58}$$

where we defined

$$\mathcal{Z}(\xi) = \frac{eZ(\xi)}{\alpha m_e c^2}; \tag{2.59}$$

as the longitudinal normalized plasma response function.
We notice that this expression depends on α, that for a bunch propagating inside plasma is not constant. Multiplying and dividing the third term of Eq.(2.58) for σ_x and taking into account the definition $\Lambda = \alpha k_p^2\sigma_x^2$ we obtain

$$\sigma_x'' + \frac{p'}{p}\sigma_x' + \frac{\Lambda\mathcal{Z}(\xi)}{4\gamma\sigma_x} = \frac{\epsilon_{n,rms}^2}{\gamma^2\sigma_x^3}; \tag{2.60}$$

where Λ is the normalized bunch length that is constant in paraxial approximation for ultra-relativistic bunches and does not depend on the transverse spot size. Now we adopt a trial function for the stationary solution of the form

$$\sigma_x = \sigma_0\gamma^{-1/2}; \tag{2.61}$$

with $\gamma = \gamma_0 + \gamma' z$. The envelope equation becomes

$$\frac{1}{4}\gamma'^2 + \frac{\Lambda\mathcal{Z}(\xi)}{4}\sigma_0^- 2\gamma^2 = \epsilon_n^2\sigma_0^{-4}\gamma^2. \tag{2.62}$$

A set of beam parameters that are compatible with our case study is $\gamma \approx 200$, $\epsilon_n \approx 10$ mm mrad and $\sigma_r \approx 10\mu$ m. In this case, the first term of Eq.(2.51) results negligible respect to the emittance term for an accelerating gradient < 10TV/m. So we get a matching condition of the form

$$\sigma_x = \sqrt{\frac{4}{\gamma\Lambda\mathcal{Z}}}\epsilon_n; \tag{2.63}$$

where $\mathcal{Z} = \mathcal{Z}(0)$ since we assumed that all driver charge is located in the bunch center.

2.6 Witness transverse dynamics

A treatment of the transverse witness dynamics will be now performed in order to evaluate and prevent the causes of emittance growth. This treatment makes use of the generalized Courant-Snyder theory for the beam dynamics, which is summarized in Appendix C. The main causes for emittance growth are:

- high energy spread [12];
- phase space filamentation due to non linear focusing forces [47];
- beam mismatching [48].

The first cause will be neglected because we assume to design our working points in order to mantain a low energy spread during all the acceleration. We will now furnish a brief evaluation of the second and third cause for emittance growth in the case of a plasma accelerating channel.

2.6.1 Phase space filamentation

The nonlinearities of the applied forces generate rms emittance growth due to filamentation of the trace space as showed in Fig. 4.5.

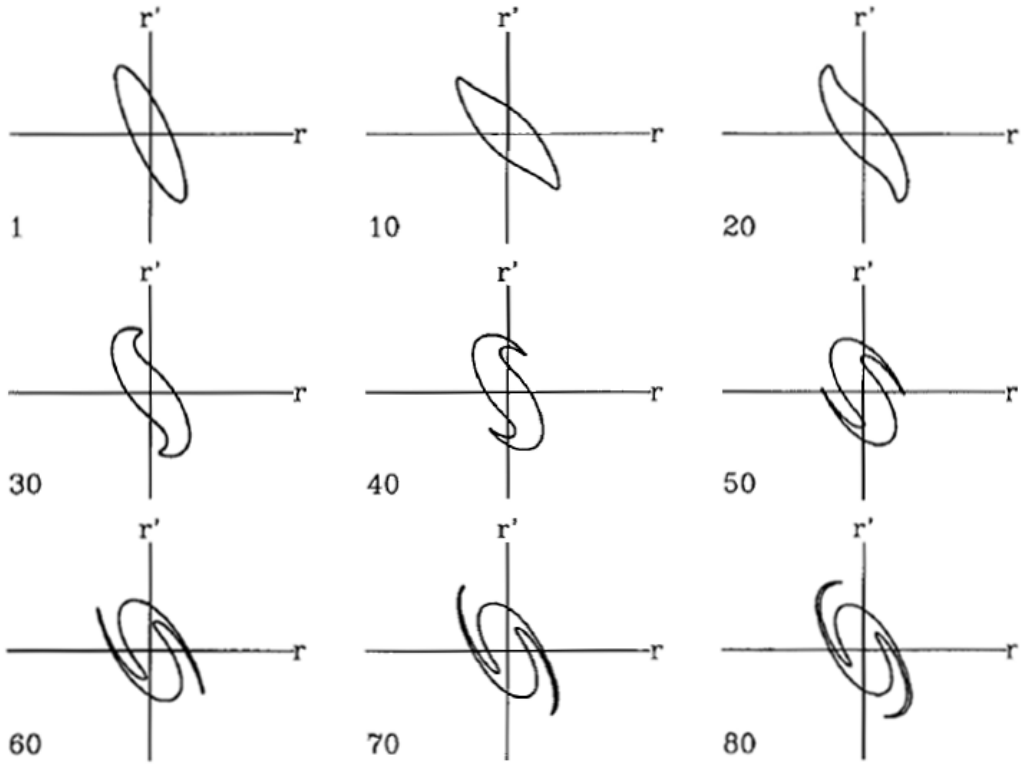

Figure 2.3. Progressive distortion of trace-space ellipse during beam propagation through a periodic channel of thin lenses with spherical aberrations [47]. The numbers associated with each figure indicate the lens periods that have been traversed.

This particular case is referred to the propagation of a beam through a periodic channel consisting of axisymmetric thin lenses with spherical aberration. The change of the slope for each particle crossing of the lens is given by

$$\Delta r' = -\frac{r}{f} - C_s r^3; \tag{2.64}$$

where f is the focal length of the lens and C_s is called spherical aberration coefficient. The field generated by a driver corresponds to a continuous focusing channel, but for our consideration it will be treated in thin lens approximation. The spherical aberration term C_s will be now evaluated for a linear driver showing how it can be minimized, avoiding emittance growth.
The action of the driver on witness can be compared to the action of a quadrupole with a force that is focusing in both planes acting on the witness. This force has both linear and non linear components, since $R'(r)$ of Eq.(1.7) can be written as

$$R'(r) = \frac{k_p^2}{2} r - \frac{k_p^2}{8\sigma_r^2} r^3 + \mathcal{O}(r^5). \tag{2.65}$$

Using Eq.(2.65) we can evaluate the spherical aberration coefficient.
We assume that the longitudinal dimension of the witness is negligible, that it is injected at a distance ξ from the driver center and that the bunchs' shape doesn't vary during the propagation. The radial equation of motion for an electron inside an electromagnetic field [47] is

$$\frac{d}{dt}(\gamma m_e \dot{r}) - \gamma m_e r \dot{\theta}^2 = -e(E_r + r\dot{\theta} B_z - \dot{z} B_\theta). \tag{2.66}$$

Assuming cylindrical symmetry and negligible B_θ Eq.(2.66) becomes

$$\frac{d}{dt}(\gamma m_e \dot{r}) = -eE_r; \tag{2.67}$$

that can be written as

$$\frac{d}{dz}(\gamma r') = -\frac{eE_r}{m_e c^2}. \tag{2.68}$$

A direct integration of Eq.(2.69) in thin lens approximation gives the result

$$\Delta r' = -\frac{eE_r}{\gamma m_e c^2} L. \tag{2.69}$$

Inserting now the field generated by a bi gaussian driver over the witness $E_r = Z(\xi) R'(r)$ in Eq.(2.69) we obtain

$$\Delta r' = -\frac{e k_p^2 Z(\xi) L}{2\gamma m_e c^2} r + \frac{e k_p^2 Z(\xi) L}{8\sigma_{r,D}^2 \gamma m_e c^2} r^3; \tag{2.70}$$

which gives as a result a spherical aberration coefficient

$$C_s = -\frac{e k_p^2 Z(\xi) L}{8\sigma_{r,D}^2 \gamma m_e c^2}. \tag{2.71}$$

The ratio between the second and the first term of Eq.(2.70) describes the importance of the spherical aberration term respect to the linear focusing. This term can be evaluated as $r^2/4\sigma_{r,D}^2$. As a consequence the spherical aberration term becomes negligible respect the focusing term when $r \ll \sigma_{r,D}$. So the witness phase space filamentation is negligible if $\sigma_{r,w} \ll \sigma_{r,D}$, the same result previously obtained in order to have a negligible transverse contribution to witness energy spread. The peculiarity of BLAST scheme derives from injection phase. Indeed, the witness is injected on the crest of the accelerating field, where $Z(\xi) = 0$. The effects of the focusing field generated by the driver in that region is negligible and as well is negligible the aberration coefficient. The effect of the self field will be evaluated in the next section.

2.6.2 Beam mismatching

Emittance growth due to beam mismatching respect to the focusing is a consequence of the correlated slice envelope oscillations [48] as shown in Fig. 2.6. Different slices of a beam injected in a focusing channel experience different phase space rotations. The emittance evaluated in the entire beam (projected emittance), that is a result of the overlapping of the phase spaces of the single beam slices, can grow as a consequence of this correlated beam envelope evolution.

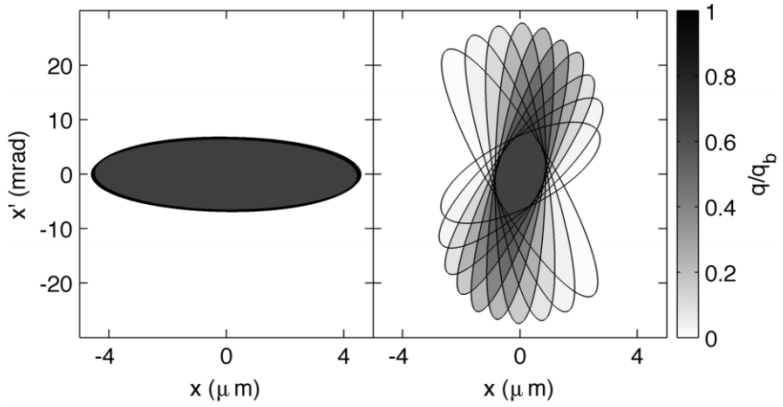

Figure 2.4. Emittance growth by betatron decoherence. The dependence of betatron phase by longitudinal dimension can lead to emittance growth as demonstrated in reference [48].

From the generalized CS theory, a beam is matched if at the injection of a focusing channel its β-function is a stationary solution of the envelope equation for the transport lattice [47]

$$\frac{1}{2}\beta\beta'' - \frac{1}{4}\beta'^2 + \beta^2 K(s) = 1. \tag{2.72}$$

In particular, assuming β_m the stationary solution of Eq.(2.72) and α and β are the Courant-Snyder functions at the injection of the plasma channel, we have that the potential maximum outcoming normalized emittance can be written as

$$\epsilon_{n,fin} = \frac{\epsilon_{n,init}}{2}\left(\frac{1+\alpha^2}{\beta^*} + \beta^*\right); \tag{2.73}$$

where $\epsilon_{n,init}$ is the beam normalized emittance at the injection and $\beta^* = \beta/\beta_m$. The necessity of a matching condition for the witness arises from this feature.
Another feature that can introduce emittance growth is a focusing force correlated in the longitudinal dimension [49]. Assume a focusing force that is linear in r and correlated in longitudinal dimension acting on a bunch through a channel of length L in thin lens approximation. From Eq.(2.69) we can write the transverse kick as

$$\Delta r' = -f(\xi)\frac{k^2}{\gamma m_e c^2} rL; \tag{2.74}$$

where k^2 is the focusing strength of the plasma and $f(\xi)$ is a function that describes the longitudinal dependance of the focusing force. We assume that $f(\xi)$ is normalized to the average value of the focusing force. In cartesian coordinates we can write

$$\Delta x' = -f(\xi)\frac{k^2}{\gamma m_e c^2} xL. \tag{2.75}$$

The slope x' can be written as

$$x' = x'_0 + \Delta x'. \tag{2.76}$$

Assuming $x'_0 = 0$ (beam with no emittance at the injection) we can write the normalized emittance at the exit of the focusing channel as

$$\epsilon_{n,x} = \sqrt{\langle x^2\rangle\langle f^2(\xi)k^4x^2\frac{L^2}{c^2}\rangle - \langle x^2 f(\xi)k^2\frac{L}{c}\rangle^2}; \tag{2.77}$$

namely

$$\epsilon_{n,x} = k^2\sigma_x^2\frac{L}{c}\sqrt{\langle f^2(\xi)\rangle - \langle f(\xi)\rangle^2}; \tag{2.78}$$

that, since $f(\xi)$ is normalized to the average focusing force acting on the bunch ($\langle f(\xi)\rangle = 0$) becomes

$$\epsilon_{n,x} = k^2\sigma_x^2\frac{L}{c}\sqrt{\langle f^2(\xi)\rangle}; \tag{2.79}$$

The meaning of Eq.(2.79) is that a dependency on the longitudinal position of the focusing force introduces emittance growth. In order to preserve emittance it is necessary to have the condition

$$\frac{\partial(E_r - cB_\theta)}{\partial\xi} = 0. \tag{2.80}$$

In the next section we will see that this condition is verified for the BLAST scheme.

2.7 Witness matching

In this section we will invetigate the matching conditions of a witness injected in the wake of a low density driver. We start from the assumption that the beam loading is negligible, showing that, in this case, a witness injected on crest can not be matched because in the crest of a linear plasma wakefield there is no focusing field.
Further we will introduce the condition of high beam loading and we will point out that the matching near crest region doesn't depend on driver. For all considerations we will perform in this section, we will assume to have an ultra-short and narrow witness ($k_p\sigma_{r,z} \ll 1$) the keep energy spread low. We will also assume that the transverse spot size of the witness is very smaller than the driver.
For the evaluation of the fields in the case of negligible beam loading, we will start from the equation for local plasma density generated by a driver in linear regime

$$n_1(\xi, r) = -\frac{\epsilon_0 k_p^2}{e} Z(\xi) n_{b\perp}. \tag{2.81}$$

If $k_p\sigma_z \ll 1$ we can assume that the beam will experience the same focusing field ($Z(\xi)$ is constant for the entire witness length). Writing $n_{b\perp}$ as its Taylor expansion, Eq.(2.81) becomes

$$n_1(\xi, r) = -\frac{\epsilon_0 k_p^2}{e} Z(\xi) \left(1 - \frac{1}{2\sigma_{r,D}^2} r^2 + \mathcal{O}(r^4);\right). \tag{2.82}$$

If $\sigma_{r,w} \ll \sigma_{r,D}$ we can consider only the linear term of Eq.(2.82), namely the local deviation of the plasma density becomes a function of the longitudinal position only

$$n_1(\xi) = -\frac{\epsilon_0 k_p^2}{e} Z(\xi). \tag{2.83}$$

If the effect of the beam loading is negligible, we can treat this region as a uniformly charged cylinder with a positive charge $n_p = -n_1$. From this considerations it is possible to evaluate E_r as

$$E_r = \frac{k_p^2 Z(\xi)}{2} r; \tag{2.84}$$

and inserting inside the envelope equation we get

$$\sigma_x'' + \frac{\gamma'}{\gamma}\sigma_x' + \alpha_D \mathcal{Z}(\xi)\frac{k_p^2}{2\gamma}\sigma_x = \frac{\epsilon_n^2}{\gamma^2\sigma_x^3}. \tag{2.85}$$

Assuming a trial function of the form $\sigma_x = \sigma_0\gamma^{-1/4}$ end a constant accelerating gradient $\gamma = \gamma_0 + \gamma' z$, we get

$$\frac{1}{16}\gamma'^2\sigma_0 + \alpha_D \mathcal{Z}(\xi)\frac{k_p^2}{2}\sigma_0\gamma = \frac{\epsilon_n^2}{\sigma_0^3}\gamma. \tag{2.86}$$

The first term can be neglected for accelerating gradients lower than several TV/m, so we get stationary solution

$$\sigma_x = \sqrt[4]{\frac{2}{\alpha_D \mathcal{Z}(\xi)\gamma}}\sqrt{\frac{\epsilon_n}{k_p}}. \tag{2.87}$$

Eq.(2.87) admits a real finite solution for $\mathcal{Z}(\xi) > 0$ (focusing region). The region of crest corresponds to $\mathcal{Z}(\xi) \approx 0$ and to very high values of matched spot sizes that is useless fo acceleration.
The field generated by narrow and ultra-short bunches in high density regimes has been object of several studies [50, 37, 51]. In BLAST scheme the witness is injected near crest of accelerating wakefield of a low density driver at the optimized bunch separation that guarantees the beam loading compensation of energy spread. So in order to describe the transverse field acting on witness we can introduce the constraint that $\frac{\partial E_z}{\partial \xi} = 0$ from Eq.(2.41). The consequence of this constraint that we will now demonstrate that assuming a very high witness density $\alpha \gg 1$, the witness can match in its own wake. We will also demonstrate that in order to evaluate the matching we can also apply the ion column model assuming a plasma density $n = n_0/2$. The corresponding matching condition results to be

$$\sigma_x = \sqrt[4]{\frac{1}{\gamma}}\sqrt{\frac{2\epsilon_n}{k_p}}. \tag{2.88}$$

The ion column model can be applied if in the witness region the plasma current density $\vec{J} = 0$ and that the local plasma density ρ is constant. The condition $J_z = 0$ has been proved rigorously by Ref. [34] for low density and low charge beams. In order to prove $J_r = 0$, we start from the r component of the Ampere's law

$$\frac{\partial B_\theta}{\partial \xi} = -\mu_0 J_r + \frac{1}{c}\frac{\partial E_r}{\partial \xi}; \tag{2.89}$$

and from the θ component of Faraday law

$$\frac{\partial E_r}{\partial \xi} - \frac{\partial E_z}{\partial r} = c\frac{\partial B_\theta}{\partial \xi}. \tag{2.90}$$

Combining Eq.(2.89) with Eq.(2.90) we obtain for the accelerating field

$$\frac{\partial E_z}{\partial r} = \mu_0 c J_r. \tag{2.91}$$

The first derivative respect to ξ of Eq.(2.91) is

$$\frac{\partial}{\partial r}\frac{\partial E_z}{\partial \xi} = \mu_0 c\frac{\partial J_r}{\partial \xi} = 0; \tag{2.92}$$

since we assumed the beam loading compensation Eq.(2.41). After the passage of the witness there is total blow out since we assumed ultra-high witness density. Inside the blow-out region $J_r = 0$ because the ions are motionless. For Eq.(2.92) we have that J_r doesn't vary from the blow-out region to the witness region, so in witness region $J_r = 0$ and therefore $\vec{J} = 0$.
In order to prove that ρ is constant in witness region, we have to prove that $\frac{\partial \rho}{\partial r} = 0$ and $\frac{\partial \rho}{\partial \xi} = 0$. Maxwell equations can be combined in order to obtain

$$\frac{1}{r}\frac{\partial}{\partial r}[r\,(E_r - cB_\theta)] = \frac{\rho}{\epsilon_0} - \mu_0 c J_z. \tag{2.93}$$

Assuming both $J_z = 0$ and linear behaviour in r of the focusing fields [37] for small values of r, $\frac{\partial \rho}{\partial r} = 0$ is verified since the left side of Eq.(2.93) results to be constant respect to r.
In order to prove that $\frac{\partial \rho}{\partial \xi} = 0$, we apply the Panofsky-Wenzel theorem to Eq.(2.91) in order to obtain

$$\frac{\partial(E_r - cB_\theta)}{\partial \xi} = \mu_0 c J_r. \tag{2.94}$$

Now deriving Eq.(2.93) respect to ξ we obtain

$$\mu_0 c \frac{1}{r}\frac{\partial}{\partial r}(r J_r) = \frac{1}{\epsilon_0}\frac{\partial \rho}{\partial \xi} = 0; \tag{2.95}$$

since we have already proven that $J_r = 0$.
We have now to evaluate the local plasma density in the witness region in order to apply the ion column model. It can be easily evaluated from the assumption of ultra-short beam ($k_p \sigma_z \ll 1$) and considerations of Ref. [51]. According to Stupakov et al., the density on axis generated by a bunch can be treated as an Heaviside step function

$$n = n|_{\xi \to 0+} \Theta(\xi). \tag{2.96}$$

In the crest region of the accelerating field generated by a low density driver the local electron density is equal to the background density, so $n|_{\xi \to 0+} = n_0$. The plasma density inside the bunch so can be written as

$$n = n_0 \Theta(0) = n_0/2. \tag{2.97}$$

Inserting Eq.(2.97) in Eq.(2.93) it is possible to evaluate the focusing field as

$$E_r - cB_\theta = \frac{n_0 e}{2\epsilon_0} r. \tag{2.98}$$

Inserting the focusing field Eq.(2.93) in the envelope equation, the resulting matching condition is given by Eq.(2.87).
It is also interesting to notice that since

$$\frac{\partial(E_r - cB_\theta)}{\partial \xi} = \mu_0 c J_r; \tag{2.99}$$

The condition of beam loading compensation corresponds to the condition that we found for minimum emittance growth Eq.(2.80).

2.8 BLAST working point design

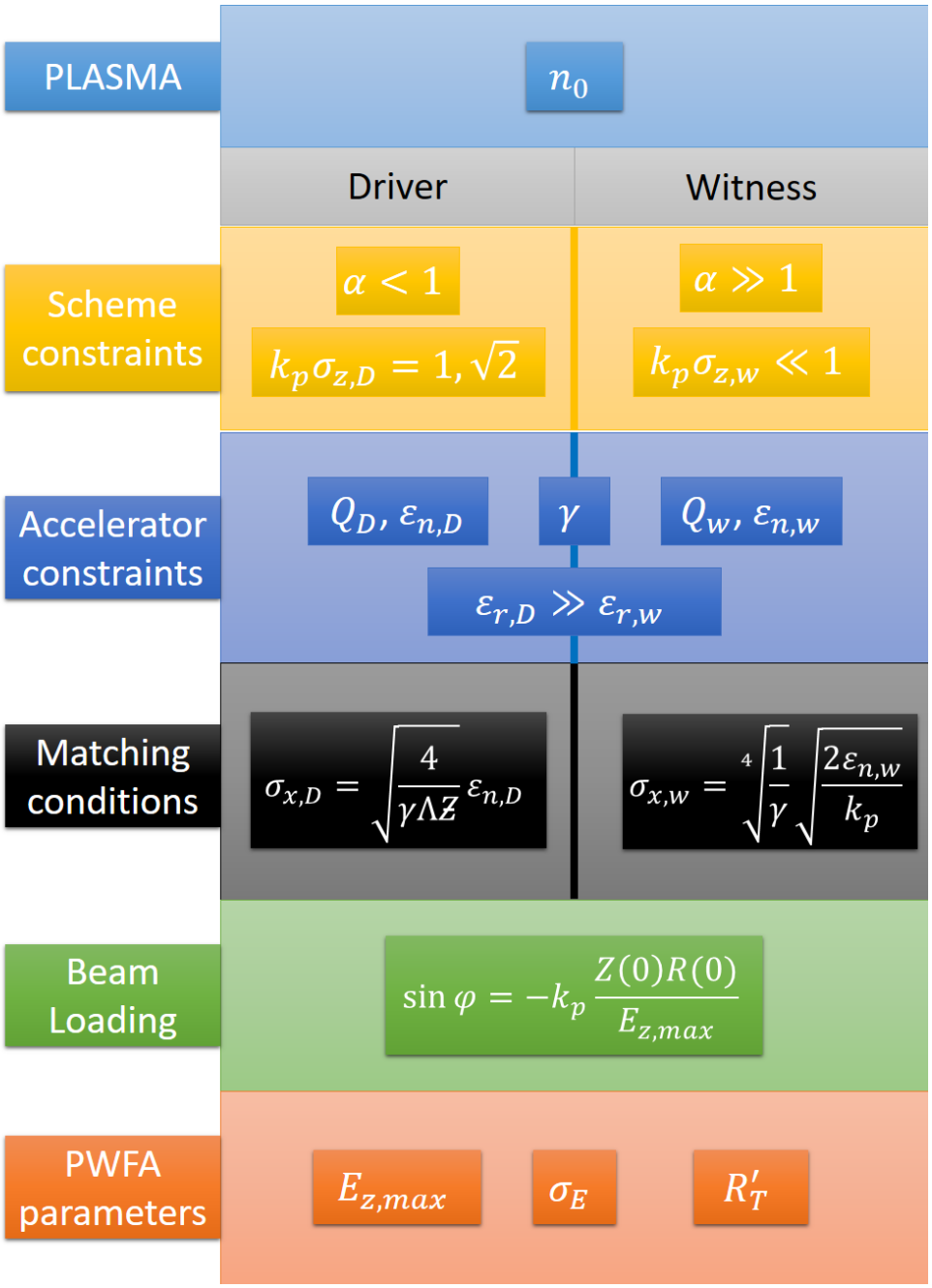

Figure 2.5. Design procedure for BLAST scheme working points. Extensively explained in section (2.8).

The working point optimization results from the following considerations:

- **Plasma density**: plasma density n_0 is decided arbitrarily, according to the possibilities of injector in order to have $k_p\sigma_z \ll 1$; the choice should be

consistent with the requirements about witness energy spread at the exit of the plasma accelerator that can be evaluated through Eq.(2.33);

- **Bunch density**: all the following beam parameters have to be arranged such that $\alpha_D < 1$ and $\alpha_w \gg 1$;
- **Bunch length**: driver's length $\sigma_{z,D}$ is chosen according to the kind of scheme; for high transformer ratio scheme $k_p\sigma_z = \sqrt{2}$, while for high accelerating gradient scheme $k_p\sigma_z = 1$; for the witness $k_p\sigma_z \ll 1$ is necessary to reduce forseen energy spread;
- **Bunch charge**: driver and witness charges $Q_{D,w}$ are decided according to the possibility to obtain the desired bunch densities;
- **Spot constraint**: $\sigma_{r,D} \gg \sigma_{r,w}$ is necessary to avoid transverse energy spread and phase space filamentation; assuming the β-functions at the injection $\beta_{r,D} \approx \beta_{r,w}$ this condition reduces to $\epsilon_{n,D} \gg \epsilon_{n,w}$;
- **Matching conditions**: the spot sizes at the injection are defined by the matching conditions Eq.(2.63) and Eq.(2.88);
- **Injection distance**: the optimal injection phase is defined by Eq.(2.42).

After the working point definition it is possible to evaluate the maximum accelerating gradient and the transformer ratio.
Now we will use the procedure to design an high gradient working point.
Assume to have an injector that can produce driver bunches with an outcoming energy $\gamma = 200$, a charge $Q = 200$pC and a length $\sigma_z = 40\mu$m.
The condition $k_p\sigma_z = 1$ brings to the choice of a plasma density $n_0 = 2 \cdot 10^{16}\text{cm}^{-3}$ that corresponds to a driver length $\sigma_z = 37.2\mu$m.
In order to have high gradient we choose a normalized bunch density $\alpha = 1$.
From the bunch density $n_b = 2 \cdot 10^{16} = \dfrac{Q/e}{\pi^{3/2}\sigma_z\sigma_r^2}$ we can evaluate the transverse spot size value and gives the result $\sigma_r = 10.3\mu$m.
The ideal emittance of the driver is evaluated from the matching condition Eq.(2.94) and results to be $\epsilon_n = 17$mm mrad.
We choose for the witness a charge $Q = 10$pC, a length $\sigma_z = 3\mu$m the emittance $\epsilon_n = 0.3$mm mrad according to the injector possibilites.
Witness injection spot size is evaluated through the matching condition Eq.(2.101) $\sigma_r = 1.26\mu$m.
Witness normalized bunch density results $\alpha \approx 40$.
Neglecting beam loading we expect an accelerating gradient ≈ 2GV/m and an accelerating length for the energy doubling $L \approx 5$cm.
The evaluated transformer ratio $R_T \approx 1.5$.
Assuming an energy spread at injection $\sigma_{E,i} = 0.001$ the forseen energy spread at the extraction for energy doubling is $\sigma_{E,f} = 0.003$ with an increase of 0.002. The asymptotic value is 0.006.

Chapter 3

The SPARC_LAB test facility

In this chapter we will present the SPARC_LAB test facility [52], where the working points for high quality PWFA experiments studied in this thesis will be tested and verified.

SPARC_LAB is based on the unique combination of high brightness electron beams, from the SPARC photoinjector [53] with high intensity ultrashort laser pulses, from the FLAME laser system [54]. The joint presence of these two systems allows the investigation of plasma acceleration with different configurations, i.e. self and

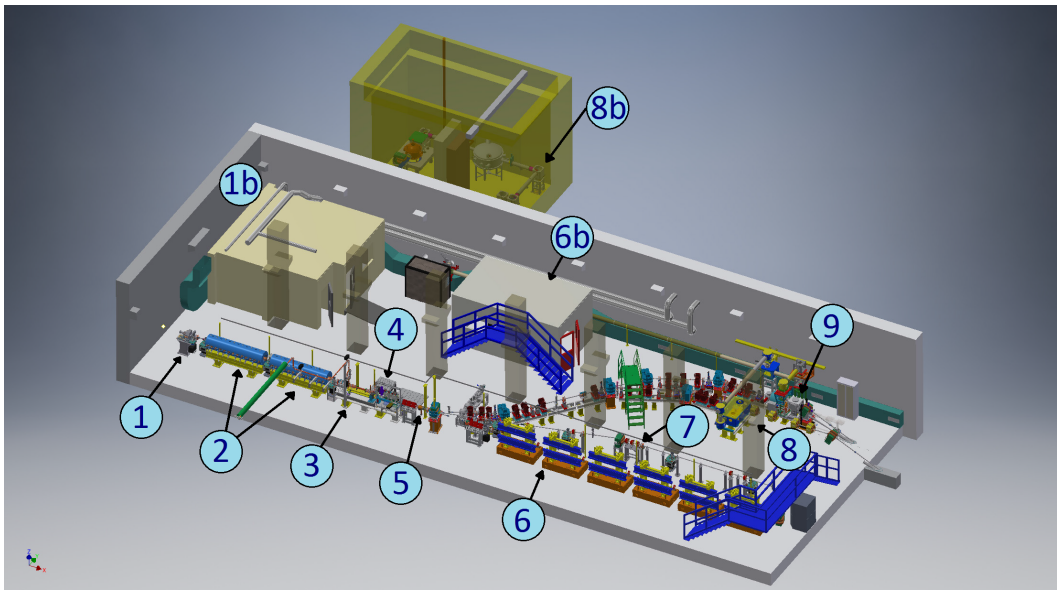

Figure 3.1. SPARC_LAB layout. From left: the electron-gun (1) driven by the photocathode laser (1b), followed by the two TW S-Band accelerating sections (2) and the TW C-Band accelerating section (3). The beam driven experiment chamber (4; Fig. 4.2). RFD (5). After the RFD a couple of dipoles can send the beam to four different beam lines: FEL physics beam line (6), that can work both in SASE and in seeded using the (6b) schemes, diagnostic beam line (7), external injection experiment beam line (8), where the wake is generated by a laser pulse coming from FLAME laser (8b) and the witness is injected externally, and Thompson backscattering line (9).

external injection [55], laser and particle beam driven [56].
In addition, these two cutting-edge systems allows the generation of advanced radiation sources, such as FEL in different exotic schemes [57, 58, 59], broad [60] and narrow [61] band high peak power THz radiation, and x-rays from Thomson backscattering [62]. Fig. 3.1 shows the photo-injector and the four beamlines. The first beam line (Fig. 3.1/6) hosts the undulators. The second line (Fig. 3.1/7) is dedicated to the test of advanced beam diagnostic. The third line (Fig. 3.1/8) is dedicated to external injection experiment. The fourth line (Fig. 3.1/9) is dedicated to the Thompson backscattering experiment.

3.1 Photo-injector

The SPARC_LAB photo-injector is composed of a 1.6 cell BNL/UCLA/SLAC type gun, operating at S-band ($2.856GHz$) with a peak field of 120MV/m on the copper metallic photocathode that generates a 5.6MeV electron beam. The gun is then followed by two S-band and one C-band travelling wave (TW) sections whose accelerating gradient can boost the beam energy up to 180MeV. The first S-band cavity is also used as RF compressor in velocity bunching regime [63], setting the beam injection phase near to zero crossing. The first two S-band sections are surrounded by solenoid coils that can provide a magnetic focusing to better control the beam envelope and the emittance oscillations under RF compression. A diagnostics transfer line, located downstream a dipole, allows to fully characterize the accelerated beam.

3.2 Plasma beam driven chamber

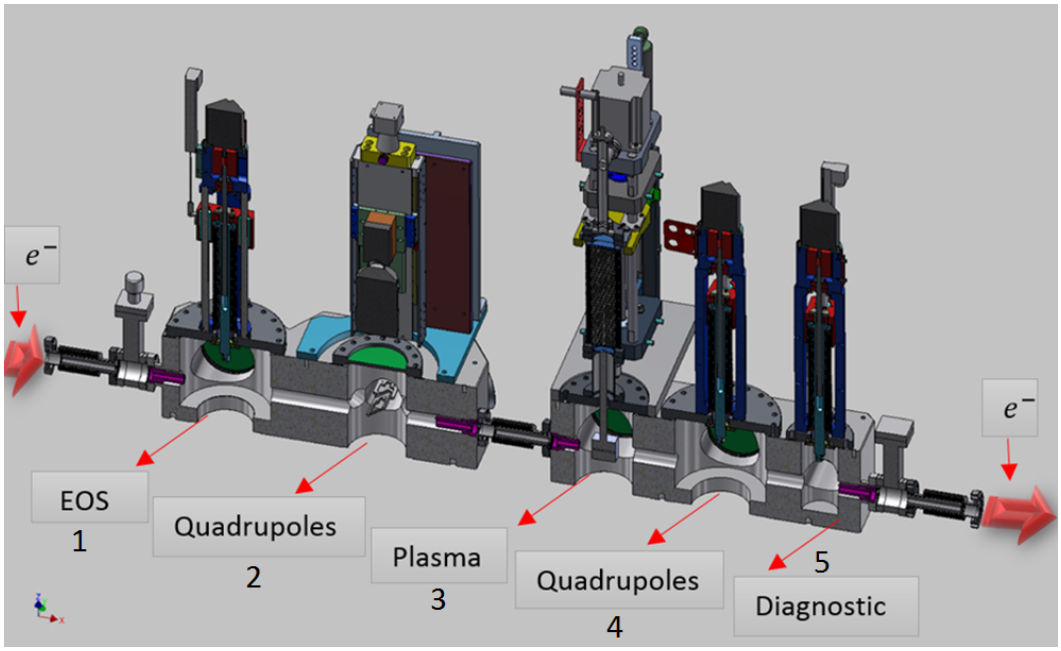

Figure 3.2. The plasma beam driven chamber. Eos (1), injection (2) and extraction (4) permanent magnet quadrupole triplets, plasma capillary (3) and THz diagnostic.

The plasma beam driven chamber has been designed to host the plasma channel system, transverse and longitudinal diagnostics, and permanent quadrupole magnets, both to match the beam at the vacuum-plasma interface and at the extraction from plasma.
A structure composed by a capillary filled with hydrogen and ionized by an high voltage discharge circuit [64] was chosen in order to create a pre-ionized plasma channel. The apparatus was supposed to work with a repetition rate $1 - 10$Hz very close to the C-band accelerating cavity, so the chamber was also designed taking into account the necessity of high quality of the vacuum. The control over the beam dynamics is necessary because bunch parameters at the injection have a strong impact on the plasma beam dynamics that, in turn, is of primary importance for the quality of the outcoming beam. As a consequence, also a proper diagnostics before the plasma channel is of important to verify if the requirements on the beam transport line are fulfilled. The same kind of diagnostic applied after the plasma channel is essential to verify the effects of plasma acceleration over the beam.
The beam transverse diagnostics is performed using an optical transition radiation (OTR) system.
The longitudinal beam profile can be evaluated using different diagnostic systems, described in the next section. In order to grant these requirements, the plasma beam driven chamber (shown in Fig. 3.2) was designed as follows.
The first section holds the EO-based diagnostics [65] (Fig. 3.3/1), the second and fourth section hold permanent magnet quadrupoles for injection and extraction (Fig. 3.2/2, 3.2/4) the third section holds the plasma capillary section (Fig. 3.2/3) and

the fifth section holds a THz diagnostic system (Fig. 3.2/5). The whole chamber is mounted on a powered handling in order to allow a fine alignment of the plasma channel with the irises and the beams' orbit.

3.3 Longitudinal diagnostic

In order to perform beam longitudinal profile measurements the SPARC_LAB facility is equipped with an electro-optical sampling (EOS) diagnostic, a terahertz (THz) diagnostic and an RF-deflector (RFD).
The EOS diagnostic is located inside the plasma chamber, before the plasma capillary and allows to evaluate the longitudinal beam profile using a single shot not intercepting measurement with a resolution of $\approx$ 50fs. This collocation was chosen in order to provide a single shot online measurement of longitudinal distribution before the acceleration, in particular to monitor the distance between driver(s) and witness.
The THz diagnostic is located inside the plasma chamber, downstream the plasma. It is a multi-shot measure device (both intercepting and non intercepting depending on configuration) that allows to evaluate the longitudinal beam profile with a resolution of about 10fs. The THz measurement device can be used also as a THz source and it was placed downstream the plasma acceleration channel in order to make feasable a plasma driven THz source.
The RFD system [66] is located after the plasma interaction chamber. It is an intercepting measurement device that allows to evaluate the longitudinal profile of a beam with a resolution of 30fs. The combination of the RFD with a bending magnet, located downstream on the transport line, allows to perform direct measurements of the longitudinal phase space.
All the diagnostics are described in detail in the corresponding sub-sections.

3.3.1 Electro-optical sampling longitudinal diagnostics

The technique of electro-optical sampling (EOS) is used to reconstruct the longitudinal charge distribution of a propagating bunch using non linear crystals placed near the moving electron beams [65]. The temporal resolutions reached are determined by the width of the optical laser puls and the EO crystal length and is usually very high. The working principle is based on the birefringence in a non linear crystal (like ZnTe and GaP), induced by the high electric fields of the relativistic electron bunch, which propagate in the crystal like a THz-field (see Fig. 3.3) and that are a function of time ($E_b(t)$). Due to the action of this electric field, the crystal becomes anisotropic (biaxial). The electric field of a polarized laser passing through the crystal is decomposed along the two optical axes, with characteristic refractive indices $n_i = n_1, n_2$ respectively. Therefore, the two components travel at different velocities $v_i = c/n_i$. At the end of the crystal their relative phase delay Γ is

$$\Gamma(t) = \frac{\omega d}{c}(n_1 - n_2) \propto E_b(t); \tag{3.1}$$

where ω is the laser pulse frequency and d is the crystal thickness. Therefore the time information contained in $\Gamma(t)$ is a replica of $E_b(t)$.

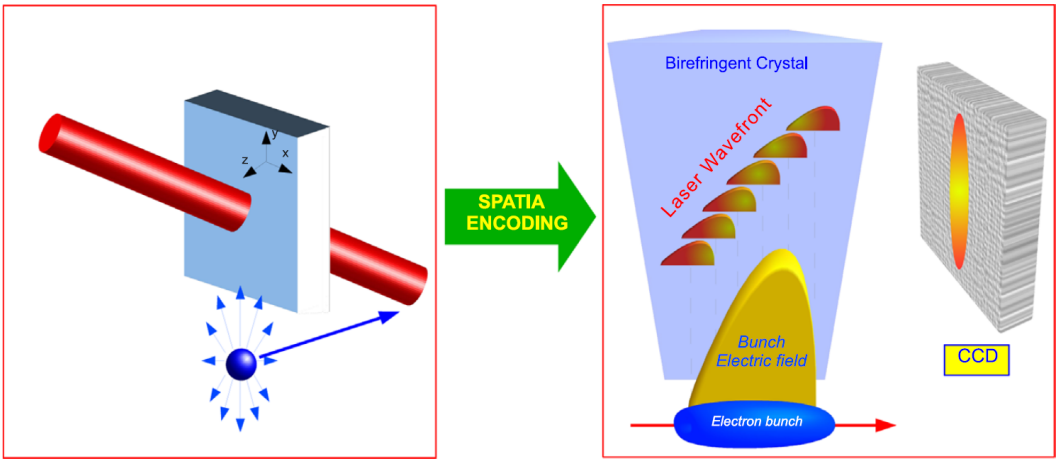

Figure 3.3. Spatial decoding for the Electro-optic Sampling. The laser crosses the EO crystal with angle $\theta = 30°$. By inserting a polarizer whose axis is 90° with respect to the laser linear polarization, the longitudinal bunch profile is directly retrieved on the CCD.

At the SPARC-LAB facility a Ti:Sa IR laser ($\lambda = 800$ nm, 130 fs pulse length, rms) is used to sample the birefringence which is induced in the non linear optical crystal by the co-moving electric field of the electron bunch. The laser is derived from a splitting of the photocathode's laser pulse. This configuration allows to obtain a natural synchronization with the electron beam, having a repetition rate of 10 Hz. The initial linear polarization of the laser pulse is converted into a slightly elliptical polarization. The polarization is then converted into an intensity modulation by placing a polarizer after the crystal. The polarization axis of the polarizer is rotated by 90° with respect to the initial laser polarization. To encode the bunch longitudinal profile into the laser, we used the spatially encoding EOS technique, in which the laser crosses the non linear crystal with an angle of $\theta = 30°$ (see Fig. 3.3). In such a way, being x the spatial coordinate along the laser transverse profile and t the time coordinate for the longitudinal bunch profile, we have

$$t = \frac{x}{c}\tan(\theta); \tag{3.2}$$

where c is the vacuum speed of the light. From Eq. 3.2, the total time window Δt is directly proportional to the laser spot diameter d, i.e. $\Delta t = (d/c)\tan(\theta)$.

3.3.2 THz diagnostics

Radiation extending up to the THz range can be generated as coherent radiation from ultra-short (sub-picosecond) electron bunches. In the approximation that a radiation process has a characteristic temporal emission very lower than a particle bunch duration, it can be used to retrieve the longitudinal electron beam charge distribution by studying its coherent spectrum. The transition radiation (TR) is used for this purpose because it is a surface phenomenon that for our purposes can be considered instantaneous. TR is produced when a relativistic charged particle crosses the interface between two media with different dielectric properties. The full theory of TR is fully described in ref. [67]. A single particle with a normal

incidence on a surface has a spectral angular distribution that can be described by the formula

$$\frac{d^2 I_{sp}}{d\omega d\Omega} = \frac{e^2}{4\pi^3 \epsilon_0 c} \frac{\beta^2 \sin^2\theta}{(1-\beta^2\cos^2\theta)^2}; \tag{3.3}$$

with c the speed of light, e the electron charge, $\beta = v/c$ where v is the electron velocity and θ, in case of normal incidence, is the angle between the particle trajectory and the observer. Because of the backward-emitted radiation is proportional to the reflection coefficient of the media, metallic screens with high reflectivity (e.g. aluminum) are tipical choices for the THz devices. For instance, the plasma frequency of aluminum is 3.55×10^3 THz, which corresponds to a wavelength of about 85 nm. Ideally, frequencies that are below the plasma frequency are completely reflected by the metal. In real cases, the reflection can be considered almost complete just for frequencies far below that value, therefore in infrared and far infrared spectrum, the absorption and transmission is negligible and the waves can be considered totally reflected. The formula from Eq.(3.3) is known as Ginzburg-Frank formula. In most practical cases the Ginzburg-Frank equation is not applicable because two basic pre-assumptions of the analytic derivation are not fulfilled: the radiation screens used in an accelerator are of limited size, and the radiation is usually observed in the near-field and not in the far-field regime [68]. However, in the limits of validity of the formula in Eq.(3.3), the spectral angular distribution of single-particle TR radiation does not present any dependence on the radiation frequency. The particles of a bunch with finite longitudinal and transverse dimension emit a radiation field with the same amplitude. The relative phase depends only on the position occupied by the single particle inside the bunch and on the direction of the observation. The spectral angular distribution produced by a relativistic electron beam can be written as

$$\frac{d^2 I}{d\omega d\Omega} = \frac{d^2 I_{sp}}{d\omega d\Omega}(N + N(N-1)F(\omega)); \tag{3.4}$$

with $\omega = 2\pi c/\lambda$ the angular frequency of the emitted light and N the number of electrons in the bunch. $F(\omega)$ is the so-called bunch longitudinal form factor defined as the square of the Fourier transform of the normalized longitudinal particle distribution within the bunch, $S(z)$,

$$F(\omega) = |\int S(z) e^{+i\frac{\omega}{c}\hat{n}\cdot\hat{z}} dz|^2; \tag{3.5}$$

where $\hat{z}$ is the unit vector towards the observation point, and the integral is performed along the longitudinal direction z. We can evaluate from Eq.(3.5) that at $\lambda < \sigma_z$, $F(\omega) \approx 0$ while at $\lambda > \sigma_z$, $F(\omega) \approx 1$, where $\lambda = 2\pi c/\omega$ is the wavelength of the emitted radiation and σ_z is the bunch length. Two terms contribute to the total intensity of Eq.(3.4): the first one, proportional to the number of particles N, is the total intensity if the particles radiate all incoherently, each behaving independently one from the other. The second one dominates at wavelengths λ larger than the bunch length, for which the N particles can be treated as a single macro-particle in which all particles emit radiation coherently at the same phase and so the field

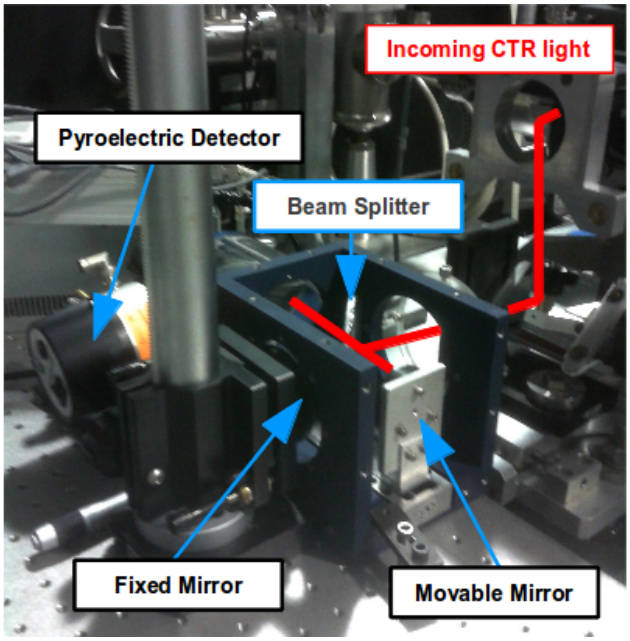

Figure 3.4. Michelson Interferometer.

amplitudes add with constructive interference and the intensity scales quadratically with the number of electrons per bunch, i.e. N^2. Since the bunch longitudinal form factor in Eq.(3.5) is typically zero for $\lambda < \sigma_z$, the coherent TR (CTR) spectrum is enhanced (with respect to incoherent spectrum) by N^2 when $\lambda > \sigma_z$. In the SPARC_LAB layout, the CTR spectrum is measured using interferometer techniques (in Fig. 3.4 a Michelson interferometer setup is shown).

3.3.3 RF Deflector

One of the most estabilished diagnostics techniques for the full longitudinal characterization of beam parameters for LINACs is the use of RF deflectors (RFD). This device allows to perform measurents the bunch longitudinal profile and adding a dispersive system (i.e. a magnetic dipole) also direct measurements of the longitudinal phase space (LPS) [53].
The RFDs make use of a transverse voltage that is a function of time ($V_{defl}(t)$) in order to force a correlation between the longitudinal position of the particle inside the bunch (t_B) and the transverse one (usually vertical) at the screen position (y_S) [69]. At SPARC_LAB the screen consists in a Ce:YAG radiator, whose produced light is collected by a CCD camera. The phase of the deflecting voltage is chosen to have a zero crossing of the transverse voltage in the center of the bunch, giving a linear transverse deflection from the head and the tail of the bunch itself. The displacement introduced to the single slice by the transverse deflector results to be proportional to the longitudinal distance of the slice respect to the center of the bunch.The mechanism is illustrated in Fig. 3.5.
Since the single slices of the beam have a finite transverse emittance, the distributin of the deflected bunch at the screen position is the superposition between the deflected

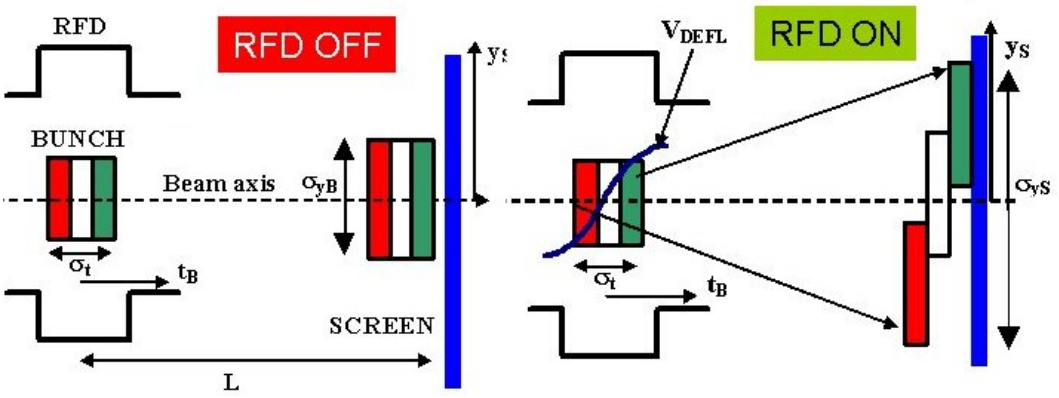

Figure 3.5. Longitudinal to transverse correlation induced by the RFD transverse voltage.

beam profile and the transverse size of each bunch slice. Under the assumption that all longitudinal slices have the same transverse dimension on the screen (σ_{yB}) and that there is a drift (L) between the RFD and the screen, the total vertical rms distribution (σ_{yS}) at the screen is given by

$$\sigma_{y,S}^2 \approx K_{cal}\sigma_{tB}^2 + \sigma_{yB}^2; \tag{3.6}$$

where $K_{cal} = (V_{defl}/E)\omega_{RF}L$, ω_{RF} is the angular frequency of the deflecting voltage and E is the beam energy in eV units. From this formula one can define the resolution length σ_{tB}^{res} as the bunch length that gives, on the screen, a distribution with rms vertical size equal to $\sqrt{2}\sigma_{yB}$. It is equal to

$$\sigma_{tB}^{res} = E\frac{\sigma_{yB}}{V_{defl}\omega_{RF}L} = \sqrt{\frac{E}{E_0}}\sqrt{\epsilon\beta_S}\frac{1}{V_{defl}\omega_{RF}L}; \tag{3.7}$$

where ϵ is the transverse normalized emittance of the beam, β_S is the vertical β-function at the screen position and E_0 is the electron rest energy. With the parameters of SPARC_LAB, i.e. $V_{defl} \approx 1$MV, $f_{RF} = 2.856$GHz ($\omega_{RF} = 2\pi f_{RF}$), $\epsilon = 1$mm mrad, $\beta_S = 30$m, $E = 180$MeV and $L = 4$m, resolutions of about 10fs are in principle reachable. By considering that the magnification of our CCD imaging system is 33μm/pixel (being 1 pixel 10μm), with a typical RFD calibration value of 400fs/mm the real resolution of the RFD device is about 13fs.

3.4 Injection/extraction system

The transverse matching of bunches, in particular the witness, is of primary importance for the preservation of transverse emittance and then for high quality acceleration.
The analysis of matching conditions that has been performed and that is fully exploited in the next chapter gave the result of β-function at the injection ≈ 1mm for the SPARC_LAB layout parameters with a plasma density $n_0 = 10^{16} - 5 \cdot 10^{16}$. This requirement is very challenging for the characteristics of the transport line and requires a dedicated study.

The necessity of preserving the cylindrical symmetry of the bunch after the final focus led to the choice of a triplet of permanent quadrupoles where the first and the third quadrupole are focusing on the same plane.
A preliminary study for the design of the quadrupoles has been performed using the MAD-X code [70]. The β-function evolution in both planes can be seen in Fig. 3.6 togheter with the simulation lattice, which starts from the end of the second S-band TW section. It consists in a triplet of electromagnetic quadrupoles, a C-band accelerating structure, a triplet of permanent quadrupoles, a device focusing in both planes that represents the focusing effect of the plasma channel, another triplet of permanent quadrupoles and another triplet of electromagnetic quadrupoles. The boundary conditions at the position $s = 0$ were set in agreement with previous simulations and experiments.
The preliminary results where then refined using a tracking code (General Particle Tracer, GPT) [71] from the photo-cathode to the capillary entrance. All the permanent magnet quadrupoles were designed in order to have the same gradient, $g = 520\mathrm{T/m}$. Within a triplet the first and the third quadrupole are focusing on the same plane, while the second quadrupole is defocusing and with a length that is exactly twice the length of the focusing quadrupoles. Permanent magnet quadrupoles were chosen due to the extremely high focusing gradient required. The preliminary design and the field map for the focusing magnet are reported in Fig. 3.7[1].
Further considerations led to the use of the same triplet even for the extraction system and the matching with the transport line to the undulators.

[1]The final realization of the permanent magnets was performed by KYMA S.r.l.

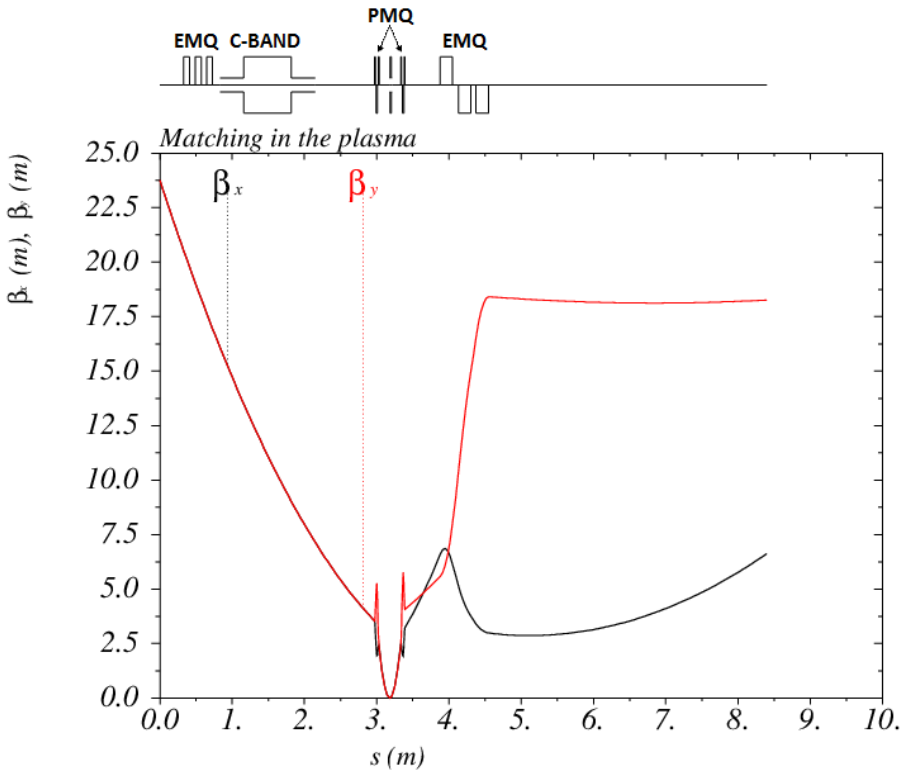

Figure 3.6. Evolution of the Twiss β-function evaluated using the MAD-X code.

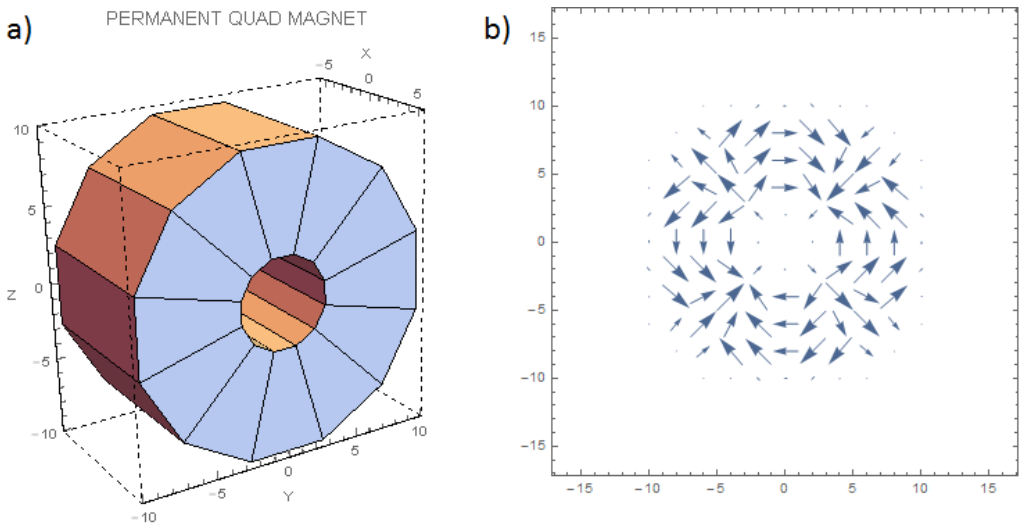

Figure 3.7. Permanent magnet focusing quadrupole design (a) and field map (b). The defocusing magnet has exactly twice the length.

3.5 Plasma channel setup

The plasma channel setup was studied in order to optimize the control over the plasma density profile intercepted by the bunches. The capillary is necessary in order to have a pre-ionized plasma. Hydrogen was chosen in order to have full ionization at relatively low plasma temperature during discharge. The plasma density measurements are performed using the Stark broadening.

3.5.1 Gas filled capillary

The plasma accelerating section consists of an inlet where it is possible to connect capillaries with different lengths and diameters filled with hydrogen. The discharge is performed using an high voltage generator ($\approx$ 20kV). The anode and the cathode are located at the extremes of the capillary. The gas injection system is composed by an hydrogen generator, connected to an high speed solenoid electrovalve contained inside the vacuum chamber that controls the final injection to the capillary.
The plasma is generated inside a capillary that is first filled with hydrogen, then ionized by an electric discharge. The gas density inside the capillary depends on the aperture time of the electrovalve ($\approx$ 3ms) in order to have the optimal plasma density for the experiment. For the first stage experiment it is forseen a capillary with a length of 3cm and a diameter of 1mm, shown during discharge in Fig. 3.8. The inlets are localized at 1/4 and 3/4 of the length, optimized in order to have a reasonably flat plasma density profile.
In order to evaluate the capillary filling time, simulations have been performed using the hydrodynamic code *OpenFoam*^{TM} [72].

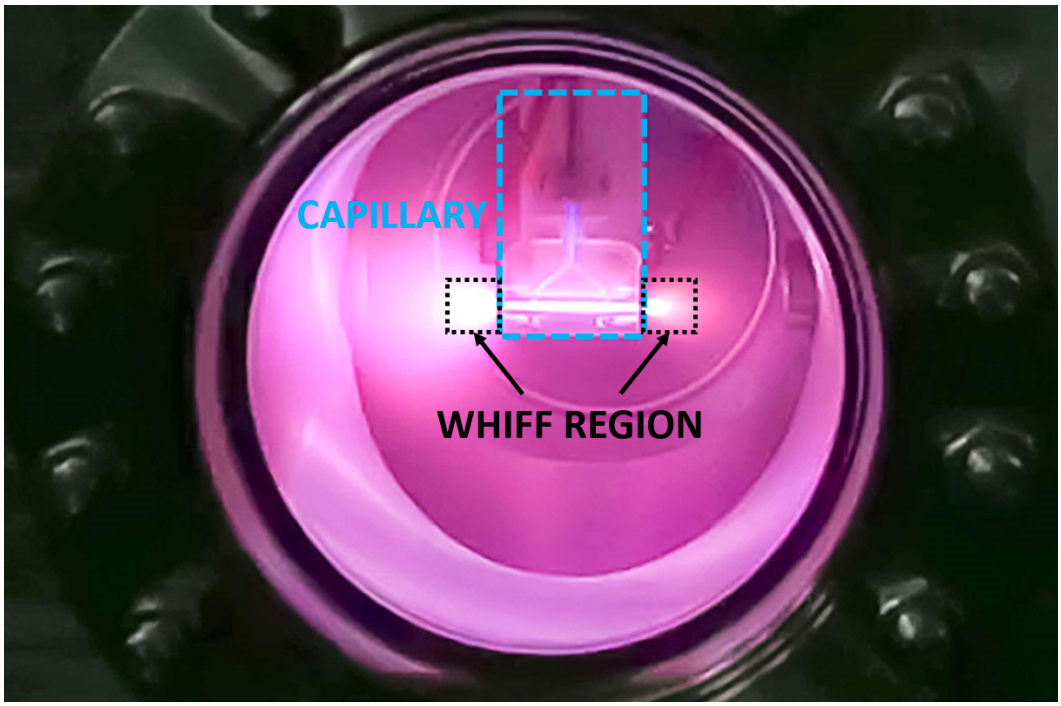

Figure 3.8. SPARC_LAB plasma capillary during discharge

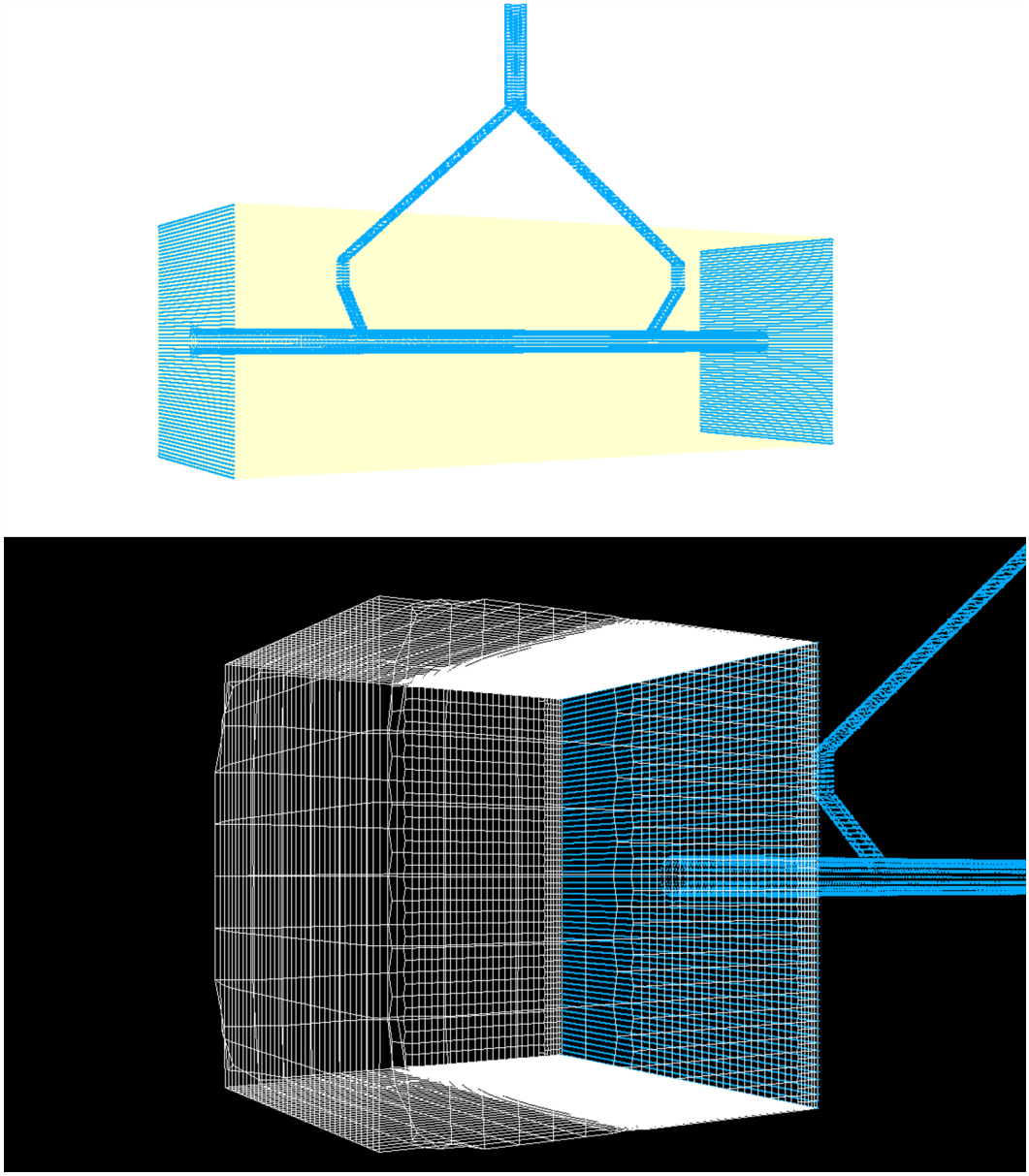

Figure 3.9. Capillary meshing and detail of whiff region meshing

Capillary mesh was modelized following capillary design as showed in Fig. 3.9. It includes all the injection system from the electrovalve to the electrodes. In order to evaluate the shape of gas whiff, the box included also a region outside the capillary with a cubic shape and 1cm edges.
The gas injection was simulated assuming a linear pressure ramp at the inlet from a value of 0mbar to 100mbar in the time of 1μs. The capillary has a fixed temperature $T = 300$K. As shown in Fig. 3.10, after $1ms$ the density growth saturates in the center of the capillary. The gas profile on axis shows a flat top between the inlets, an almost linear ramp to the capillary exit and an exponential decay outside the capillary. After $\approx 800\mu$s the gas profile stabilizes. For valve aperture times $>$ 1ms

the gas profile can be considered constant in time. It has been evaluated during experiment that aperture times of the valve < 3ms led to unwanted discharge flow inside inlet region. So the value of valve aperture were set to a constant value of 3ms.

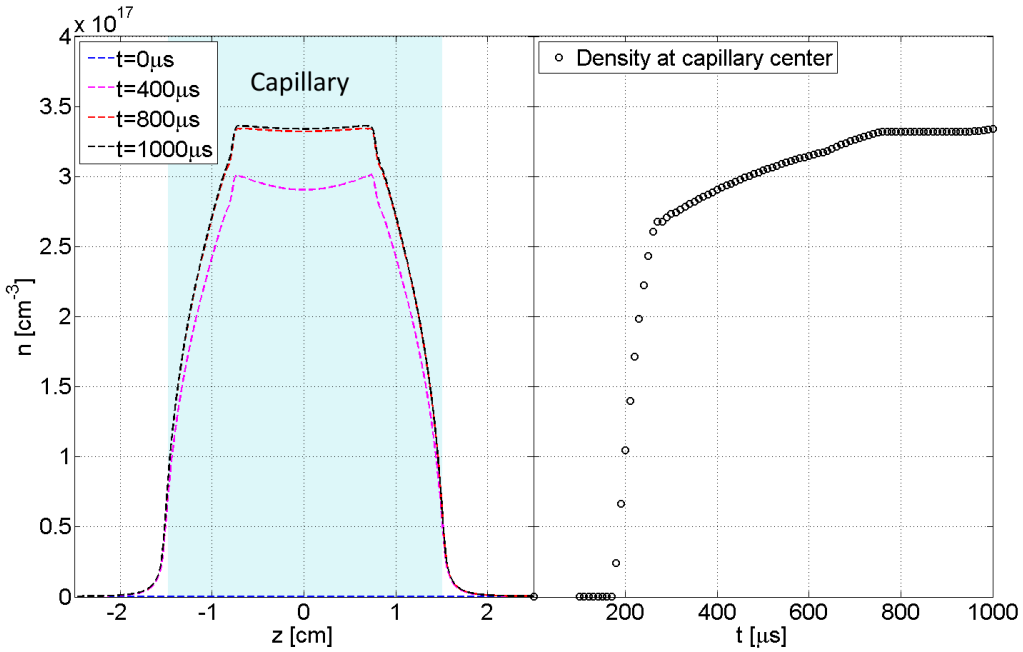

Figure 3.10. Hydrogen density on capillary axis at different times and density evolution in capillary center as a function of time.

3.5.2 Discharge system

The discharge system [73] is composed by an RLC circuit: a thyratron to charge a capacitor, a resistance to limit the current inside the plasma, an inductance which represents the parasitic inductance of the circuit and eventually there is the plasma resistance that was evaluated to be negligible respect to the total resistance of the circuit. Before the discharge the capacitor is charged by a tension $\approx$ 20kV, afterwards the capacitor is connected to the electrodes by an high voltage switch, generating the discharge through the capillary, causing the ionization of the hydrogen. The maximum current traversing the capillary depends on the capillary and on the intrinsic resistance of the discharge circuit. The injection of the beams is performed after the discharge when the electron density reaches the forseen value. The measurement of electron density is performed with the method described in the next section. In Fig. 3.11 is reported the current profile during discharge inside the capillary of Fig. 3.8.

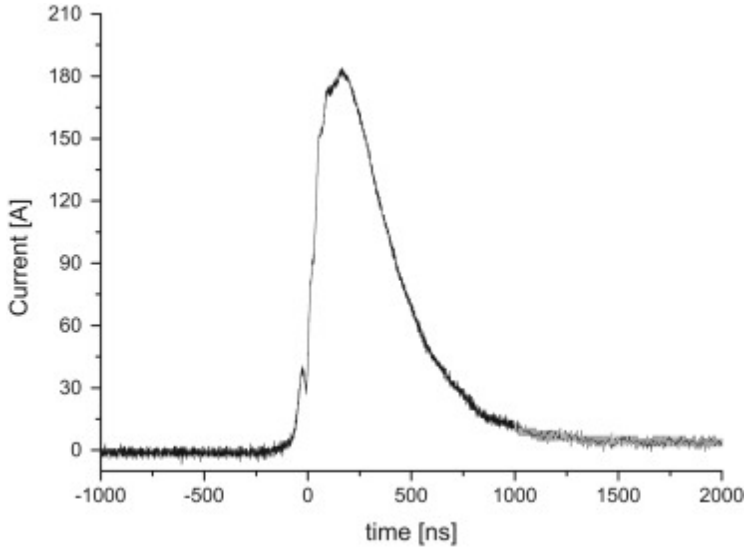

Figure 3.11. Current profile during discharge inside capillary from Ref. [73].

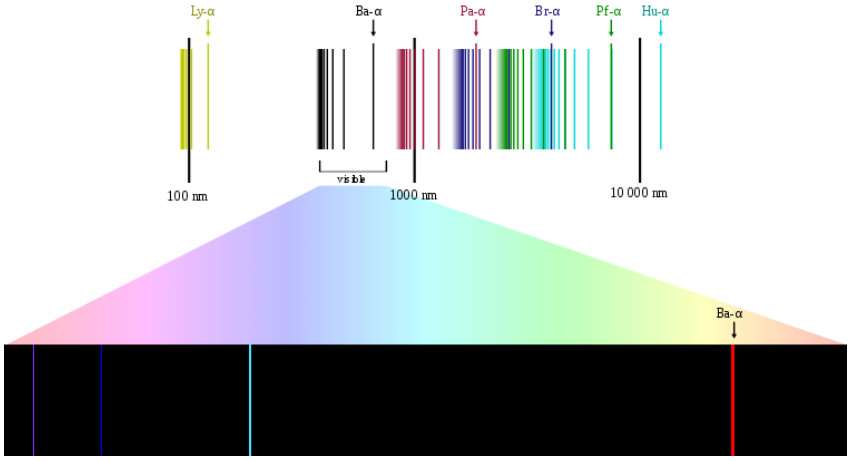

Figure 3.12. Hydrogen emission spectrum.

3.5.3 Plasma density measurement

The measurement system for the plasma density is based on the Stark effect. Hydrogen atoms, when excited, emit light at a different wavelength in the visible range, usually referred to as Balmer spectral lines (see Fig. 3.12). These lines are subjected to broadening caused by many effects. The Stark effect is the shifting and splitting of spectral lines of atoms and molecules due to presence of an external electric field. Stark broadening happens when the splitting of the spectral lines is caused by the presence of an external electric field produced by nearby free electrons. The measurement of the Stark broadening allows us to reconstruct the electron density of the plasma near the emitter. This effect has been modeled and experimentally measured. For hydrogen plasma, the full width at half maximum (FWHM) of the Balmer alpha line $\Delta\lambda$ is related to the plasma density by the following formula [74]:

$$\Delta\lambda(nm) = \alpha(n_e, T) n_e (10^{18} cm^{-3})^{2/3}; \tag{3.8}$$

The $\alpha(n_e, T)$ parameter, function of the electron density n_e and the plasma temperature T, can be derived by either fitting experimental data or computer simulations. The analysis of the Stark effect on the Balmer spectral lines can lead to plasma density information around the emitting atoms. By triggering the intensified camera with different delays it is possible to scan the temporal evolution of the plasma density along the entire longitudinal dimension of the capillary.
Measurements at SPARC_LAB [75] have been performed using both alpha and beta Balmer lines. In Fig. 3.13 we report an example of measurement result for the capillary described in section 3.5.1. The x-axis represents the longitudinal dimension of the capillary and the y-axis the time evolution.

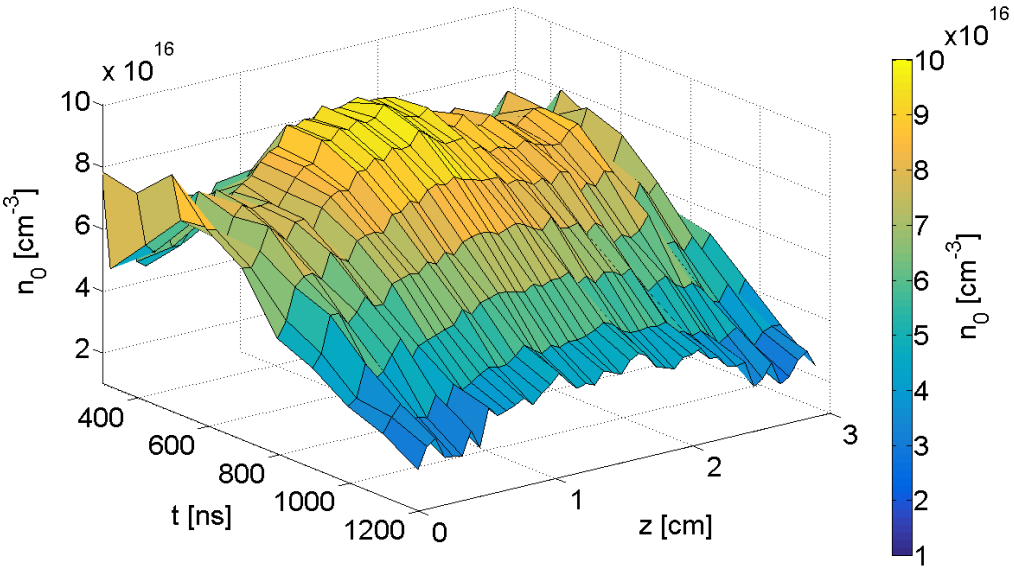

Figure 3.13. Plasma density evolution along the longitudinal capillary dimension from ref. [75].

Chapter 4

BLAST working point design

According to the consideration performed in Chapter 2 we will now design a working point for the PWFA in BLAST scheme for a beam driven experiment to be performed at the SPARC_LAB facility.
Basing on our previous work we were able to find a working point in blast scheme using a plasma with a density $n_0 = 2 \cdot 10^{16}$ cm^{-3}. The bunch parameters at the injection are listed in Table 4.1. The spatial and momentum distributions are initialized inside the code and gaussian shaped. The plasma density profile is flat top with sharp edge and the bunches are inizialized such that the center of the driver overlaps the beginning of plasma edge.

Table 4.1. Beam parameters at the injection

	Driver	Witness
Q[pC]	200	10
γ	200	
ϵ_n[mm mrad]	17	0.3
$\sigma_r[\mu$m]	10.3	1.26
$\sigma_z[\mu$m]	37.2	3
σ_E[%]	0.1	0.1

According to the equations from Chapter 2, the expected accelerating gradient is $\approx$ 2GV/m and the expected energy spread at energy doubling is 0.3%.
The simulation scans will be performed in order to find the optimal bunch separation, that is not forseen from the model. Fort the optimal bunch separation, the energy spread growth will be compared to the scaling law Eq.(2.44). Further, the transverse bunch evolution will be compared to the matching condition for witness Eq.(2.93). Then we will check the robustness of the proposed working point through a stability analysis over the expected jitter of the parameters at the injection.
All the simulations presented in this chapter, will be performed with the Architect code, described in Appendix E. The following parameters will be used: an integration time step $\Delta t \approx 0.44$fs and the mesh are squared with a dimension 0.75μm$\times 0.75\mu$m. The corresponding CFL parameter is 0.5. The box is composed by a $732\hat{u}_r \times 932\hat{u}_z$

cell grid. The dimension of the box is $275\mu m \times 700\mu m$, in the range $0 - 275$ for the transverse dimension and in the range $-200 - 500$ for the longitudinal dimension. Mesh structure is reported in Fig. 4.1. The driver is located at $z = 0$ and it is discretized with $4 \cdot 10^5$ particles while the witness is discretized with $5 \cdot 10^4$ particles.

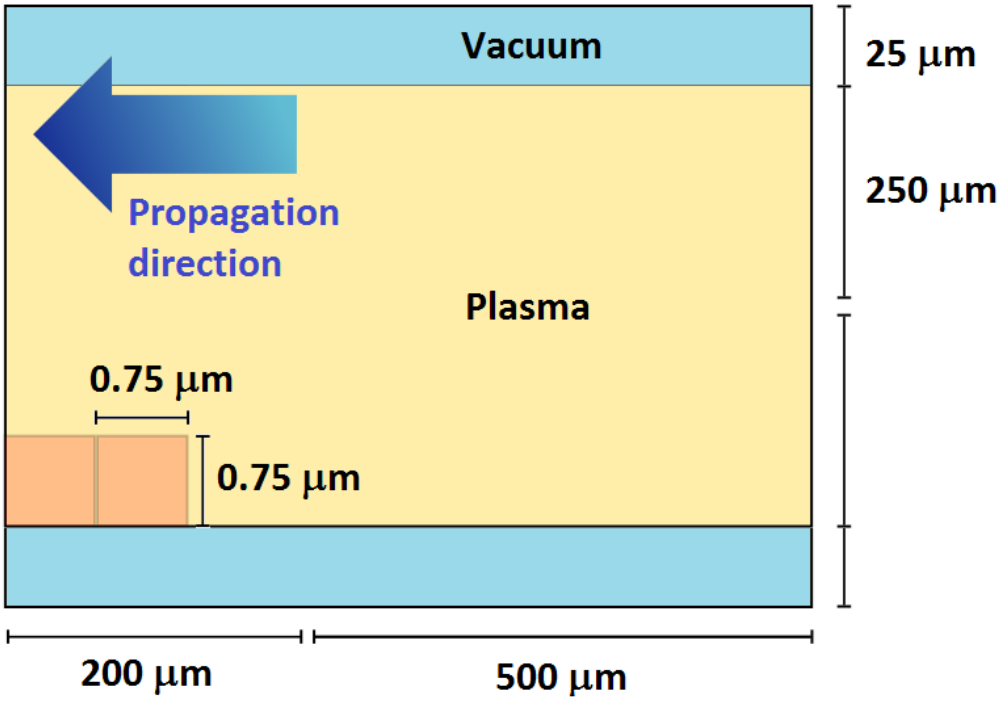

Figure 4.1. Mesh structure of the simulations.

4.1 Bunch separation scan

Two series of simulations have been performed in order to evaluate the optimal injection distance. The range of the first simulation scan is $0.45 - 0.55\lambda_p$ with steps of $0.025\lambda_p$. The range of the second simulation scan is $0.5 - 0.525\lambda_p$ with steps 0f $0.005\lambda_p$. In Fig. 4.2 and Fig. 4.3 are reported the results of the scan in terms of energy spread. In order to avoid the effect of the tails on the statistics, the energy spread is evaluated through a gaussian fit of the bunch energy distribution. In Fig. 4.2 is reported the energy spread evolution along the plasma channel and in Fig. 4.3 is reported the final energy spread as a function of the bunch separation. In Fig. 4.4 and Fig. 4.5 are reported the same results for the second scan. The injection length that minimizes the energy spread and guarantees the best result is $\Delta z = 0.505\lambda_p$.

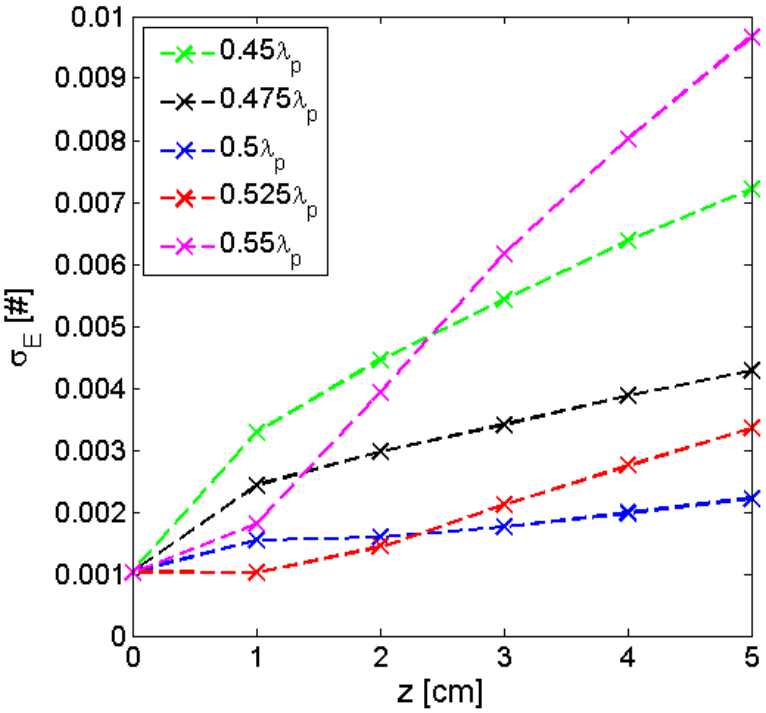

Figure 4.2. Energy spread vs. propagation length in plasma channel. Bunch separation scan at low resolution.

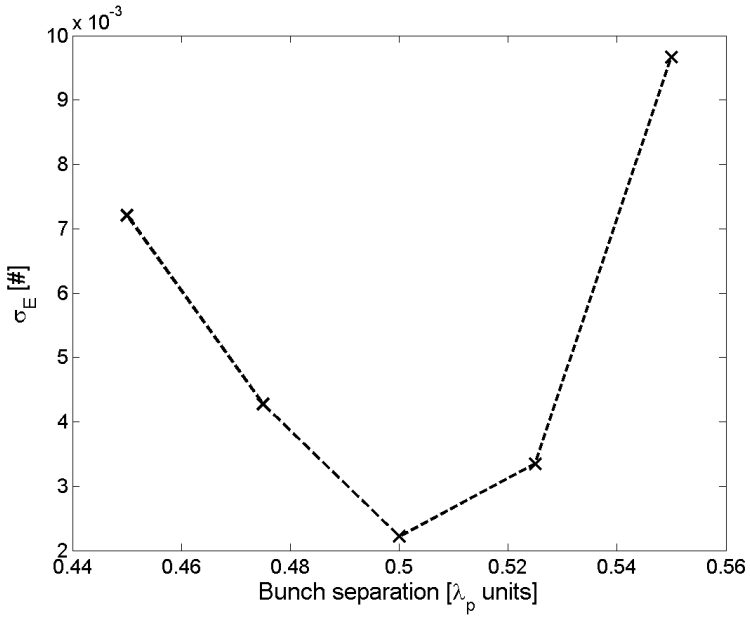

Figure 4.3. Final energy spread vs. bunch separation. Bunch separation scan at low resolution.

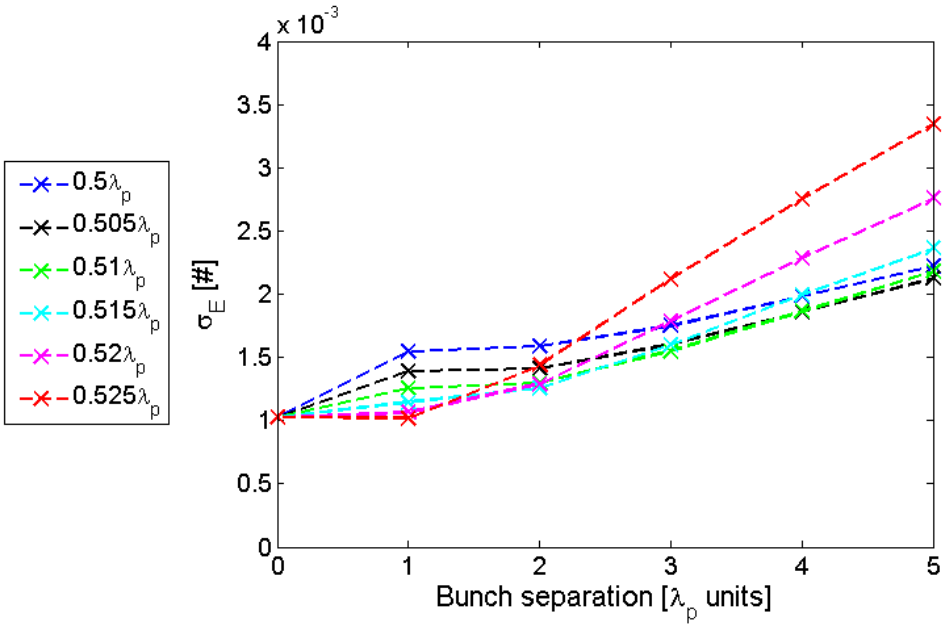

Figure 4.4. Energy spread vs. propagation length in plasma channel. Bunch separation scan at high resolution.

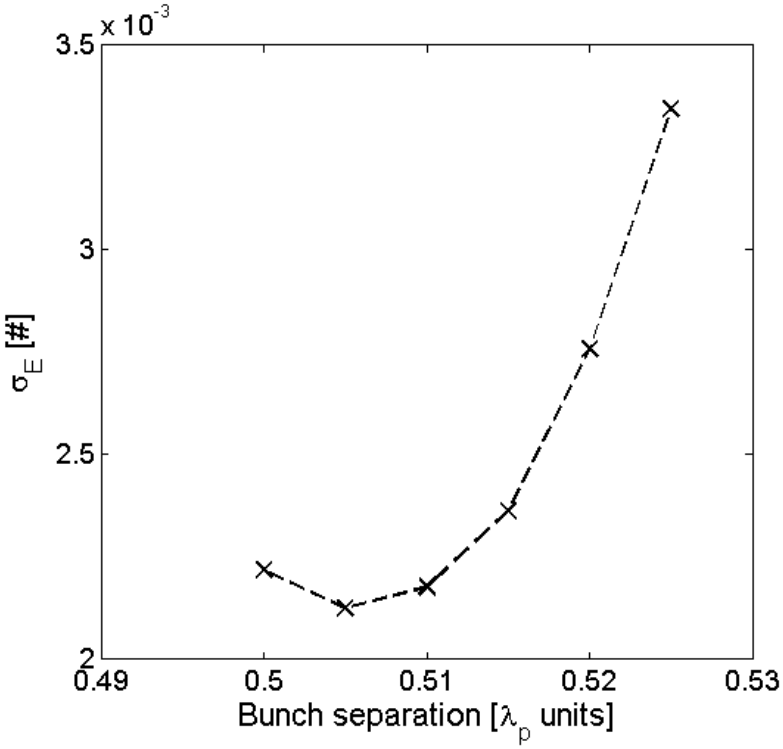

Figure 4.5. Final energy spread vs. bunch separation. Bunch separation scan at high resolution.

4.2 Witness transverse envelope

As we pointed out in chapter 2, witness energy spread growth in BLAST scheme can be generated only by mismatching. Following the matching conditions Eq.(2.93), the mismatching can be generated only by an error on the waist position. Since the formation of the witness blow-out region occurs reasonably after a plasma wavelength of propagation, we can define a natural error in the waist position $\Delta s = \lambda_p$. The matching condition Eq.(2.93) can be turned into a matching condition for the β-function that is

$$\beta_x = 2\frac{\sqrt{\gamma}}{k_p}. \tag{4.1}$$

Assume to inject a beam that at waist has a β-function that follows Eq.(4.1). Adopting the approximation that near the waist with no focusing force the α-function grows linearly

$$\alpha(s) = -\frac{s}{\beta_w}; \tag{4.2}$$

where β_w is the β-function at waist, we have that

$$\beta(s) = \beta_w + \frac{s^2}{\beta_w}. \tag{4.3}$$

Since $\beta_w = \beta_m$, we have that assuming an error in the injection Δs in the waist position, Eq.(2.65) becomes

$$\epsilon_{n,fin} = \epsilon_{n,init}\left(1 + \frac{\Delta s^2}{\beta_w^2}\right). \tag{4.4}$$

Assuming that the natural error $\Delta s = \lambda_p$, the emittance increase can be written as

$$\epsilon_{n,fin} = \epsilon_{n,init}\left(1 + \frac{\pi^2}{2\gamma}\right). \tag{4.5}$$

According to Eq.(4.5), the emittance increase is below the 5%. As pointed out in Ref. [48], in mismatched cases the β-function will oscillate around the matched case. In Fig. 4.6 we can see that the envelope oscillation is of the order of 20% of the spot size. The emittance increase is around 2%, lower than the evaluated acceptable limit. In Fig.4.7 we can see a comparison between the witness β-function and the matching condition evaluated through Eq.(4.1). After a propagation of $\approx$ 1cm, the result is consistent with the theoretical previsions performed for the BLAST scheme. A possible explanation for the initial discrepancy is furnished in the next section.
In order to have a comparison with the blow-out model, we tried to perform the same simulation assuming at the injection a β-function following the ion column model for blow-out. In this case the spot size at the injection is $\sigma_x = 1.05\ \mu$m and $\beta_x = 0.75$ mm. As we can see from Fig.4.8 the beam in this case acts as a mismatched beam, assesting on the matching β value expected from our model. The conclusion is that the blow-out model doesn't apply in this case.

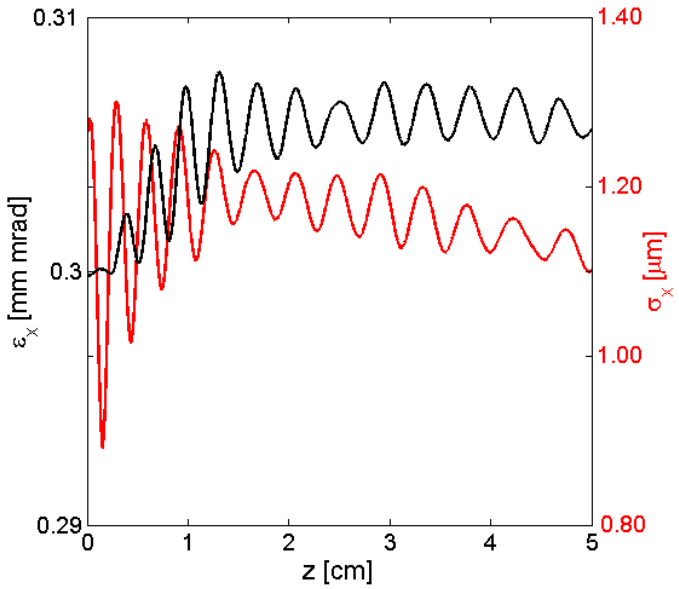

Figure 4.6. Witness envelope and emittance evolution during the propagation in the plasma channel.

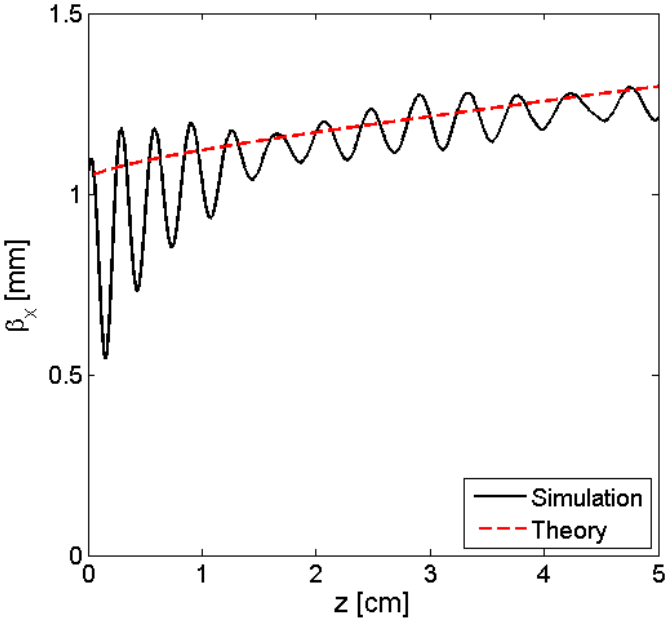

Figure 4.7. β-function evolution of the witness compared with the theoretical previsions of the BLAST scheme model.

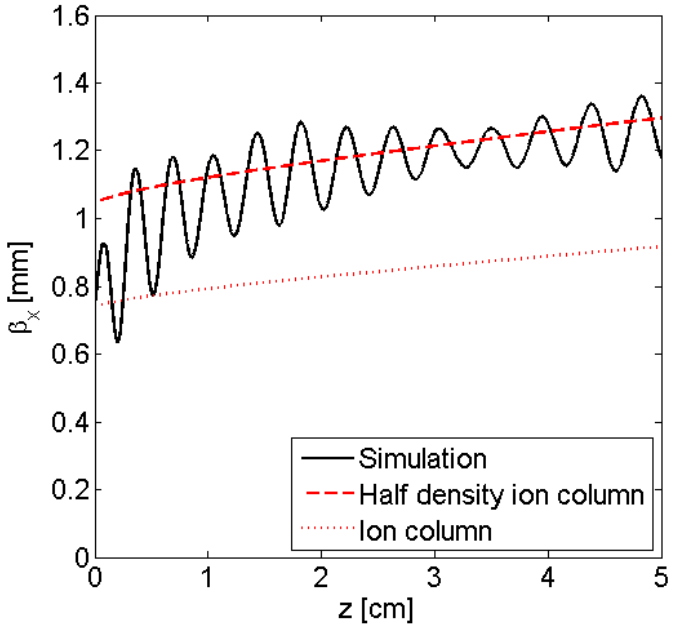

Figure 4.8. β-function evolution of a witness injected following the transverse matching conditions of the ion column model compared with the theoretical previsions of the BLAST scheme model and the blow-out ion column model.

4.3 Accelerating gradient and energy spread

The forseen accelerating gradient for the working point is $E_z \approx 2\text{GV/m}$. In Fig. 4.8 we report the witness energy and the effective accelerating gradient as a function of propagation distance in plasma.

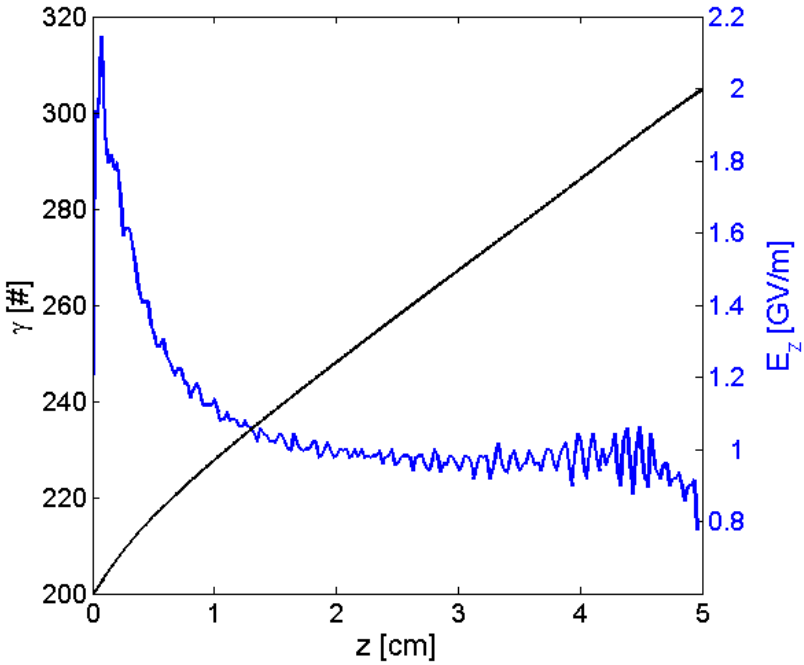

Figure 4.9. Witness energy (black) and effective accelerating gradient (blue).

As we can see, the maximum accelerating gradient reached inside the plasma is consistent with our prevision. The reduction of the accelerating gradient is due to expected effects of head erosion. We notice in this case that after the initial driver arrangement (1cm of propagation inside plasma) the accelerating gradient stabilizes at a value $E_z \approx 1\text{Gv/m}$.
Combining this result with the betatron oscillation result, we conclude that during the first centimeter of propagation, the driver evolves to a stable configuration inside plasma that guarantees a constant accelerating field and a full accomplishment of the BLAST scheme prerequisites. The driver evolution is not forseen by the model developed in this work as we already pointed out in section 2.5. A model for the treatment of driver evolution will be discussed in last chapter.
In Fig. 4.9 is reported the witness LPS before and after the acceleration. As expected, the result of the LPS is consistent with the assumption of Chiou et Katsouleas [46] that the minimum energy spread can be reached in the case of null longitudinal derivative of the accelerating field.
Since we reach the condition $\frac{\partial E_z}{\partial \xi} = 0$ we can use Eq.(2.44) in order to forsee the energy spread evolution.
In Fig. 4.9 we report a comparison of the bunch energy spread evolution as a function of the energy with the results from Eq.(2.44).

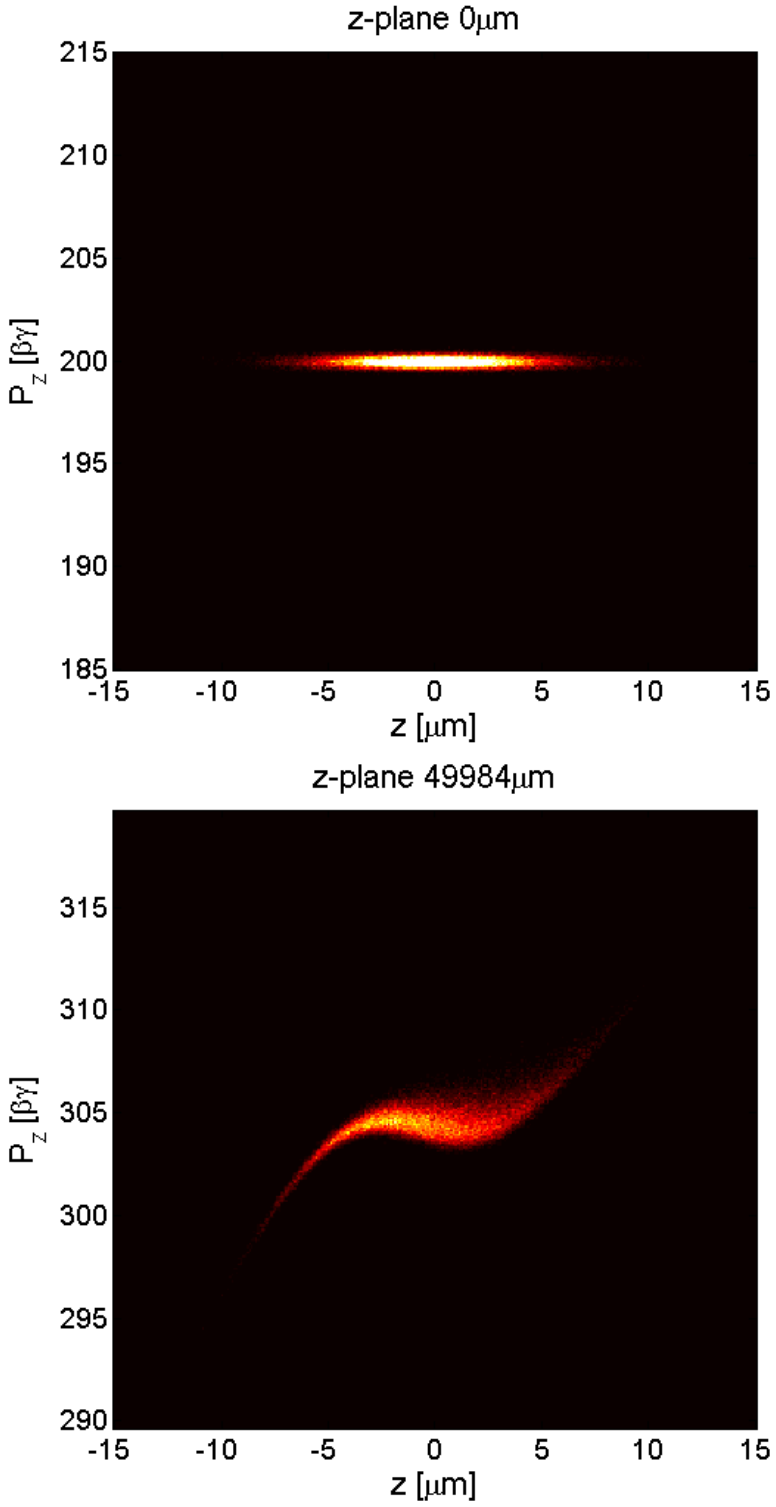

Figure 4.10. Witness LPS before and after acceleration.

We can notice the very nice agreement of the simulation with the theoretical prevision,

validating the consideration performed over energy spread.

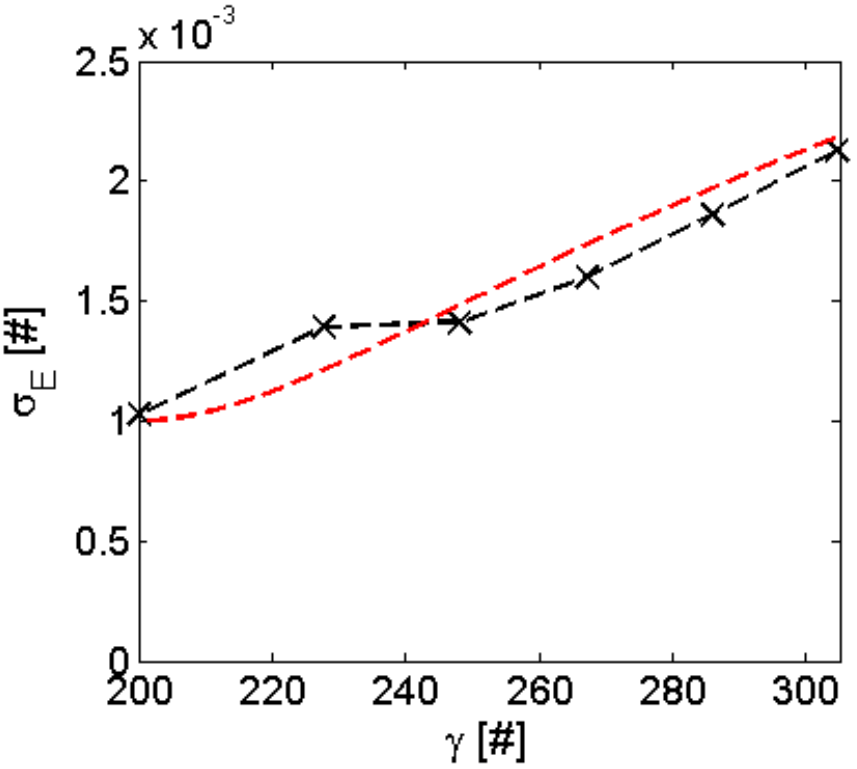

Figure 4.11. Energy spread evolution inside plasma.

Table 4.2. Witness parameters at injection and extraction

	Witness	
	Entrance	Exit
γ	200	305
ϵ_n[mm mrad]	0.3	0.305
$\sigma_r[\mu\text{m}]$	1.26	1.1
$\sigma_z[\mu\text{m}]$	3	3
$\sigma_E[\%]$	0.1	0.21

4.4 Working point result

The outcoming witness parameter after the acceleration are reported in table 4.2 The average accelerating gradient is 1.07GV/m. Using Eq.(2.44) the forseen energy spread for energy doubling is 0.3%. The asymptotic energy spread (limit of Eq.(2.44) for $\gamma \to \infty$) is 0.57%. The length of the plasma channel for the energy doubling is 10cm.

4.5 Tolerance analysis

In order to perform the tolerance analysis over the proposed working point we used the results of the measurements performed at the SPARC photoinjector in order to evaluate the jitters of the bunch parameters at the plasma channel entrance. Simulation scans where used to evaluate which of these jitters observably affect the outcoming witness parameters. The influential jitters are the following

- driver and witness transverse spot size ±15%;
- driver and witness length ±12%;
- driver and witness charge ±10%;
- bunch separation ±8%.

For every simulation performed in the tolerance analysis, variations over spot size, length and charge were considered always at the same in percentage for both driver and witness. These assumptions derive from the following considerations.
Assuming that the jitter on the spot size depends on energy jitter, an that the variation on energy depends on the phase jitter between the photo-chatode laser and the RF pulse, the jitter ar reasonably the same both for driver and for witness.
The phase jitter can causes also a variation on the bunch length [45]. The variations can be different in percentage over bunch depending on the compression phase in velocity bunching scheme. The compression phase also affects the separation length between bunches. We decided to neglect all these aspects because they get over the accuracy of this phase of preparation of the experiment.
The fluctuations on charge are due to jitters on laser energy that with the SPARC_LAB configuration are of the same amount both for driver and for witness.

Assuming these jitters we performed a simulation scan over 30 reasonable configurations of the real photo-injector using the sampling approach of the latin hypercube (LHS) [76]. The results are reported in Fig. 4.12, Fig. 4.13 and Fig. 4.14.
The outcoming beams result very stable in term of quality. The average energy spread on the sample is $\approx 0.4\%$ with a standard deviation $< 0.2\%$. The emittance growth is $< 7\%$ in all the simulations considered. The most evident effect of jitter is related to the outcoming witness energy. The average value of γ is ≈ 305 with a standard deviation of $\approx 5\%$.

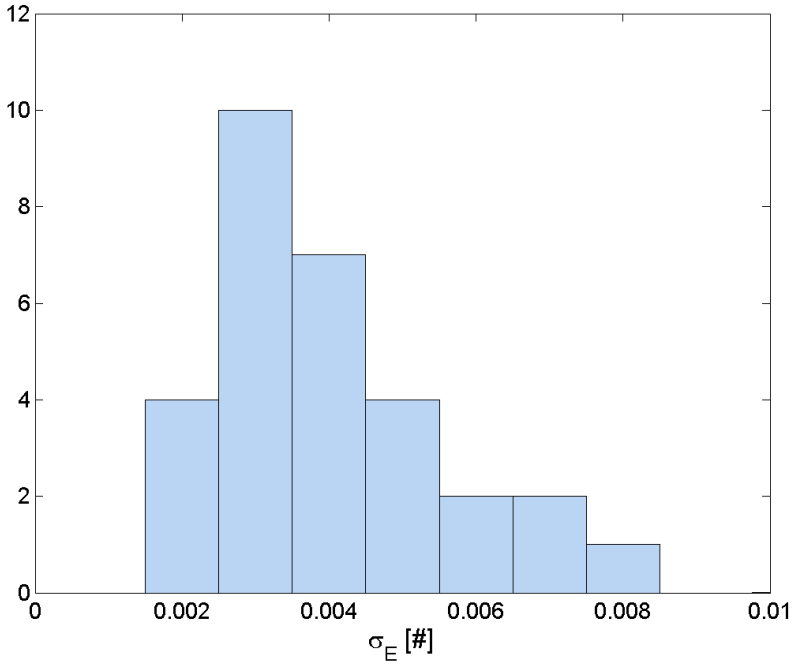

Figure 4.12. Energy spread jitter in LHS.

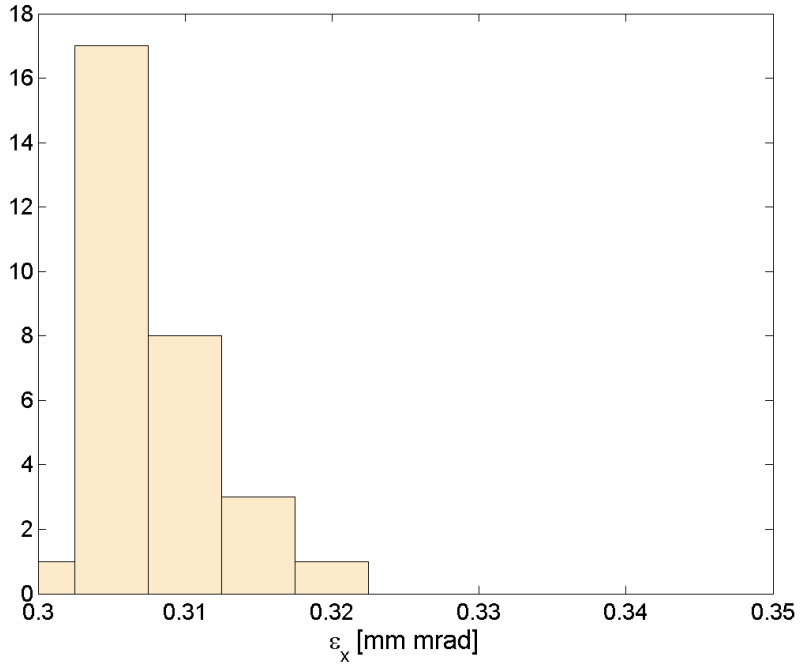

Figure 4.13. Emittance jitter in LHS.

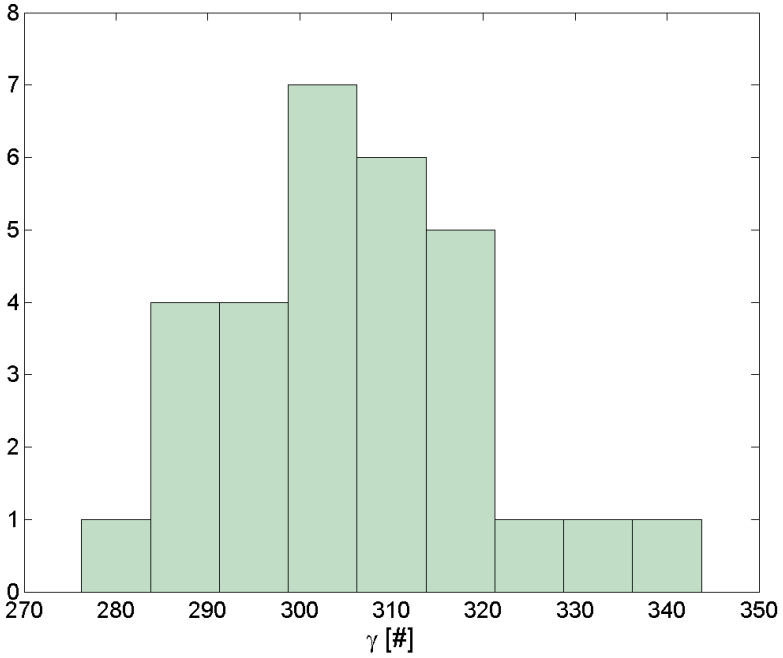

Figure 4.14. Energy jitter in LHS.

Chapter 5

Conclusions and future perspectives

The BLAST scheme working points were defined in the context of this thesis work. The main aspects useful for a working point design were derived from a theoretical point of view and cross checked with the simulation results with an evident agreement. The tolerance study evidenced a great stability of the proposed working point in terms of beam quality but a relatively high energy jitter (5%).
Expected result for this kind of experiment are of the same order of magnitude of the state of the art.
The BLAST working points result to be suitable for high quality beam driven PWFA experiments. Future perspectives of this work concern mainly the following aspects:

- experimental demonstration of the results;
- applications: plasma driven FEL;
- higher energy performances;
- extension of the model in order to include also the head erosion.

As we pointed out, a working point in blast scheme requires a witness with a very high brightness and a driver with a very low brightness. One of the possibilities to design a start-to-end working point with this features is represented by the hollow beam velocity bunching scheme [45]. In conventional multi-bunch velocity bunching schemes, the emittance growth of the witness is due to space-charge effects that, when considering two crossing beams with the same particles, act as a nonlinear diverging lens. The hollow beam is a scheme that consists on a train of bunches where the driver has an hollow profile. An hollow beam profile can be obtained by implementing an hollow laser pulse on the cathode. As showed in Fig.(5.1), the witness passes through the driver hollow, minimizing the space charge effects. The transverse electric field (due to space-charge) for a hollow beam centered in r_0 and having width σ_r is given by

$$E_r(r) = \frac{n_b}{\epsilon_0}\frac{\sigma_r^2}{r}\left(e^{-r_0^2/2\sigma_r^2} - e^{-(r-r_0)^2/2\sigma_r^2}\right).$$

For pure Gaussian beams ($r_0 = 0$) it is $E_r > 0$, so particle are pushed outwards. Instead, in hollow beams ($r_0 > 0$) it is $E_r < 0$ for $r < r_0$. If the hole is completely charge-free, then $E_r = 0$.
The SPARC_LAB configuration allows the possibility of testing the outcoming beam configuration as driving bunch for an FEL. In order to verify if it is possible to have an FEL radiation with the current SPARC_LAB test facility we will use the scaling laws from the work of Xie [77] assuming the SPARC_LAB undulator parameters and the beam obtained by simulations in chapter 4.
The radiation in this case results to be single slice. The scaling laws from [77] were evaluated assuming multiple slices, affecting the reliability of the previsions.
The expected radiation is $\approx 4 \cdot 10^{12}$ photons, with a saturation length $L \approx 7.5$m and a saturation power of ≈ 130MW. So the BLAST scheme is at present a possible candidate for this experiment.
The evaluation of the performances at higher energy will be performed in the context of EuPRAXIA project. The EuPRAXIA (European Plasma Research Accelerator with eXcellence In Application) project [78] is a proposed EU design study on a plasma based accelerator with an high degree of control on accelerated beam quality that allows to perform practical applications.
The final project should consist in a compact accelerator at 5GeV with a a beam quality that is high enough to pilot an FEL and other experiments in the fields of high energy physics.
The design study for EuPRAXIA is still at a preliminary phase. One of the possibilities that is invesigated for the design consist in an external injection beam driven scheme. The project is also divided in several steps. The aim of the first step consists in an high quality plasma based accelerator at 1GeV such that at least one half of the final energy of the bunch is obtained from a plasma booster.
The design of future working points can take a great advantage from the evaluation of head erosion effect, that is of primary importance in order to evaluate more precisely the expected accelerating gradient of a beam driven plasma wakefield accelerator in linear regime.
Since the field of a the head of an high density bunch can be also treated using linear equations [34], such a model could be easily extended also for high density bunches.
As we remarked during the work, the structure of the linear equations developed doens't allow to use them to describe the head erosion because the bunch distribution during the propagation evolves to a correlated bunch distribution that is not described by the system of equations.
For this reason, the analysis of the head erosion requires a partial reformulation of the equations, basing on a distribution that in general can be also correlated.
Due to the extreme interest concerning this argument, an head erosion modelization in linear approximation is considered the main task for the extension of the BLAST scheme.

Appendices

Appendix A

Linear theory

In this section, we find the electromagnetic field response of a cold plasma to a bunch of arbitrary charge moving approximately at the speed of light in the so called 'linear approximation'.
The electromagnetic field response can be found from the Green's function response to a test charge. One of the possible approaches is using potentials (ϕ,A) [29]. Katsouleas [30] developed an easier derivation by solving directly for the fields, as in the following.
Consider a charge q injected inside cold plasma at rest with a speed v_b. We choose the reference frame such that the speed of the particle is in the same direction of the z-axis and assuming cylindrical system of coordinates. The charge density can be written as

$$\rho_b = q\delta(\vec{r})\tilde{\delta}(z - ct) \tag{A.1}$$

where $\tilde{\delta}(r) = 1/(2\pi r)\delta(r)$.
We now write all the equations governing the motion of plasma particles. Maxwell's equations:

$$\begin{aligned} \nabla\cdot\vec{E} &= \frac{\rho}{\epsilon_0}; \\ \nabla\times\vec{E} &= -\frac{\partial\vec{B}}{\partial t}; \\ \nabla\times\vec{B} &= \mu_0\left(\vec{J} + \epsilon_0\frac{\partial\vec{E}}{\partial t}\right); \\ \nabla\cdot\vec{B} &= 0; \end{aligned} \tag{A.2}$$

where $\vec{E}$, $\vec{B}$ and $\vec{J}$ are the electric field, the magnetic field and the current density, μ_0 and ϵ_0 are the magnetic permeability and the electric permettivity and ρ is the electric charge density.
The continuity equation for the electrons:

$$\frac{\partial n_e}{\partial t} + \nabla\cdot(n_e\vec{v_e}) = 0; \tag{A.3}$$

where n_e is the local electron density and $\vec{v_e}$ is the local plasma electron speed.
The definiton of momentum, charge density and current density inside plasma perturbed by an electron beam:

$$\begin{aligned} \vec{p_e} = \gamma m_e \vec{v_e} &= \frac{1}{\sqrt{1 - \frac{v_e^2}{c^2}}} m_e \vec{v_e}; \\ \rho &= -en_b + en_i - en_e; \\ \vec{J} &= -en_b \vec{v_b} - en_e \vec{v_e}; \end{aligned} \tag{A.4}$$

where m_e is the electron mass, n_b is the bunch density, n_i the ion density and n_e the electron density.
We now consider all the quantities describing plasma as deviations from the equilibrium values:

$$\begin{aligned} \vec{E} &= \vec{E_0} + \vec{E_1}; \\ \vec{B} &= \vec{B_0} + \vec{B_1}; \\ \vec{v_e} &= \vec{v_0} + \vec{v_1}; \\ n_e &= n_0 + n_1; \\ \vec{J} = \vec{J_b} + \vec{J_0} + \vec{J_1} &= -en_b \vec{v_b} - e(n_0 + n_1)\vec{v_0} - en_0 \vec{v_1} - en_1 \vec{v_1}. \end{aligned} \tag{A.5}$$

From the hypotesis of cold plasma at rest we can state that $\vec{E_0} = 0$, $\vec{B_0} = 0$ and $\vec{v_0} = 0$. From the hypotesis of neutral plasma and negligible motion of ions (that derive from the consideration that the ion mass $m_i \gg m_e$) we can state that $n_0 = n_i$. We conclude that

$$\begin{aligned} \vec{J} &= -en_b \vec{v_b} - en_0 \vec{v_1} - en_1 \vec{v_1}; \\ \rho &= -en_b - en_1. \end{aligned} \tag{A.6}$$

In the non relativistic limit we rewrite all our set of equations as

$$\begin{aligned} &\nabla \times \vec{E_1} = -\frac{\partial B_1}{\partial t}; \\ &\nabla \times \vec{B_1} = \mu_0 \vec{J} + \frac{1}{c^2} \frac{\partial \vec{E_1}}{\partial t}; \\ &\nabla \cdot \vec{E_1} = -\frac{en_b + en_1}{\epsilon_0}; \\ &\nabla \cdot \vec{B_1} = 0; \\ &m_e \left(\frac{\partial \vec{v_1}}{\partial t} + \vec{v_1}(\nabla \cdot \vec{v_1}) \right) = -e\vec{E_1} - e\vec{v_1} \times \vec{B_1}; \\ &\frac{\partial n_1}{\partial t} + \nabla \cdot ((n_0 + n_1)\vec{v_1}) = 0. \end{aligned} \tag{A.7}$$

Now we linearize all the equation assuming that the system experiences only small deviations from the equilibrium condition ($F_1 \approx 0$ for any field inside plasma) and ignoring all the perturbation terms of second order. The equations become:

$$\begin{aligned}
&\nabla\times \vec{E_1} = -\frac{\partial B_1}{\partial t};\\
&\nabla\times \vec{B_1} = -e\mu_0(n_b\vec{v_b} + n_0\vec{v_1}) + \frac{1}{c^2}\frac{\partial \vec{E_1}}{\partial t};\\
&\nabla\cdot \vec{E_1} = -\frac{en_b + en_1}{\epsilon_0};\\
&\nabla\cdot \vec{B_1} = 0;\\
&\frac{\partial \vec{v_1}}{\partial t} = -\frac{e}{m_e}\vec{E_1};\\
&\frac{\partial n_1}{\partial t} + n_0\,\nabla\cdot \vec{v_1} = 0.
\end{aligned} \tag{A.8}$$

The last of Eq.(A.8) was obtained for a costant background density n_0. This condition is not always true, so the theory should be reformulated for plasma ramps. In the limit that $\nabla n_0 \cdot \vec{v_1} \ll n_0\,\nabla\cdot \vec{v_1}$ the formulas computed are still valid. Now we derive the last equation with respect to t and we get

$$\frac{\partial^2 n_1}{\partial t^2} + n_0\,\nabla\cdot \frac{\partial \vec{v_1}}{\partial t} = 0; \tag{A.9}$$

then substituting the fifth and third of Eq.(A.8) inside Eq.(A.9) we get

$$\frac{\partial^2 n_1}{\partial t^2} + \omega_p^2 n_1 = -\omega_p^2 n_b; \tag{A.10}$$

where

$$\omega_p = \sqrt{\frac{e^2 n_0}{\epsilon_0 m_e}}; \tag{A.11}$$

has the dimension of a frequency. ω_p is known as plasma pulsation and describes the harmonic behaviour of the plasma for small oscillations.
Now we write the particle density in the case of a single ultrarelativistic electron inside plasma, with a direction of motion parallel to the z-axis

$$n_b = \tilde{\delta}(r)\delta(z - ct). \tag{A.12}$$

We perform a change of variables as follows:

$$\begin{aligned}
\xi &= z - ct;\\
\frac{\partial}{\partial t} &= -c\frac{\partial}{\partial \xi};\\
k_p &= \omega_p/c
\end{aligned} \tag{A.13}$$

where k_p is known as plasma skin depth. The equation for the plasma density becomes

$$\frac{\partial^2 n_1}{\partial \xi^2} + k_p^2 n_1 = -k_p^2 n_b. \tag{A.14}$$

Substituting Eq.(A.12) inside Eq.(A.14) we find the Green's equation for a plasma

$$\frac{\partial^2 n_1}{\partial \xi^2} + k_p^2 n_1 = -k_p^2 \tilde{\delta}(r)\delta(\xi); \tag{A.15}$$

that can be solved by the use of Laplace transform as follows:

$$\begin{aligned} s^2\mathcal{L}\{n_1\} - sn_1(0) - sn_1'(0) + k_p^2\mathcal{L}\{n_1\} = -k_p^2\delta(\vec{(}r)) \Rightarrow \\ \Rightarrow n_1(r,\xi) = -k_p\tilde{\delta}(r)\sin(k_p\xi)\Theta(\xi); \end{aligned} \tag{A.16}$$

where Θ is the Heaviside function. The wake generated by a single particle is harmonic and has a wavelength depending on the plasma density

$$\lambda_p = 2\pi\sqrt{\frac{\epsilon_0 m_e c^2}{e^2 n_0}}. \tag{A.17}$$

The response to an impulse with a non point-like shape is obtained as the space integral of the Green function Eq.(A.16). Assuming that we have a charge density distribution in cylindrical symmetry that is separable over the longitudinal and transverse component such as that $n_b(r,\xi) = n_{b\parallel}(\xi)n_{b\perp}(r)$, we can write the resulting density as

$$\begin{aligned} n_1(r,\xi) =& -k_p\int_{-\infty}^{+\infty} d\xi' \int_0^{2\pi} d\theta' \int_0^{+\infty} r'dr' n_{b_\perp}(r')\times \\ &\times n_{b\parallel}(\xi')\tilde{\delta}(|\vec{r}-\vec{r}'|)\sin(k_p(\xi-\xi'))\Theta(\xi-\xi') = \\ =& -k_p\int_{-\infty}^{+\infty} n_{b\parallel}(\xi')\sin(k_p(\xi-\xi'))\Theta(\xi-\xi')d\xi'\times \\ &\times \int_0^{2\pi} d\theta' \int_0^{+\infty} n_{b_\perp}(r')\tilde{\delta}(|\vec{r}-\vec{r'}|)dr'; \end{aligned} \tag{A.18}$$

that leads to

$$\begin{aligned} n_1(r,\xi) =& -k_p n_{b_\perp}(r)\int_{-\infty}^{\xi} n_{b_\parallel}(\xi')\sin(k_p(\xi-\xi'))d\xi' = \\ =& \frac{\epsilon_0 k_p^2}{e} Z(\xi) n_{b\perp}(r); \end{aligned} \tag{A.19}$$

where $Z(\xi)$ is defined as

$$Z(\xi) = -\frac{e}{\epsilon_0 k_p}\int_{-\infty}^{\xi} n_{b_\parallel}(\xi')\sin(k_p(\xi-\xi'))d\xi'. \tag{A.20}$$

Notice that in our notation from now on we will assume that all bunches are gaussian with the following bunch distribution

$$\begin{aligned} n_{b\parallel} &= n_b e^{-\xi^2/2\sigma_z^2}; \\ n_{b\perp} &= e^{-r^2/2\sigma_r^2}; \end{aligned} \tag{A.21}$$

with $n_b = \frac{Q/e}{(2\pi)^{3/2}\sigma_r^2\sigma_z}$.
Now in order to find the electric field we take the curl of the Faraday's law:

$$\nabla\times(\nabla\times\vec{E_1}) = -\frac{\partial}{\partial \mathrm{t}}(\nabla\times\vec{B_1}) \Rightarrow \nabla^2\vec{E_1} - \nabla(\nabla\cdot\vec{E_1}) = \frac{\partial}{\partial \mathrm{t}}(\nabla\times\vec{B_1}). \tag{A.22}$$

We replace the curl of the magnetic field from the Ampére-Maxwell equation and the divergence of the electric field from Gauss's law

$$\begin{aligned} \nabla^2\vec{E_1} - \nabla\left(-\frac{e}{\epsilon_0}n_b - \frac{e}{\epsilon_0}n_1\right) &= \frac{\partial}{\partial \mathrm{t}}\left(\mu_0\vec{J_1} + \mu_0\vec{J_b} + \frac{1}{c^2}\frac{\partial\vec{E_1}}{\partial t}\right) \Rightarrow \\ \Rightarrow \nabla^2\vec{E_1} - \frac{1}{c^2}\frac{\partial^2\vec{E_1}}{\partial t^2} &= -en_0\mu_0\frac{\partial\vec{v_1}}{\partial t} - ec\mu_0\hat{z}\frac{\partial n_b}{\partial t} - \frac{e}{\epsilon_0}\nabla n_b - \frac{e}{\epsilon_0}\nabla n_1. \end{aligned} \tag{A.23}$$

As before we perform the substitution $\xi = z - ct$. We obtain

$$\nabla^2\vec{E_1} - \frac{\partial^2\vec{E_1}}{\partial\xi^2} = ecn_0\mu_0\frac{\partial\vec{v_1}}{\partial\xi} + ec^2\mu_0\hat{z}\frac{\partial n_b}{\partial\xi} - \frac{e}{\epsilon_0}\nabla n_b - \frac{e}{\epsilon_0}\nabla n_1. \tag{A.24}$$

We replace the derivative of the velocity with the linear motion equation $\frac{\partial\vec{v_1}}{\partial\xi} = -\frac{e}{cm_e}\vec{E_1}$

$$\left(\nabla^2 - \frac{\partial^2}{\partial\xi^2} - k_p^2\right)\vec{E_1} = ec^2\mu_0\hat{z}\frac{\partial n_b}{\partial\xi} - \frac{e}{\epsilon_0}\nabla n_b - \frac{e}{\epsilon_0}\nabla n_1. \tag{A.25}$$

Now we split the divergence and Laplace operator longitudinal and transverse component. The new operators can be written

$$\begin{aligned} \nabla^2 = \nabla_r^2 + \frac{\partial^2}{\partial\xi^2} &= \frac{1}{r}\frac{\partial}{\partial r}\left(r\frac{\partial}{\partial r}\right) + \frac{\partial^2}{\partial\xi^2} \\ \nabla &= \hat{r}\frac{\partial}{\partial r} + \hat{z}\frac{\partial}{\partial\xi}. \end{aligned} \tag{A.26}$$

We can write the density functions in the right side of Eq.(A.21) as

$$\begin{aligned}
\frac{\partial n_b}{\partial \xi} &= \frac{\partial}{\partial \xi}[\tilde{\delta}(r)\delta(\xi)] = \tilde{\delta}(r)\delta'(\xi) \\
\nabla n_b &= \hat{r}\frac{\partial n_b}{\partial r} + \hat{z}\frac{\partial n_b}{\partial \xi} = \hat{r}\tilde{\delta}'(r)\delta(\xi) + \hat{z}\tilde{\delta}(r)\delta'(\xi) \\
\nabla n_1 &= -\hat{r}k_p\frac{\partial}{\partial r}\left[\delta(\vec{r}\sin(k_p\xi)\Theta(\xi)\right] - \hat{z}k_p\frac{\partial}{\partial \xi}\left[\delta(\vec{r}\sin(k_p\xi)\Theta(\xi)\right] = \\
&= -\hat{r}k_p\tilde{\delta}'(r)\sin(k_p\xi)\Theta(\xi) - \hat{z}k_p^2\tilde{\delta}(r)\cos(k_p\xi)\Theta(\xi).
\end{aligned} \tag{A.27}$$

Now substituting back the expression for the density into the equation for the field and separating the longitudinal and radial components we get the equations

$$\begin{aligned}
(\nabla_r^2 - k_p^2)E_{1r} &= -\frac{e}{\epsilon_0}\tilde{\delta}'(r)\left[\delta(\xi) - k_p\sin(k_p\xi)\Theta(\xi)\right] \\
(\nabla_r^2 - k_p^2)E_{1z} &= -\frac{e}{\epsilon_0}\tilde{\delta}(r)\cos(k_p\xi)\Theta(\xi);
\end{aligned} \tag{A.28}$$

The last equation for the logitudinal electric field can be easily solved for the longitudinal direction, but it also requires to be solved in the transverse direction or rather finding the transverse dependence for the longitudinal field. The last equation of Eq.(A.28) is a Green's equation in the transverse coordinate

$$(\nabla_r^2 - k_p^2)G(\vec{r};\vec{r'}) = \delta(\vec{r} - \vec{r}'); \tag{A.29}$$

that is the Green's function response to the Kelvin-Helmholtz and admits the solution [30]

$$G(\vec{r};\vec{r'}) = -\frac{1}{2\pi}K_0(k_p|\vec{r} - \vec{r}'|); \tag{A.30}$$

where K_0 is the modified Bessel function of the second kind at 0^{th} order. So the longitudinal field generated by an electron inside plasma in linear approximation can be written

$$E_{1z}(r,\xi) = \frac{e}{2\pi\epsilon_0}k_p^2K_0(k_pr)\cos(k_p\xi)\Theta(\xi). \tag{A.31}$$

In a linear system we can apply the superposition principle. So we can write the field as the convolution of the field generated by a particle and the distribution of the particles. As for the density perturbation, if we suppose to have a separable charge density distribution over the longitudinal and transverse component such as that $n_b(r,\xi) = n_{b\parallel}(\xi)n_{b\perp}(r)$ we can write the field for an entire bunch as the convolution product between

$$
\begin{aligned}
E_z(r,\theta,\xi) &= Z'(\xi)R(r) \\
Z'(\xi) &= -\frac{e}{\epsilon_0}\int_{-\infty}^{\xi} n_{b_\parallel}(\xi')\cos(k_p(\xi-\xi'))d\xi' \\
R(r) &= \frac{k_p^2}{2\pi}\int_0^{2\pi} d\theta' \int_0^{+\infty} r'dr' n_\perp(r') K_0(k_p|\vec{r}-\vec{r}'|);
\end{aligned}
\tag{A.32}
$$

where $Z'(\xi)$ is the first derivative of the function introduced in Eq.(A.20).
The transverse wake can be found easily using the Panofsky-Wenzel theorem [79]

$$
\frac{\partial W_\parallel}{\partial r} = \frac{\partial W_\perp}{\partial \xi}. \tag{A.33}
$$

where

$$
W_{\parallel,\perp} = e\left(E + \vec{v_b}\times\vec{B_1}\right)_{z,r} \tag{A.34}
$$

are the parallel and longitudinal wake functions. Since the direction of the bunch is parallel to the z-axis, $(v_b \times B_1)_z = 0$, so unless a constant the longitudinal electric field is equal to the longitudinal wake function. Applying the Panofsky-Wenzel theorem we obtain

$$
\frac{\partial E_{1z}}{\partial r} = \frac{\partial (E_{1r} - cB_{1\theta})}{\partial \xi}. \tag{A.35}
$$

Therefore from Eq.(A.32)

$$
E_{1r} - cB_{1\theta} = Z(\xi)R'(r). \tag{A.36}
$$

Combining the Gauss' law in its differential form

$$
\frac{\partial E_z}{\partial \xi} + \frac{\partial}{r\partial r}(rE_r) = \frac{\rho}{\epsilon_0}; \tag{A.37}
$$

and the z component of Ampere's law

$$
\frac{1}{r}\frac{\partial}{\partial r}(rB_\theta) = \mu_0 J_z - \frac{1}{c}\frac{\partial E_z}{\partial \xi}; \tag{A.38}
$$

we obtain a differential expression for the transverse wakefield

$$
\frac{\partial}{\partial r} r\left(E_r - cB_\theta\right) = \frac{r}{\epsilon_0}\left(\rho - \frac{J_z}{c}\right). \tag{A.39}
$$

The transverse wakefield can be easily evaluated using the electrostatic approximation, namely the assumption that the effect of the current density is negligible respect to the effect of the electrostatic field ($\vec{J} \approx 0$), an assumption that is rigorously verified for low bunch charges [34]. Assuming $J_z = 0$, the focusing field from Eq.(A.38) result to be only dependant from the charge density that we can evaluate

as $\rho(r,\xi) = -en_1(r,\xi)$. Then, inserting Eq.(A.19) Eq.(A.36) inside Eq.(A.39) we obtain

$$\frac{\partial}{\partial r}[rR'(r)] = -rk_p^2 n_{b\perp}(r); \tag{A.40}$$

that can be integrated as

$$R'(r) = -\frac{k_p^2}{r}\int_0^r n_{b,\perp}(r')r'dr'. \tag{A.41}$$

For gaussian bunch it is convenient to expand Eq.(A.21) in Taylor series in order to separate the linear component of the field from the non linear components (that, as we will show, introduce emittance growth)

$$n_{b\perp}(r) = 1 - \frac{r^2}{2\sigma_r^2} + \mathcal{O}(r^4). \tag{A.42}$$

Inserting Eq.(A.42) inside Eq.(A.41) we get

$$R'(r) = -\frac{k_p^2}{2}r + \frac{k_p^2}{8\sigma_r^2}r^3 + \mathcal{O}(r^5). \tag{A.43}$$

The analytical solution of $R(0)$ for a bunch with a transversely bi-gaussian particle distribution has been already computed in literature [31] and is

$$R(0) = \left(\frac{k_p^2\sigma_r^2}{2}\right)\left(e^{k_p^2\sigma_r^2/2}\right)\Gamma\left(0, \frac{k_p^2\sigma_r^2}{2}\right); \tag{A.44}$$

where $\Gamma(\alpha,\beta) = \int_\beta^\infty t^{\alpha-1}e^{-t}dt$ is the Euler Gamma Function.
Integrating Eq.(A.43) we get

$$R(r) = R(0) - \frac{k_p^2}{4}r^2 + \frac{k_p^2}{32\sigma_r^2}r^4 + \mathcal{O}(r^6). \tag{A.45}$$

The solution for the longitudinal plasma response functions $Z(\xi)$ and $Z'(\xi)$ can be evaluated by direct integration of the second equation of Eq.(A.32) and Eq.(A.20) considering a gaussian form for the longitudinal bunch density as Eq.(A.21). The solution is

$$Z(\xi) = -\sqrt{\frac{\pi}{2}}\frac{c^2 m_e}{e}(\alpha)(k_p\sigma_z)e^{-k_p^2\sigma_z^2/2}\,\mathrm{Im}\left[e^{ik_p\xi}\,\mathrm{erfc}\left(\frac{\xi}{\sqrt{2}\sigma_z} + i\frac{k_p\sigma_z}{\sqrt{2}}\right)\right]; \tag{A.46}$$

for the longitudinal plasma response function and

$$Z'(\xi) = \sqrt{\frac{\pi}{2}}\frac{c^2 m_e}{e}(\alpha)(k_p^2\sigma_z)e^{-k_p^2\sigma_z^2/2}\,\mathrm{Re}\left[e^{ik_p\xi}\,\mathrm{erfc}\left(\frac{\xi}{\sqrt{2}\sigma_z} + i\frac{k_p\sigma_z}{\sqrt{2}}\right)\right]; \tag{A.47}$$

for its first derivative. It is useful to notice that assuming to evaluate the field far behind the bunch, where $\xi \ll -\sigma_z$ in our notation, hold the equalities

$$Z(\xi) = -\sqrt{2\pi}\frac{c^2 m_e}{e}(\alpha)(k_p\sigma_z)e^{-k_p^2\sigma_z^2/2}\sin k_p\xi; \tag{A.48}$$

and

$$Z'(\xi) = \sqrt{2\pi}\frac{c^2 m_e}{e}(\alpha)(k_p^2\sigma_z)e^{-k_p^2\sigma_z^2/2}\cos k_p\xi. \tag{A.49}$$

Another very useful equation to perform the calculations in this thesis is the following

$$Z''(\xi) = -k_p^2 Z(\xi). \tag{A.50}$$

Appendix B

Blow-out regime

When the perturbation introduced by the driving bunch on plasma is high ($n_b/n_0 = \alpha \gg 1$) the plasma wakefield is no more described by the linear theory, since the second order term of Eq.(A.7) are not negligible. A complete analytical solution for the beam-plasma interaction in blow-out regime doesn't exist, still it is possible to extract the main features of the accelerating and focusing field inside the blow-out region, that is the region of interest for the acceleration of witness bunch.
The shape of the blow-out region has been discussed and modelized by several authors [33] [50] [34]. For our purposes the main features of the blow-out region can be summarized as follows. The shape of the blow-out region generated by a gaussian bunch is mainly ellipsoidal. Its transverse dimension is approximately

$$r_m \approx 2\sqrt{\Lambda}/k_p; \tag{B.1}$$

where k_p is the plasma skin depth already defined for the linear regime and *Lambda* is the normalized bunch length defined as

$$\Lambda = \alpha k_p^2 \sigma_r^2 = \frac{r_e}{2} \frac{N_b}{\sqrt{2\pi}\sigma_z}; \tag{B.2}$$

where r_e is the classical electron radius and N_b the number of electrons in the bunch. The length of the bubble depends from another parameter, the normalized bunch charge, that is the ratio of the beam charge to the plasma electron charge located within a volume of a cubic plasma skin depth

$$\tilde{Q} = \frac{N_b k_p^3}{n_0}. \tag{B.3}$$

For $\tilde{Q} < 1$ the plasma preserves a quasi-harmonic behaviour, namely the blow-out region length is $\approx \lambda_p$. For $\tilde{Q} > 1$ the blow-out region length is $\geq \lambda_p$. The blow-out region or bubble is surrounded by an electron sheat and in the region of the bubble closure there is a recombination region with very high electron density. In this region is present a sharp zero-crossing of accelerating field.
In order to describe the behaviour of the fields inside the blow-out region it is convenient, as for linear theory, to adopt a cylindrical system of coordinates in cylindrical symmetry. We will also apply the change of variables described by Eq.(A.13). The r component of the Ampere's law under these adoptions can be

written as

$$\frac{\partial B_\theta}{\partial \xi} = -\mu_0 J_r + \frac{1}{c}\frac{\partial E_r}{\partial \xi}; \tag{B.4}$$

while the θ component of Faraday law can be written as

$$\frac{\partial E_r}{\partial \xi} - \frac{\partial E_z}{\partial r} = c\frac{\partial B_\theta}{\partial \xi}. \tag{B.5}$$

Combining Eq.(B.4) with Eq.(B.5) we obtain for the accelerating field

$$\frac{\partial E_z}{\partial r} = \mu_0 c J_r. \tag{B.6}$$

From the assumption of immobile ion background follows that the current density is generated only from the plasma and bunch electrons. In this case we are allowed to apply the superposition principle because Eq.(B.5) is linear in J_r, so the effect on the field of the bunch and the plasma can be considered separately. Inside the blow-out region $\vec{J} = 0$ due to the absence of electrons. From this follows that

$$\frac{\partial E_z}{\partial r} = 0; \tag{B.7}$$

so, the accelerating field is independent from the radial position. In the bunch head region the blow-out is not complete so $J_r \neq 0$ and the field can be written as

$$E_z(r, \xi) = -\mu_0 \int_r^{+\infty} dr' J_r(r', \xi). \tag{B.8}$$

In order to evaluate the focusing field, as for linear theory, we write the Gauss' law in its differential form

$$\frac{\partial E_z}{\partial \xi} + \frac{1}{r}\frac{\partial}{\partial r}(rE_r) = \frac{\rho}{\epsilon_0}; \tag{B.9}$$

and the z component of Ampere's law

$$\frac{1}{r}\frac{\partial}{\partial r}(rB_\theta) = \mu_0 J_z - \frac{1}{c}\frac{\partial E_z}{\partial \xi}. \tag{B.10}$$

Combining Eq.(B.9) and Eq.(B.10) we obtain the following

$$\frac{1}{r}\frac{\partial}{\partial r}[r\,(E_r - cB_\theta)] = \frac{\rho}{\epsilon_0} - \mu_0 c J_z. \tag{B.11}$$

Assuming total blow-out, the drive bunch electrons are effectively the only free electrons inside the bubble. However, they do not produce a net contribution to the source term for focusing in Eq.(B.11). Therefore, the source term in the bubble results entirely from the static ions ($\rho = n_0 e$). By symmetry E_r and $B_\theta = 0$ at $r = 0$, so the integral over r of Eq.(B.11) yields $E_r - cB_\theta$ inside the plasma bubble

$$E_r - cB_\theta = \frac{n_0 e}{2\epsilon_0}. \tag{B.12}$$

A focusing field as in Eq.(B.12) guarantees a matching condition for the bunch that

is [39]

$$\sigma_x = \sqrt[4]{\frac{2}{\gamma}}\sqrt{\frac{\epsilon_n}{k_p}}. \tag{B.13}$$

The model described is commonly known as ion channel model. This is because the focusing field in this model results to be equivalent to the field evaluated for an uniformly charged cylinder with density $\rho = n_0 e$. The accelerating field in this model is also evaluated as independent from the radial position ($\partial E_z/\partial r = 0$) and its longitudinal slope is constant ($\partial E_z/\partial \xi$ =const). For the demonstration of the last feature, not mandatory for the aim of this work, we refer to the work of Lu et al. [34].

Appendix C

Transverse dynamics

In this appendix is given a brief introduction to the transverse beam dynamics. A most extensive treatment of this argument is given in references [47] [80] [81]. Within a Frenel-Ferret reference frame, the transverse trajectory of a particle within a particle accelerator can be described in its transverse motion by the followinq differential equation

$$x''(s) + k(s)x(s) = 0; \tag{C.1}$$

and its equivalent in the y direction, where $k(s)$ describes a focusing property that is function of the longitudinal position. If the focusing property is periodic, Eq.(C.1) is known as Hill's equation. The general solution to Eq.(C.1) is the following

$$x(s) = \sqrt{\epsilon}\sqrt{\beta(s)}\cos(\psi(s) + \phi); \tag{C.2}$$

where $\sqrt{\epsilon}$ is a constant, $\beta(s)$ is a function of the transverse position that depends on the initial conditions of the particle, ϕ is an integration constant and ψ a phase factor depending on position. From (C.2) we can derive

$$x'(s) = -\frac{\sqrt{\epsilon}}{\sqrt{\beta(s)}}\{\cos[\psi(s) + \phi] + \sin[\psi(s) + \phi]\}; \tag{C.3}$$

where we defined

$$\alpha = -\frac{\beta'(s)}{2}. \tag{C.4}$$

Solving Eq.(C.2) and Eq.(C.3) for ϵ we get the following Eq.

$$\epsilon = \gamma(s)x^2(s) + 2\alpha(s)x(s)x'(s) + \beta(s)x'^2(s); \tag{C.5}$$

where we defined

$$\gamma(s) = \frac{1 + \alpha^2(s)}{\beta(s)}. \tag{C.6}$$

Eq.(C.5) is known as Courant-Snyder equation, ϵ is the Courant-Snyder invariant and $\alpha(s)$, $\beta(s)$ and $\gamma(s)$ are known as Twiss parameters or Courant-Snyder functions. As shown in figure C.1, Eq.(C.5) describes an ellipse in the trace space xx' and we

have that the area of the ellipse $A = \pi\epsilon_x$. The same considerations can be performed also for the y plane. If the focusing term is decoupled in the transverse space (namely k_x is not a function of the position y and k_y is not a function of the position x), in order to describe the transverse motion of a particle, we need 6 Courant-Snyder functions and two Courant-Snyder parameters: $\alpha_x(s)$, $\alpha_y(s)$, $\beta_x(s)$, $\beta_y(s)$, $\gamma_x(s)$, $\gamma_y(s)$, ϵ_x and ϵ_y.

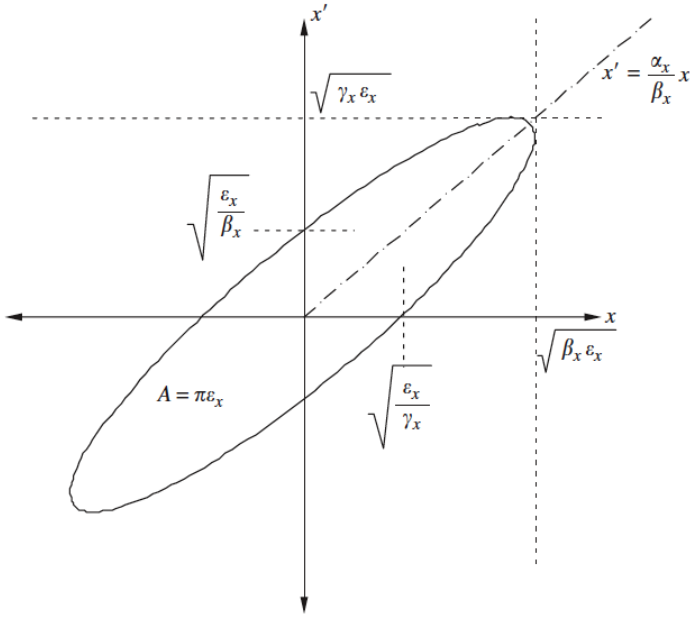

Figure C.1. Trace space ellipse described by the single particle motion.

For a group of particles, we have to relate to the particle distribution in order to evaluate the beam motion. The motion of a charged beam is described by the Vlasov-Maxwell equation

$$\frac{\partial f_e}{\partial t} + \vec{v_e} \cdot \nabla f_e - e\left(\vec{E} + \frac{\vec{v_e}}{c} \times \vec{B}\right) \cdot \frac{\partial f_e}{\partial \vec{p}} = 0. \tag{C.7}$$

The principle of equivalent beams [47] states that two beams composed of the same particle species and having the same current and kinetic energy are equivalent in an approximate sense if the second moments of distributions are the same. The second moment of a quantity is defined as

$$\sigma_a^2 = \langle a^2 \rangle = \int_V a^2 f_e dV; \tag{C.8}$$

where V is the volume in the trace space. Multiplying both sides of Eq.(C.5) for the distribution function and integrating over the trace space, we obtain

$$\epsilon_{x,rms} = \gamma_x \sigma_x^2 + 2\alpha_x \sigma_{xx'} + \beta_x \sigma_{x'}^2. \tag{C.9}$$

The ellipse described by Eq.(C.9) is an ellipse that encloses most of the beam trace space. From the ellipse relations expressed in figure C.1 we obtain the equation

$$\sigma_x = \sqrt{\epsilon_{x,rms}\beta_x}; \tag{C.10}$$

and

$$\sigma_{x'} = \sqrt{\epsilon_{x,rms}\gamma_x}. \tag{C.11}$$

From Eq.(C.4)

$$\alpha_x = -\frac{\beta_x'}{2} = -\frac{1}{2\epsilon_{x,rms}}\frac{d}{dz}\langle x^2\rangle = -\frac{\langle xx'\rangle}{\epsilon_{x,rms}} = -\frac{\sigma_{xx'}}{\epsilon_{x,rms}}. \tag{C.12}$$

Inserting Eq.(C.10), Eq.(C.11) and Eq.(C.12) inside Eq.(C.6) we obtain

$$\epsilon_{x,rms} = \sqrt{\sigma_x^2\sigma_{x'}^2 - \sigma_{xx'}^2}. \tag{C.13}$$

The particle slope x' can be written as p_x/p_z. Assuming negligible energy spread (constant p_z), Eq.(C.13) becomes

$$\epsilon_{x,rms} = \frac{1}{p_z}\sqrt{\sigma_x^2\sigma_{p_x}^2 - \sigma_{xp_x}^2} = \frac{1}{\beta\gamma m_e c}\sqrt{\sigma_x^2\sigma_{p_x}^2 - \sigma_{xp_x}^2}. \tag{C.14}$$

So $\epsilon_{x,rms}$ is not constant for an accelerating beam. We define the normalized rms emittance as

$$\epsilon_{n,x} = \sqrt{\sigma_x^2\sigma_{p_x}^2 - \sigma_{xp_x}^2}; \tag{C.15}$$

that is equivalent to the rms emittance in phase space.

Appendix D

Envelope equation derivation

In order to derive the envelope equation we start from the definition of first and second longitudinal derivative of rms beam radius

$$\frac{d\sigma_x}{dz} = \frac{d}{dz}\sqrt{\langle x^2\rangle} = \frac{1}{2\sigma_x}\frac{d}{dz}\langle x^2\rangle = \frac{\langle xx'\rangle}{\sigma_x} = \frac{\sigma_{xx'}}{\sigma_x}; \tag{D.1}$$

and

$$\frac{d^2\sigma_x}{dz^2} = \frac{d}{dz}\frac{\sigma_{xx'}}{\sigma_x} = \frac{1}{\sigma_x}\frac{d\sigma_{xx'}}{dz} = \frac{\sigma_{x'}^2}{\sigma_x} - \frac{\sigma_{xx'}^2}{\sigma_x^3} + \frac{1}{\beta_z c}\langle x\frac{d}{dt}(x')\rangle. \tag{D.2}$$

For accelerating beams is convenient to express x' as p_x/p_z. We can write

$$\frac{d}{dt}x' = \frac{d}{dt}\frac{p_x}{p_z} = \frac{\dot{p}_x}{p_z} - \frac{\dot{p}_z}{p_z}\frac{p_x}{p_z} = \frac{F_x}{p_z} - \frac{\dot{p}_z}{p_z}x'. \tag{D.3}$$

Inserting Eq.(D.3) in Eq.(D.2) we obtain

$$\frac{d^2\sigma_x}{dz^2} = \frac{\sigma_{x'}^2 - \sigma_{xx'}^2}{\sigma_x^3} + \frac{1}{\sigma_x}\frac{\langle xF_x\rangle}{c\beta_z p_z} - \frac{p_z'}{p_z}\frac{\sigma_{xx'}}{\sigma_x}; \tag{D.4}$$

and considering Eq.(D.1) and rms and normalized emittance definitions we finally get

$$\sigma_x'' + \frac{p_z'}{p_z}\sigma_x' - \frac{1}{\sigma_x}\frac{\langle xF_x\rangle}{c\beta_z p_z} = \frac{\epsilon_{x,rms}^2}{\sigma_x^3} = \frac{\epsilon_{n,x}^2}{\gamma^2\sigma_x^3}. \tag{D.5}$$

Inserting Eq.(C.10) in Eq.(D.5) we can obtain the envelope equation for the β-function

$$\frac{1}{2}\beta\beta'' - \frac{1}{4}\beta'^2 + \beta^2 K(s) = 1; \tag{D.6}$$

where $K(s)$ is the beam perveance. As demonstrated in reference [82], it's also possible to derive the envelope equation as a consequence of Vlasov-Maxwell equation. The term $\langle xF_x\rangle$ corresponds to the average value of the action of all the transverse forces acting on the beam. Usually, within the envelope equation, it is convenient to separate the external forces acting on the beam from the internal coulombian repulsion.

The net effect of the Coulomb interaction in a multi-particle system can be classified into two regimes [47]:

- Collisional regime, dominated by binary collisions caused by close particle encounters;
- Collective regime or space charge regime, dominated by the self-field produced by the particle's distribution that varies appreciably only over large distances compare to the average separation of the particles.

A measure for the relative importance of collisional versus collective effects in a beam with particle density n is the relativistic Debye length:

$$\lambda_D = \sqrt{\frac{\epsilon_0 \gamma^2 k_B T_b}{e^2 n}}; \tag{D.7}$$

where the transverse beam temperature T_b is defined as $T_b = \gamma m_e \langle v_\perp^2 \rangle$, γ is the energy of the beam, m_e electron mass, e electron charge, ϵ_0 vacuum dielectric constant and k_B the Boltzmann constant. As long as the Debye length remains small compared to the particle bunch transverse size the beam is in the space charge dominated regime and is not sensitive to binary collisions. Smooth functions for the charge and field distributions can be used in this case and the space charge force can be treated like an external applied force. The space charge field can be separated into linear and nonlinear terms as a function of displacement from the beam axis. The linear space charge term defocuses the beam and leads to an increase in beam size. The nonlinear space charge terms increase also the rms emittance by distorting the phase-space distribution. Under the paraxial approximation of particle motion we can consider the linear component only.
For a bunched beam of uniform charge distribution in a cylinder of radius R and length L, carrying a current I and moving with longitudinal velocity $v_z = \beta c$, the linear component of the transverse space charge field is approximately given by [83]

$$E_r(r, \zeta) = \frac{Ir}{2\pi\epsilon_0 R^2 \beta c} g(\zeta); \tag{D.8}$$

where $g(\zeta)$ is a form factor and can be expressed as

$$g(\zeta) = \frac{1-\zeta}{2\sqrt{A^2 + (1-\zeta)^2}} + \frac{\zeta}{2\sqrt{A^2 + \zeta^2}}; \tag{D.9}$$

where $\zeta = z/L$ is the normalized longitudinal coordinate along the bunch and $A = r\gamma/L$ is the beam aspect ratio. As γ increases $g(\zeta) \to 1$.
To evaluate the force acting on the beam one must account also for the azimuthal magnetic field $B_\theta = \dfrac{\beta}{c} E_r$. Thus the Lorentz force acting on the beam

$$F_r = e(E_r - \beta c B_\theta) = e(1-\beta^2)E_r = \frac{eE_r}{\gamma^2}. \tag{D.10}$$

The attractive magnetic force, wich becomes significant at high energy, compensate for the repulsive electric force. Therefore space charge defocusing is primarly a

non-relativistic effect and decreases as γ^{-2}.
In order to include space charge forces in the envelope equation, let's start writing the space charge forces produced by the previous fields in Cartesian coordinates

$$F_x = \frac{eIx}{2\pi\gamma^2\epsilon_0\sigma_x^2\beta c}g(\zeta). \tag{D.11}$$

We can now evaluate the envelope equation term as

$$\frac{\langle xF_x\rangle}{\beta cp} = \frac{k_{SC}}{\gamma^3}; \tag{D.12}$$

where we have introduced the generalized beam perveance

$$k_{SC}(\zeta) = \frac{2I}{I_A}g(\zeta); \tag{D.13}$$

normalized to the Alfven current $I_A = \dfrac{4\pi\epsilon_0 m_e c^3}{e} = 17kA$.
The complete envelope equation can be written as

$$\sigma_x'' + \frac{p'}{p}\sigma_x' - \frac{1}{\sigma_x}\frac{\langle xF_{x,ext}\rangle}{c\beta p} = \frac{\epsilon_{n,x}^2}{\gamma^2\sigma_x^3} + \frac{k_{SC}}{\gamma^3\sigma_x}. \tag{D.14}$$

From the envelope equation we can identify two regimes of beam propagation: emittance dominated and space charge dominated. We can define a laminarity parameter as the ratio of the space charge term as

$$\rho = \frac{I}{2I_A\gamma}\frac{\sigma_x^2}{\epsilon_n^2}. \tag{D.15}$$

$\rho \gg 1$ corresponds to a beam dominated by space charge, while $\rho \ll 1$ corresponds to a beam dominated by emittance.

Appendix E

Architect code

The simulations presented in this work have been performed with a time-explicit hybrid kinetic fluid code called Architect [84] [85].
The evolution of the beam driven scheme is solved by a particle in cell (PIC) approach with fluid equations. The PIC approach is used to treat the evolution of the bunch in the 6-dimensional phase space. The kinetical treatment of the bunch allows to analyze the phase space evolution and the emittance growth of the system. Nevertheless, allows a quite simple interface of Architect code with particle tracking codes.
The background plasma electrons are modelled as a cold relativistic fluid. The electromagnetic fields that move the particles both of the fluid and beams are generated by the sum of the currents of the beams and the background plasma. Electromagnetic fields and fluid equations are solved in cylindrical symmetry on a moving window following the bunch.
The code loop is synthesized in Fig. 4.1.
The single time step can be divided into five subsequent steps.
The first step consists in deriving the bunch current projecting bunch particles in the $r - z$ grid. The second step consists in computing the background current from the fluid number density and momentum. The third step corresponds to a finite difference time domain integration of Maxwell's equations with a Yee scheme, the source terms represented by the current are known from the previous steps. We notice that Architect computes the total electromagnetic fields, the sum of bunch and background induced fields. The fourth step integrates continuity and fluid momentum equations by using the just computed electromagnetic fields, in order to update number density and momentum. The fifth and final step consists in particle time advancement.
The Architect code has been already cross validated with the PIC code ALaDyn [86].

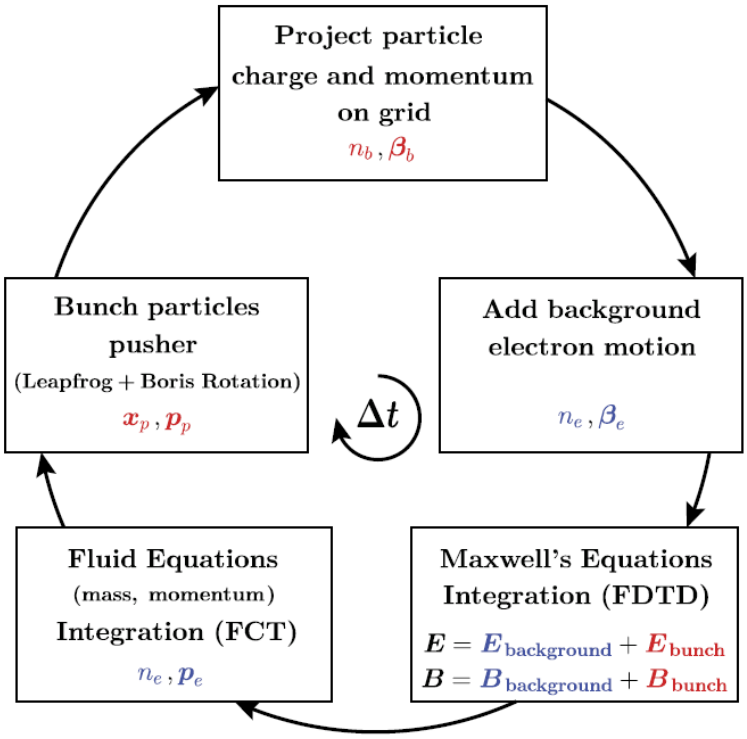

Figure E.1. Architect code loop from reference [86].

Bibliography

[1] The LHC Study Group et al. The large hadron collider, conceptual design. Technical report, CERN/AC/95-05 (LHC) Geneva, 1995.

[2] Panofsky W.K.H. and Breidenbach M. Accelerators and detectors. *Reviews of Modern Physics*, 71(2):S121, 1999.

[3] Bini S. et al. Development of x-band accelerating structures for high gradients. *Chinese physics C*, 36(7):639, 2012.

[4] Baer H. et al. The international linear collider technical design report-volume 2: physics. *arXiv preprint arXiv:1306.6352*, 2013.

[5] Esarey E., Schroeder C.B., and Leemans W.P. Physics of laser-driven plasma-based electron accelerators. *Reviews of Modern Physics*, 81(3):1229, 2009.

[6] Kilpatrick W.D. Criterion for vacuum sparking designed to include both rf and dc. *Review of Scientific Instruments*, 28(10):824–826, 1957.

[7] Boyd T.J. Jr. Kilpatrick's criterion. *Los Alamos Group AT-1 report AT-1*, 82:28, 1982.

[8] Wang J.W. Some problems on rf breakdown in room temperature accelerator structure, a possible criterion. Technical report, SLAC/AP-51, 1986.

[9] Blue B.E. et al. Plasma-wakefield acceleration of an intense positron beam. *Physical review letters*, 90(21):214801, 2003.

[10] Herr W. and Muratori B. Concept of luminosity. In *Proceedings of CERN Accelerator School*, volume 361, 2003.

[11] Brau C.A. What brightness means. In *The Physics and Applications of High Brightness Electron Beams*, volume 1, pages 20–27, 2003.

[12] Migliorati M., Bacci A., Benedetti C., Chiadroni E., Ferrario M., Mostacci A., Palumbo L., Rossi A.R., Serafini L., and Antici P. Intrinsic normalized emittance growth in laser-driven electron accelerators. *Physical Review Special Topics-Accelerators and Beams*, 16(1):011302, 2013.

[13] Tajima T. and Dawson J.M. Laser electron accelerator. *Physical Review Letters*, 43(4):267, 1979.

[14] Hogan M.J. et al. Plasma wakefield acceleration experiments at facet. *New Journal of Physics*, 12(5):055030, 2010.

[15] Modena A. et al. Electron acceleration from the breaking of relativistic plasma waves. *Nature*, 377(6550):606–608, 1995.

[16] Umstadter D., Kim J.K., and Dodd E. Laser injection of ultrashort electron pulses into wakefield plasma waves. *Physical review letters*, 76(12):2073, 1996.

[17] Ting A., Moore C.I., Krushelnick K., Manka C., Esarey E., Sprangle P., Hubbard R., Burris H.R., Fischer R., and Baine M. Plasma wakefield generation and electron acceleration in a self-modulated laser wakefield accelerator experiment. *Physics of Plasmas (1994-present)*, 4(5):1889–1899, 1997.

[18] Gahn C., Tsakiris G.D., Pukhov A., Meyer ter Vehn J., Pretzler G., Thirolf P., Habs D., and Witte K.J. Multi-mev electron beam generation by direct laser acceleration in high-density plasma channels. *Physical Review Letters*, 83(23):4772, 1999.

[19] Leemans W.P., Catravas P., Esarey E., Geddes C.G.R., Toth C., Trines R., Schroeder C.B., Shadwick B.A., Van Tilborg J., and Faure J. Electron-yield enhancement in a laser-wakefield accelerator driven by asymmetric laser pulses. *Physical review letters*, 89(17):174802, 2002.

[20] Malka V. et al. Electron acceleration by a wake field forced by an intense ultrashort laser pulse. *Science*, 298(5598):1596–1600, 2002.

[21] Faure J., Glinec Y., Pukhov A., Kiselev S., Gordienko S., Lefebvre E., Rousseau J.P., Burgy F., and Malka V. A laser–plasma accelerator producing monoenergetic electron beams. *Nature*, 431(7008):541–544, 2004.

[22] Geddes C.G.R., Toth C., Van Tilborg J., Esarey E., Schroeder C.B., Bruhwiler D., Nieter C., Cary J., and Leemans W.P. High-quality electron beams from a laser wakefield accelerator using plasma-channel guiding. *Nature*, 431(7008):538–541, 2004.

[23] Mangles S.P.D. et al. Monoenergetic beams of relativistic electrons from intense laser–plasma interactions. *Nature*, 431(7008):535–538, 2004.

[24] Leemans W.P., Nagler B., Gonsalves A.J., Toth C., Nakamura K., Geddes C.G.R., Esarey E., Schroeder C.B., and Hooker S.M. Gev electron beams from a centimetre-scale accelerator. *Nature physics*, 2(10):696–699, 2006.

[25] Kim H.T., Pae K.H., Cha H.J., Kim I.J., Yu T.J., Sung J.H, Lee S.K., Jeong T.M., and Lee J. Enhancement of electron energy to the multi-gev regime by a dual-stage laser-wakefield accelerator pumped by petawatt laser pulses. *Physical review letters*, 111(16):165002, 2013.

[26] Chen P., Dawson J.M., Huff R.W., and Katsouleas T. Acceleration of electrons by the interaction of a bunched electron beam with a plasma. *Physical review letters*, 54(7):693, 1985.

[27] Blumenfeld I. et al. Energy doubling of 42 gev electrons in a metre-scale plasma wakefield accelerator. *Nature*, 445(7129):741–744, 2007.

[28] Litos M. et al. High-efficiency acceleration of an electron beam in a plasma wakefield accelerator. *Nature*, 515(7525):92–95, 2014.

[29] Chen P. A possible final focusing mechanism for linear colliders. *Particle Accelerators*, 20(3-4):171–182, 1987.

[30] Katsouleas T., Wilks S., Chen P., Dawson J.M., and Su J.J. Beam loading in plasma accelerators. *Particle Accelerators*, 22:81–99, 1987.

[31] Lu W., Huang C., Zhou M.M., Mori W.B., and Katsouleas T. Limits of linear plasma wakefield theory for electron or positron beams. *Physics of Plasmas (1994-present)*, 12(6):063101, 2005.

[32] Rosenzweig J.B., Breizman B., Katsouleas T., and Su J.J. Acceleration and focusing of electrons in two-dimensional nonlinear plasma wake fields. *Physical Review A*, 44(10):R6189, 1991.

[33] Lotov K.V. Blowout regimes of plasma wakefield acceleration. *Physical Review E*, 69(4):046405, 2004.

[34] Lu W., Huang C., Zhou M., Tzoufras M., Tsung F.S., Mori W.B., and Katsouleas T. A nonlinear theory for multidimensional relativistic plasma wave wakefieldsa). *Physics of Plasmas (1994-present)*, 13(5):056709, 2006.

[35] Ruth R.D., Morton P.L., Wilson P.B., and Chao A.W. A plasma wake field accelerator. *Part. Accel.*, 17(SLAC-PUB-3374):171, 1984.

[36] Van Tilborg J. et al. Active plasma lensing for relativistic laser-plasma-accelerated electron beams. *Physical review letters*, 115(18):184802, 2015.

[37] Barov N., Rosenzweig J.B., Thompson M.C., and Yoder R.B. Energy loss of a high-charge bunched electron beam in plasma: Analysis. *Physical Review Special Topics-Accelerators and Beams*, 7(6):061301, 2004.

[38] Tzoufras M., Lu W., Tsung F.S., Huang C., Mori W.B., Katsouleas T., Vieira J., Fonseca R.A., and Silva L.O. Beam loading by electrons in nonlinear plasma wakes a. *Physics of Plasmas*, 16(5):056705, 2009.

[39] Barov N. and Rosenzweig J.B. Propagation of short electron pulses in underdense plasmas. *Physical Review E*, 49(5):4407, 1994.

[40] Joshi C. et al. High energy density plasma science with an ultrarelativistic electron beam. *Physics of Plasmas (1994-present)*, 9(5):1845–1855, 2002.

[41] Kallos E. *Plasma wakefield accelerators using multiple electron bunches*. PhD thesis, University of Southern California, 2008.

[42] Massimo F., Marocchino A., Chiadroni E., Ferrario M., Mostacci A., Musumeci P., and Palumbo L. Transformer ratio studies for single bunch plasma wakefield acceleration. *Nuclear Instruments and Methods in Physics Research Section A: Accelerators, Spectrometers, Detectors and Associated Equipment*, 740:242–245, 2014.

[43] CDR LCLS. Slac-r-593, 2002. *TESLA XFEL TDR*, 2002.

[44] Tzoufras M., Lu W., Tsung F.S., Huang C., Mori W.B., Katsouleas T., Vieira J., Fonseca R.A., and Silva L.O. Beam loading in the nonlinear regime of plasma-based acceleration. *Physical review letters*, 101(14):145002, 2008.

[45] Pompili R. et al. Beam manipulation with velocity bunching for pwfa applications. *Nuclear Instruments and Methods in Physics Research Section A: Accelerators, Spectrometers, Detectors and Associated Equipment*, 829:17–23, 2016.

[46] Chiou T.C. and Katsouleas T. High beam quality and efficiency in plasma-based accelerators. *Physical review letters*, 81(16):3411, 1998.

[47] Reiser M. *Theory and design of charged particle beams*. John Wiley & Sons, 2008.

[48] Mehrling T., Grebenyuk J., Tsung F.S., Floettmann K., and Osterhoff J. Transverse emittance growth in staged laser-wakefield acceleration. *Physical Review Special Topics-Accelerators and Beams*, 15(11):111303, 2012.

[49] Kim K.J. Rf and space-charge effects in laser-driven rf electron guns. *Nuclear Instruments and Methods in Physics Research Section A: Accelerators, Spectrometers, Detectors and Associated Equipment*, 275(2):201–218, 1989.

[50] Rosenzweig J.B., Barov N., Thompson M.C., and Yoder R.B. Energy loss of a high charge bunched electron beam in plasma: Simulations, scaling, and accelerating wakefields. *Physical Review Special Topics-Accelerators and Beams*, 7(6):061302, 2004.

[51] Stupakov G., Breizman B., Khudik V., and Shvets G. Wake excited in plasma by an ultrarelativistic pointlike bunch. *Physical Review Accelerators and Beams*, 19(10):101302, 2016.

[52] Ferrario M. et al. Sparc_lab present and future. *Nuclear Instruments and Methods in Physics Research Section B: Beam Interactions with Materials and Atoms*, 309:183–188, 2013.

[53] Filippetto D. et al. Phase space analysis of velocity bunched beams. *Physical Review Special Topics-Accelerators and Beams*, 14(9):092804, 2011.

[54] Valente P. et al. Development of a multi-gev spectrometer for laser–plasma experiment at flame. *Nuclear Instruments and Methods in Physics Research Section A: Accelerators, Spectrometers, Detectors and Associated Equipment*, 653(1):42–46, 2011.

[55] Rossi A.R. et al. The external-injection experiment at the sparc_lab facility. *Nuclear Instruments and Methods in Physics Research Section A: Accelerators, Spectrometers, Detectors and Associated Equipment*, 740:60–66, 2014.

[56] Chiadroni E. et al. Beam manipulation for resonant plasma wakefield acceleration. *Nuclear Instruments and Methods in Physics Research Section A: Accelerators, Spectrometers, Detectors and Associated Equipment*, 2017.

[57] Giannessi L. et al. Self-amplified spontaneous emission free-electron laser with an energy-chirped electron beam and undulator tapering. *Physical review letters*, 106(14):144801, 2011.

[58] Giannessi L. et al. Superradiant cascade in a seeded free-electron laser. *Physical review letters*, 110(4):044801, 2013.

[59] Petrillo V. et al. Observation of time-domain modulation of free-electron-laser pulses by multipeaked electron-energy spectrum. *Physical review letters*, 111(11):114802, 2013.

[60] Chiadroni E. et al. The sparc linear accelerator based terahertz source. *Applied Physics Letters*, 102(9):094101, 2013.

[61] Chiadroni E. et al. Characterization of the thz radiation source at the frascati linear accelerator. *Review of Scientific Instruments*, 84(2):022703, 2013.

[62] Vaccarezza C. et al. The sparc_lab thomson source. *Nuclear Instruments and Methods in Physics Research Section A: Accelerators, Spectrometers, Detectors and Associated Equipment*, 829:237–242, 2016.

[63] Serafini L. and Ferrario M. Velocity bunching in photo-injectors. In *AIP conference proceedings*, volume 581, pages 87–106. AIP, 2001.

[64] Anania M.P. et al. Design of a plasma discharge circuit for particle wakefield acceleration. *Nuclear Instruments and Methods in Physics Research Section A: Accelerators, Spectrometers, Detectors and Associated Equipment*, 740:193–196, 2014.

[65] Pompili R. *Longitudinal diagnostics for comb-like electron beams by means of Electro-Optic Sampling*. PhD thesis, Tor Vergata, University of Rome, 2013.

[66] Alesini D., Di Pirro G., Ficcadenti L., Mostacci A., Palumbo L., Rosenzweig J.B., and Vaccarezza C. Rf deflector design and measurements for the longitudinal and transverse phase space characterization at sparc. *Nuclear Instruments and Methods in Physics Research Section A: Accelerators, Spectrometers, Detectors and Associated Equipment*, 568(2):488–502, 2006.

[67] Potylitsyn A.P. Diffraction radiation from relativistic particles. *Springer tracts in modern physics (ISSN 0081-3869*, 239, 2010.

[68] Casalbuoni S., Schmidt B., Schmüser P., and Steffen B. Far-infrared transition and diffraction radiation. *Tesla Report*, 15(2005):2012, 2005.

[69] D Alesini, E Chiadroni, M Castellano, L Cultrera, G Di Pirro, M Ferrario, and D Filippetto. Sliced beam parameter measurements. In *Proceedings of EPAC*, 2009.

[70] Grote H. and Schmidt F. Mad-x-an upgrade from mad8. In *Particle Accelerator Conference, 2003. PAC 2003. Proceedings of the*, volume 5, pages 3497–3499. IEEE, 2003.

[71] Croia M. Beam injection optimization in the sparc_lab plasma accelerator. Master's thesis, Sapienza, University of Rome, 2014.

[72] Hrvoje Jasak, Aleksandar Jemcov, Zeljko Tukovic, et al. Openfoam: A c++ library for complex physics simulations. In *International workshop on coupled methods in numerical dynamics*, volume 1000, pages 1–20. IUC Dubrovnik, Croatia, 2007.

[73] Anania M.P et al. Plasma production for electron acceleration by resonant plasma wave. *Nuclear Instruments and Methods in Physics Research Section A: Accelerators, Spectrometers, Detectors and Associated Equipment*, 829:254–259, 2016.

[74] F Filippi, MP Anania, A Biagioni, E Chiadroni, A Cianchi, M Ferrario, A Mostacci, L Palumbo, and A Zigler. Spectroscopic measurements of plasma emission light for plasma-based acceleration experiments. *Journal of Instrumentation*, 11(09):C09015, 2016.

[75] Filippi F., Anania M.P., Biagioni A., Chiadroni E., Cianchi A., Ferrario M., Giribono A., Mostacci A., Palumbo L., and Zigler A. Plasma density profile characterization for resonant plasma wakefield acceleration experiment at sparc_lab. In *7th International Particle Accelerator Conference (IPAC'16), Busan, Korea, May 8-13, 2016*, pages 2554–2556. JACOW, Geneva, Switzerland, 2016.

[76] Wyss G.D. and Jorgensen K.H. A user's guide to lhs: Sandia's latin hypercube sampling software. *SAND98-0210, Sandia National Laboratories, Albuquerque, NM*, 1998.

[77] Xie M. Exact and variational solutions of 3d eigenmodes in high gain fels. *Nuclear Instruments and Methods in Physics Research Section A: Accelerators, Spectrometers, Detectors and Associated Equipment*, 445(1):59–66, 2000.

[78] Aßmann R. and Grebenyuk J. Accelerator physics challenges towards a plasma accelerator with usable beam quality. *Proc. IPAC*, 14, 2014.

[79] Vaganian S. and Henke H. The panofsky-wenzel theorem and general relations for the wake potential. *Part. Accel.*, 48:239–242, 1995.

[80] Rosenzweig J.B. *Fundamentals of beam physics*. Oxford University Press England, 2003.

[81] Wiedemann H. *Particle accelerator physics*. Springer, 2015.

[82] Davidson R.C. and Qin H. *Physics of intense charged particle beams in high energy accelerators*. World Scientific, 2001.

[83] Ferrario M., Fusco V., Migliorati M., and Palumbo L. Emittance degradation due to wake fields in a high brightness photoinjector. *International Journal of Modern Physics A*, 22(23):4214–4234, 2007.

[84] Marocchino A., Massimo F., Rossi A.R., Chiadroni E., and Ferrario M. Efficient modeling of plasma wakefield acceleration in quasi-non-linear-regimes with the hybrid code architect. *Nuclear Instruments and Methods in Physics Research Section A: Accelerators, Spectrometers, Detectors and Associated Equipment*, 2016.

[85] Massimo F., Marocchino A., and Rossi A.R. Electromagnetic self-consistent field initialization and fluid advance techniques for hybrid-kinetic pwfa code architect. *Nuclear Instruments and Methods in Physics Research Section A: Accelerators, Spectrometers, Detectors and Associated Equipment*, 2016.

[86] Massimo F., Atzeni S., and Marocchino A. Comparisons of time explicit hybrid kinetic-fluid code architect for plasma wakefield acceleration with a full pic code. *Journal of Computational Physics*, 327:841–850, 2016.